UNIVERSITY OF TRENTO - Italy
Department of Civil, Environmental and Mechanical Engineering

Doctoral School in Civil, Environmental and Mechanical Engineering
Topic 2. Mechanics, Materials, Chemistry and Energy - XXXVI cycle 2021/2023

Doctoral Thesis - April 2024

Luca Cecchini

Geraniaceae seed-inspired soft robots

For environmental actuation and sensing

Supervisors
Prof. Nicola Maria Pugno - Università di Trento
Dr. Barbara Mazzolai - Istituto Italiano di Tecnologia

Disclaimer
I hereby declare that this thesis represents my own and autonomous work. All sources and aids used have been indicated as such. All texts either quoted directly or paraphrased have been indicated by in-text citations. Full bibliographic details are given in the reference list which also contains internet sources containing URL and access date. This work has not been submitted to any other examination authority.

Colophon
This document was typeset with the help of KOMA-Script and LaTeX using the kaobook class.
The source code of this book is available at:
https://github.com/fmarotta/kaobook

To the people whose labors go beyond ideas into the realm of 'real materials'- to the dry-land ecologists, wherever they may be, in whatever time they work, this effort at prediction is dedicated in humility and admiration.

– Frank Herbert

Abstract

Energy is an integral part of our everyday life, being one of the most fundamental needs, including our physiological activity. In the last 50 years, energy related issues, including demand and accessibility, consumption, and consciousness of use, have become a topic of paramount importance. In an epoch characterized by an imperative for environmental stewardship, the convergence of sustainability principles with advanced technological paradigms has emerged as a beacon of promise for forthcoming generations. This doctoral thesis embarks on a systematic exploration of the domain of sustainable soft robotics, wherein innovation converges with ecological accountability.

At the outset, the fundamental definition of sustainability is rigorously analyzed, elucidating its role in sustainable technologies. A compelling exigency for robots that seamlessly harmonize with natural cadences, possessing the dual attributes of energetic self-reliance and biodegradability, assumes paramount importance.

The need for a bioinspired approach to designing robots is crucial for current robotic technology. For a suitable transition in design philosophy, bioinspired robots should be capable of undergoing a complete life cycle, incorporating growth, remodeling, and morphogenesis. Such robots should utilize sustainable materials, have renewable energy sources, and be capable of decomposing. This can be possible just by understanding and extracting key principles from living organisms rather than directly copying them. Bioinspiration requires a multidisciplinary effort and aims to create robots that can navigate complex real-world environments without simplifications. It will necessitate a reevaluation of robot design, encompassing both physical and cognitive aspects, with a focus on integrated systems rather than component assembly. This approach is seen as a valuable tool for not only advancing robotics but also contributing to the study of biology in scenarios where investigating living organisms is impractical.

Drawing inspiration from the robust architectures of nature's progeny, this thesis introduces Geraniaceae seed-inspired soft robots, ingeniously engineered for hygroscopic actuation and sensing. Through a mutually beneficial fusion of form and function, these artificial structures emulate the awe-inspiring mechanisms of seed dispersal. Delving deeper into the domain of soft robotics, this research unfolds the potential of hygroscopic actuators, harnessing the latent energy of moisture as a fundamental source for motion. Through rigorous experimentation and computational inquiry, this study underscores the efficacy of hygroscopic actuation, revealing a sustainable avenue for soft robotic soil-exploration, as well as for environmental sensing.

In summation, this doctoral endeavor stands as an affirmation of the potency of scientific inquiry in service of sustainability. From the foundational exposition of sustainability's essence to the pioneering frontiers of hygroscopic actuation and seed-inspired robotics, this thesis represents an example of sustainable technology transition. In so doing, it sets the stage for a future wherein technology and nature coalesce harmoniously, ushering in an era characterized by bioinspired design, low-impact materials, and energetically sustainable and autonomous actuation.

Contents

List of Figures

List of Tables

Introduction 1

1.1 Sustainability Transition

Energy is an integral part of our everyday life, being one of the most fundamental needs, including our physiological activity. In the last 50 years, energy related issues, including demand and accessibility, consumption, and consciousness of use, have become a topic of paramount importance. In an epoch characterized by an imperative for environmental stewardship, the convergence of sustainability principles with advanced technological paradigms has emerged as a beacon of promise for forthcoming generations.

To start this philosophical transition, it is increasingly crucial to define the concept of sustainability in a global market economies, thorugh an unambiguously quanitative description. An effective way to start should be including the physical role of exergy in the evaluation of profit and capital concept. In thermodynamics, exergy of a system is represented as the maximum fraction of energy that can be converted in mechanical work by means of reversible machines, and so, the fundamental postulates of thermodynamics can be described in this frame as: the exergy is conserved in reversible process, while it decreases in irreversible processes [1]. From a phenomenological point of view, it is an useful instrument to describe the flux of energy. Hence, it has a keyrole in the so-called thermoeconomics to evaluate the economic value considering the exchanges of goods and services (mass and energy) in a complex system, as could be the globalized market. Moreover, by consider the economic system as an ecosystem, it is possible to directly convert concepts as cost/benefit analysis as the ensemble of mechanisms for capturing and utilizing available energy to build infrastructures and to do work. Hence, sustainability can be reformulated as the quality of an output activity (and of the relative resources) that will minimize the variation of exergy.

Sustainability does not only identify a part of the utility any user can have from a certain activity (either a product or a service), but also its physical properties, which then define the utility for its usage, and therefore the subjective value component of any stakeholder. Considering by-products (waste matter/energy released into the environment by any activity) the "quality" of a stream of by-products, and therefore its composition, represents the availability to harness the energy in it contained, whether to damage the interacting organism or create value from such a stream of by-product. This qualitative feature of matter and energy, which represents also the potential to retrieve energy from materials or to produce harm to the same stakeholder, is mapped to the availability of users to pay for the activity that creates it.

Such interaction can be represented by the utility the activities serve in relation to the environment they modify, or by the concentration of pollutants affecting third parties that enter in contact with such water, air or matter streams. As exergy represents the entire potential of energy state changes in relation to an environment that normally provides lower grade enthalpy for exchanges, so stakeholders' utility functions represent wealth changes to ow towards the seller due to the utility of their products to the buyer (both for products, waste and unrecoverable waste like dispersed emissions), in relation to both system states. The availability to pay (or pay to avoid damage in case of emissions) represents

a proportional (or inverse) coefficient to weight resources like raw materials and finished goods or externalities as emissions released into air, surface water, groundwater and soil. Let us refer to its resultant impact as commons depletion, due to degradation of the intrinsic value in the resource or, economically speaking, to the externalities cost that it creates for the impacted bodies in the appreciation of such value or any other form of value (i.e. subjective). The value of a resource can be evaluated if and only if there are living organism capable of converting observation and measurement into wisdom (increase of subjectivity and increase of human value added). In the specific case of Intellectual Property (IP) issues, the Resources required for knowledge production are forms of energy, such as food, electricity or information and experiences that bring to a certain result. It is energy that generates information. This also implies that cultural background strongly affects sustainability concept and it is fundamental to achieve common goals.

The transition to sustainable technologies must take into account the minimization of exergy variation in the design, prototyping and implementation stages. As in the economic case, the engineer and the designer must include an exergy budget in the feasibility analysis. This budget is limited and shared in the biosphere by physical definition, and by legislative definition it should be distributed following a canon. Hence, in prototyping a sustainable technology, one must take into consideration: the life time of the prototype weighted to the scenario in which it is involved, energy sources and consumption, compatibility between materials and environment, impact of materials extraction, synthesis and production, end-of-life disposal, social impact and widespread knowledge.

To support long-term energy, environment and economic improvements, action plans must be collectively established. However, the creation of a common approach with a new attitude towards natural environment must require social consciousness, scientific rigor, and intellectual honesty.

1.1.1 Sustainable Development Goals

From the earliest civilizations to the present day, humanity has embodied the concept of sustainability: history is characterized by the increased regional success of a particular society, followed by crises that were either resolved, producing sustainability, or not, leading to decline [2].

The 20th century was characterized by an exponential increase in the human consumption of resources, leading to an increase in health and wealth, and perceived as progress. However, in the 1930s economists began developing models of non-renewable resource management and the sustainability of welfare in an economy that uses non-renewable resources. Following the deprivations of the great depression and World War II, the developed world entered a new period of escalating growth. A new revolution in plastic industry, synthetic chemicals (including fertilizers, herbicides and pesticides), nuclear energy and the increasing use of fossil fuels radically transformed society and destroyed rural wildlife. Considering last 50 years of industrial development and globalization, today we face a set of interconnected crises that threaten the sustainability of our socio-ecological system, as climate change, peak and decline in key non-renewable energy resources, loss of biodiversity that may reduce the resilience of our global ecosystem and its ability to provide for human needs.

Society developed the awareness that the material benefits offered by the environment are always associated with environmental costs. In the late 20th century, environmental problems became global in scale and environmental movements and agencies started spreading, until in 1987 the United Nation's Commission on Environment and Development published the Brundtland report. This one of the first international document in which the concept of sustainable development was introduced, such as "development that meets the needs of the present without compromising the ability of future generations to meet their own needs". In brief, the report can be summarized as:

- The economic growth of industrialized and industrializing societies must consider environmental limits
- Poverty reduces sustainability and accelerates environmental pressures
- There is an urgent need to balance economy and ecology
- Population food security, loss of biodiversity, energy, industry, and human settlements are connected and cannot be treated in isolation one from another
- The crises facing the planet are interlocking elements of a single crisis of the whole planet
- Strategies for environmental conservation must envisage poverty reduction, gender equity, and wealth redistribution

The Report laid the foundations for the 1992 Earth Summit in Rio de Janeiro, the Rio declaration the adoption of the Agenda 21 and the establishment of the Commission on Sustainable Development within the UN Economic and Social Council, in which the canons of environmental legislation were defined. The role of "polluter" state become central in the economic treatment, since they must pay for the relative pollution. In 1997 there has been further international advancement with the Kyoto Protocol, where the anthropogenic CO_2 emissions were defined as responsible of global warming, mainly due to fossil fuel consumption. In 2000 the United Nations provided the so-called Millenium Summit, in which all member states commited to help achieve the Millenium Development Goals by 2015.

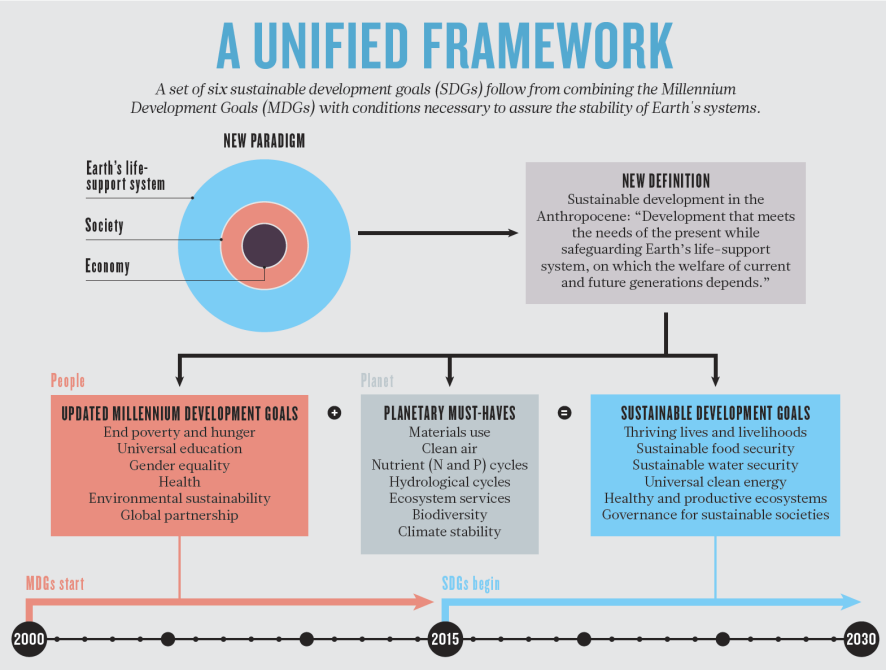

Figure 1.1: Unified framework: A set of six sustainable development goals (SDGs) follow from combining the Millennium Development Goals (MDGs) with conditions necessary to assure the stability of Earth's systems. Reprinted after request with Copyright [3].

The dimension of the concept of sustainability began to take shape when the three pillars for sustainable development were identified as economic development, social development and environmental protection [4]. The three pillars are independent, and in the long run, none can exist without the others. A different vision was proposed including the concept of environmental justice and still considering the three pillars. According to this vision, economy becomes a subsystem of human society, which is itself a subsystem of the biosphere. Any gain in one sector corresponds to a loss in another [3]. A unified definition of sustainability was proposed by Magee et al. in 2012 [5]: responsible and proactive decision making and innovation that minimizes negative impact and maintains a balance between ecological resilience, economic prosperity, political justice and cultural vibrancy to ensure a desirable planet for all species now and in the future. According to this vision, the social pillar is split into two pillars political and cultural.

With all this hystorical and philosophical consideration in mind, in 2015 the United Nations General Assembly (UNGA) formulated the Sustainable Development Goals (SDGs) or Global Goals are a collection of seventeen interlinked objectives designed to serve as a "shared blueprint for peace and prosperity for people and the planet, now and into the future" [6]. The SDGs were formulated in 2015 by as part of the Post-2015 Development Agenda, which sought to create a future global development framework to succeed the Millennium Development Goals, which ended that year. They were formally articulated and adopted in a UNGA resolution called the 2030 Agenda, known colloquially as Agenda 2030. On 6 July 2017, the SDGs were made more actionable by a UNGA resolution that identifies specific targets for each goal and provides indicators to measure progress. Most targets are to be achieved by 2030, although some have no end date.

Figure 1.2: Summary of Sustainable Development Goals. https://sdgs.un.org/goals

The SDGs and targets are meant to stimulate action in areas of critical importance for humanity and the planet. They can be summarized as:

- **People**: end poverty and hunger, in all their forms and dimensions, and ensure that all human beings can fulfil their potential in dignity and equality, in a healty environment.
- **Planet**: protect the planet from degradation, including through sustainable consumption and production, sustainably managing its natural resources and taking urgent action on climate change.
- **Prosperity**: all human beings can enjoy prosperous and fulfilling lives and that economic, social and technological progress occurs in harmony with nature.
- **Peace**: there can be no sustainable development without peace and no peace without sustainable development.
- **Partnership**: mobilize the means required to implement this Agenda through a revitalised Global Partnership for Sustainable Development.

The SDGs emphasize the interconnected environmental, social and economic aspects of sustainable development by putting sustainability at their center.

1.1.2 Advancing Environmental Sustainability through Bioinspired Soft Robotics: A Novel Approach for Sustainable Technology

The urgency to mitigate the environmental impact in design and fabrication of modern technologies has propelled the field of sustainability in technology to the forefront of research and innovation. In this framework, the emerging field of soft robotics is gaining increasing attention for its ability to fabricate intelligent machines, that take advantage of the adaptability and deformability properties of the materials and structures involved. Their flexible bodies can absorb impacts and adapt to unexpected obstacles, allowing them to continue functioning in situations where traditional rigid robots might fail. Hence, they are perfectly suitable for manipulation of sensitive objects with a high degree of dexterity, making them suitable for tasks that require delicate handling, as well as for operation in close proximity with human, medical procedures and food handling. Furthermore, the application of soft robotics extends to scenarios with delicate ecosystems, mitigating ecological disruption during exploration and environmental monitoring tasks [7, 8].

The efficient integration of actuators, sensors, computation, and energy into a singular robot demands innovative and environmentally sustainable approaches. Achieving this goal hinges on a collaborative effort involving experts in material science, chemistry, engineering, biology, computer science, and robotics. In order to establish sustainability in robotics, incorporating recycling into the initial design phase is imperative. A viable recycling plan hinges on the capacity to easily separate individual robotic materials, facilitating straightforward reuse, exchange, and enhancement of robots. Another avenue towards sustainability involves the strategic use of fewer materials through design optimization. Lightweight materials and component designs offer dual advantages for autonomous robots: firstly, they decrease weight to extend operational duration, and secondly, they curtail environmental repercussions by minimizing overall waste output. Ultimately, the realization of zero waste robotics is within reach through the implementation of fully biodegradable materials [9].

Moreover, the increase in energy demand necessitates a new category of self-sustaining robots, that harness renewable energy from the environment to carry out their tasks consistently over space and time. Through incorporating the energy source directly into the robot's structure and materials, it becomes instantly accessible for utilization, can be transformed into productive work efficiently, and, ideally, can be restored through internal energy-harvesting mechanisms. This concept is termed "Embodied Energy" [10], signifying that the same mass that traditionally serves a critical mechanical or structural role also harbors stored energy, which propels at least a segment of the robot or device.

The bioinspiration in soft robotics, matches or even surpasses the remarkable adaptability and versatility seen in organisms like microorganisms, plants, and animals. Nature provides invaluable sources of inspiration, including plants and seeds that intelligently utilize environmental cues like humidity and sunlight to effectively interact with their surrounding environment. Overall, plants and seeds offer a diverse range of mechanisms for motion that consume minimal energy, relying on environmental stimuli. For this reason, there has been a growing interest in proposing artificial actuation systems inspired by plants, particularly those using environmental stimuli-responsive materials like hygroscopic actuation.

The need of a bioinspired approach to designing robots is crucial for current robotic technology. For a suitable transition transition in design philosophy, bioinspired robots should be capable of undergoing a complete life cycle, incorporating growth, remodeling, and morphogenesis [11]. Such robots should utilize sustainable materials, have renewable energy sources, and be capable of decomposing. It can be possible just understanding and extracting key principles from living organisms rather than directly copying them. This approach requires a multidisciplinary effort and aims to create robots that can navigate complex real-world environments without simplifications. The paradigm shift will necessitate a reevaluation of robot design, encompassing both physical and cognitive aspects, with a focus on integrated systems rather than component assembly. Furthermore, bioinspired approach is seen as a valuable tool for not only advancing robotics but also contributing to the study of biology in scenarios where investigating living organisms is impractical.

1.2 Seed-inspired soft robots for energetically autonomous actuation and sensing

Plants have evolved a variety of different strategies to disperse their seeds and overcome the limitations posed by their sessile nature [12]. Seed dispersal is a very active research area from both an ecological and evolutionary perspective, because of the strong links with landscape ecology, plant diversity, dispersal adaptation, and climate change.

Seeds are an interesting source of inspiration for material science and engineering too, because they represent a rich library of morphological and mechanical features optimized for take-off, flying, landing, and drilling. These movements are defined as "passive", meaning that seed present an absence of active metabolism and no internal energy is produced. The key to seeds' mobility lies in the structural and anatomical features of their tissues, which are designed to selectively respond to changes in environmental conditions (i.e. humidity and

temperature), or the ability to exploit environmental factors as mobility vectors (animals, wind, water). Environmental responsiveness is due to the intrinsic materials and structural features (e.g., hierarchical organization, presence of awns, hairs, wings, hooks, etc.) of the seed tissues [13, 14]. In this sense, seed represent one a significant example of principle of least action in Nature, because the process of natural selection has optimized functional principles and structures to increase the chances of germination. By looking at the natural dispersion strategies of seeds, new design principles can be extracted and used as inspiration for artificial systems able to interact with the surrounding environment [15].

One mode of seed dispersal is through explosive or wind lift followed by self-burial thanks to sterile appendages capable of hygroscopic movements allowing the seeds to move across and into the soil [16]. Hygromorphism is defined as the ability of an object to change its shape and reconfigure according to environmental variation of relative humidity. It is a mechanism widely used in plant kingdom, especially in seeds, to promote germination and to perform complex operations, such as autonomous soil exploration. The deformation of the body is characterized by the internal organization of tissues, mainly composed by cellulose and lignin. Microcrystalline fiber disposition will determine the structural properties of the seed and also the anisotropic nature of the hygroscopic deformation [17]. According to the cellular structure and composition, the movement will be characterized by bending and torsional deformation, with a specific actuation time related to the water diffusion mechanisms in the internal tissues.

Nature offers several examples of structures which exploits hygroscopic effect to generate actuation systems, which exploits the environmetal variation of relative humidity (day-night or seasonal variations) as adaptation mechanism, thus enacting shape changes functional to lifecycle tasks. For example, structures like pinecones [18], wheat [15], and Geraniaceae seeds [16] absorb water molecules from the environment onto locally-aligned hygroscopic cellulose-based microstructures in the cells. This leads to shape changes that serve specific lifecycle functions, such as opening and closing in the case of pinecones, or facilitating locomotion in wheat and Geraniaceae seeds. These adaptations are crucial for tasks like seed dispersal and germination.

Based on this, the idea is to generate novel soft miniaturized robots, inspired by hygroscopic mechanisms and materials of natural seeds, and exploit their interaction with environment to generate a new generation of miniaturized and biodegradable soft robots, which can autonomously provide combined actuation and sensing.

1.2.1 Environmental propeller: the Hygroscopic effect

The botanical motion involves the intricate relationship between water transport and structural changes, known as hygroscopic deformation. This movement is driven exclusively by water, allowing it to operate effectively even in the non-living tissues of plants [19].

The chemical principle underlying hygroscopic materials is primarily based on the water adsorption, which involves the physisorption of water molecules from a vapor or liquid to the surface of a solid or liquid. In the case of hygroscopic materials, the process of water adsorption relies on several intermolecular forces, including hygrogen bonding, capillary action, Van der Waals forces and Ion-dipole interaction [20]. The combination of these intermolecular forces allows hygroscopic materials to attract and hold water molecules from the surrounding environment, often leading to changes in the physical state of the material. In particular, artificial and natural hygroscopic materials presents dissolution, which involves the breaking of chemical bonds within the material and the resulting in a homogeneous dispersion in water. For example, salts like sodium chloride readily dissolve in water when exposed to humid conditions. Some polymers, like cellulose, can form gels when exposed to water environment. This results in a three-dimensional network structure with a high water content [20]. This will lead to an expansion or swelling of the polymeric matrix, which will increase the overall volume of the structure, maintaining a visco-elastic behaviour. The absorption of water will lead to changes in mechanical properties, such as tensile strength, hardness, and flexibility. For example, wood can expand and contract with changes in humidity, affecting its dimensional stability [20].

Moreover, temperature plays a crucial role in hygroscopic adsorption, because it influence intrinsically both the rate and extent of moisture uptake by hygroscopic materials. In fact, the kinetics of water adsoprtion can be described using the isotherm relation, which relates the environmetal moisture in the surrounding phase and water content adsorbed on the surface of the hygroscopic material, at thermal equilibrium. In general, isotherm information is analyzed by applying various models, with the most suitable model chosen to study adsorption patterns. The Freundlich and Langmuir isotherms are the main approaches employed to forecast the adsorption capacity of a specific material [21]. As general rule, the activation energy of adsorption, which quantifies the energy required for a molecule to move from the gas phase to the solid phase, decreases with increasing temperature. This means that at higher temperatures, water molecules are more likely to transition from the vapor phase to the solid phase. This is important in applications where controlled moisture release is crucial.

The amount of volumetric expansion in response to changes in moisture content is measured through the Coefficient of Hygroscopic Expansion (CHE) [19].

Several parameters can influence this coefficient:

- **Chemical composition**: hydroxyl (-OH), carboxyl (-COOH), or other polar groups tend to be more hygroscopic; materials with ionic constituents may exhibit significant hygroscopic behavior due to the interaction between charged ions and water molecules; in polymers, the length of polymer chains can influence hygroscopicity. Longer chains often have more sites for water adsorption [22].
- **Physical structure**: porous materials have more surface area and can hold more water, potentially leading to greater hygroscopic expansion. The size, shape, and distribution of pores are crucial factors; crystalline regions in a material may limit the accessibility of water molecules, reducing hygroscopic expansion compared to amorphous regions; more dense materials may have fewer sites available for water adsorption compared to less dense materials; larger surface area (or surface to volume fraction) allows for more interaction between the material and water vapor, potentially leading to higher hygroscopic expansion [23].
- **Geometrical Parameters**: shape and size, irregularity can influence differently the interaction with moisture; thinner materials may absorb moisture more readily compared to thicker ones, as water molecules can diffuse through them more easily; anisotropic materials may exhibit different hygroscopic expansion coefficients depending on the direction of expansion [24].

The time propagation of water in hygroscopic tissues is in first approximation mediated by Fickian diffusion mechanism , which is intrinsically restricted by poroelastic limit [25]. Micro and mesostructures in the material (porosity), as well as the chemical nature of the material, will determine the effective diffusivity of the structure, and so the sensitivity to relative humidity variation [25].

1.2.2 The State-of-Art in Hygroscopic materials and structures for soft robotics

In the perspective of robotics development, it is possible to start from biological examples of inspiration, categorizing hygroscopic actuation systems in fungi and plants into four different groups: cell growth, turgor pressure, cohesion force, and cell wall swelling [26]. Each of these mechanisms leverages different physical phenomena, offering valuable insights for engineering design. Skotheim and Mahadevan [27] conducted an extensive examination of the physical constraints and design principles underlying plant motion. They introduced a spatial-temporal map that categorizes plant motion into three main groups: snap-buckling dominated, swelling/shrinking, and explosive fracture dominated. This represents a compelling roadmap for bioinspired design, as the design of robots is intricately linked to both temporal and dimensional scales (Figure 1.3).

Inspired by this natural mechanism, several studies have been reported in the literature with the aim of understanding and using the hygroscopic effect as a sustainable source of actuation. Considering tissue expansion, the basic principle of hygroscopic actuation is based on the coupling of materials with different moisture sensitivity, resulting in different hygroscopic deformation along their geometric configuration. The principle can be easily described through a double layer structure, in which one side is completely hydrophobic (passive layer) and

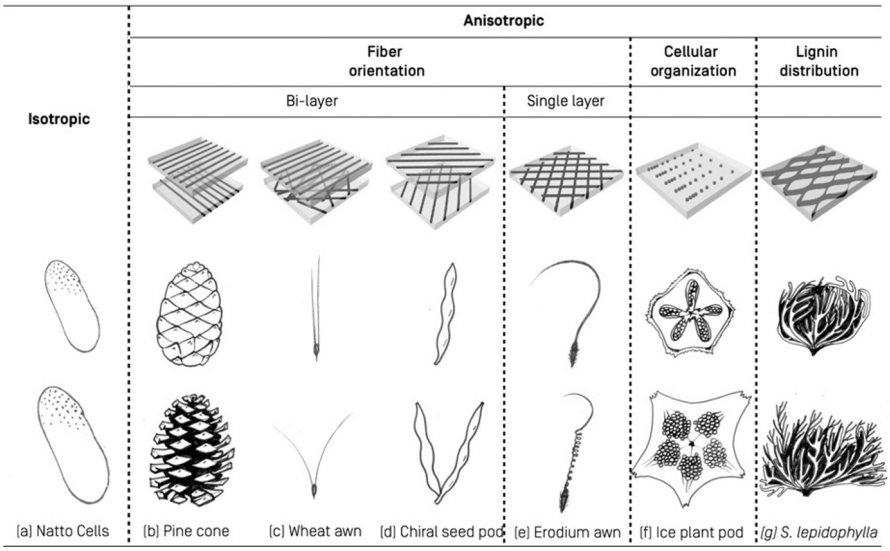

Figure 1.3: The categorization of hygromorphic plants and microorganisms based on the actuation mechanisms. (A) Living bacteria, natto cells, expand and contract within subseconds. (B) Pine cone scales bend during a duration of hours. (C) Wheat awns bend during a duration of a few minutes. (D) Chiral seed pods coil into a helix during a duration of minutes. (E) Erodium awns drill into a helix during a duration of minutes. (F) Ice plant seed pods unfold during a duration of minutes. (G) S. lepidophylla coils into spirals during a duration of hours. Reprinted after request with Copyright [17].

it is perfectly bonded with an hygroscopic material (active layer), with isotropic expansion properties. When the amount of environmetal relative humidity increases, the active layer starts to expand, generating an hygroscopic strain. The intrinsic variation of strain along the thickness direction of the bilayer will determine bending. The same concept can be generalized for anisotropic actuation systems, which will provide according to the direction of expansion a superposition of bending and twisting. Moreover, one of the most interesting inherent advantages of hygroscopic actuators is their temperature dependence. In the case of gaseous water, considering a condition of constant partial pressure, an increase in temperature determine water desorption in the hygroscopic material. It is possible to exploit this assumption to realize hygroscopic actuators that can be controlled through electronic sources that dissipate heat by the Joule effect (electrothermal effect) or by exploiting the absorption of electromagnetic radiation to locally increase temperature (photothermal effect).

In 2015 was fabricated the first electrically controllable hygromorphic actuator [28]. The authors present a double-layered humidity-driven actuator realized through solution-casting method, depositing an active layer of PEDOT:PSS and a passive layer of poly(dimethylsiloxane) (PDMS). Exploiting the combination of hygroscopicity and electrical conductivity of PEDOT:PSS, the authors were able to directly control both by Joule effect or by environmental humidity variations the reconfiguration of simple structures, as a miniaturized robotic hand (Figure 1.4A).

In 2018, it was presented the first locomotion robot based on hygroscopic effect [29]. Authors exploit the moisture expansion mechanism of aligned Polyethileneoxide (PEO) fibers, fabricated through electrospinning technique, deposited on a Polyimide (PI) inactive substrate. The actuator exploits asymemtric friction coefficient of the ratchets to rectify oscillatory bending motion in a directional locomotion (Figure 1.4B). Furthermore, they mathematically analyzed the mechanical response of the hygrobot, which allowed the prediction of its performance but also to optimize the design and to maximize the locomotion speed given geometric and environmental constraints. The advantage of using the electrospinning approach consist in realizing high surface to volume ratio microfibers, cohesive to form a highly porous structure. Hence, this additive manufacturing technique increase the CHE as well as the diffusivity of hygroscopic material, and so it will increase the sensitivity and the performances of

Table 1.1: State-of-Art of hygroscopic-mediated actuator. The actuator are classified according to manufacturing technique, materials involved, mechanical assembly of the structure, proposed application.

Manufacturing	Materials	Structure	Application	Reference
Solution-casting	PEDOT:PSS PDMS	Bilayer	Robotic hand, bending	[28] (2015)
Electrospinning	PEO PI	Bilayer	Crawler	[29] (2018)
Electrospinning	PEO PDMS	Bilayer	Bistable bending	[30] (2020)
Photolithography	Liquid crystal RM82 and DMEN	Bilayer	Bending, twisting, manipulator	[31] (2021)
Microfluidic	ETPTA Diatomite-laden alginate fiber	Discontinuous microparticles embedded in hydrogel fibers	Lifting, bending, twisting	[32] (2021)
Stereolithography	Fullcure705 in FLX930 elastomer	Bilayer of spring and square tubes embedded in hygroscopic polymer	Bending, twisting, manipulator	[33] (2022)
Layer-by-layer assembly	MXene ($Ti_3C_2T_x$) Cellulose fibers	Hierarchical gradient	Crawler, reconfigurable structure	[34] (2020)
Film coating	MXene (Ti_3AlC_2) Cellulose, PEDOT:PSS, PTFE	Bilayer	Crawler, Finger bending sensor, Breathing sensor	[35] (2022)
Film coating	MXene ($Ti_3C_2T_x$) Paper, PE	Bilayer	Manipulator, Touching sensor	[36] (2022)
Drop casting	PEDOT:PSS Graphene	Hierarchical gradient	Reconfigurable structure	[37] (2023)
FDM Electrospinning	PEO, CNC PCL	Bilayer	Bending, twisting, lifting, soil exploration	This Ph.D Thesis [38] (2023)
DIW	CMC, PVA AgNPs, PDMS	Trilayer	Bending, twisting, crawling, lifting, uniaxial motion	This Ph.D Thesis [39] (2023)

the actuator.

Using the same electrospinning approach, hygroscopic bistable structures were demonstrated [30], depositing PEO nanofibers in prestretched PDMS substrate. Following a bilayer approach, an aligned liquid crystal elastomer (LCE) anisotropic actuator was demonstrated [31]. The hygroscopic LCE was synthesized using an aza-Michael addition reaction between a reactive LC monomer and N-dimethylethylenediamine as a chain extender, followed by photo-polymerization. In particular, authors showed the possibility to manipulate the oriented hygroscopic material to realize bending and twisting actuator, with arbitrary configuration (Figure 1.4C).

Table 1.2: Mechanical properties of state of art hygroscopic-mediated actuator. The table classification is made according to input stimulus (variation of relative humidity, temperature, voltage applied, irradiance), material toughness, bendability (variation of curvature), force and response time, material figure of merit (coefficient of hygroscopic expansion and water diffusivity coefficient).

Input Stimuli	**Storage Modulus [MPa]**	**Curvature Variation [cm^{-1}]**	**Response Time [s]**	**Force [mN]**	**CHE**	**Diffusivity [$m^2\ s^{-1}$]**	**Reference**
ΔV = 20 V @RH?	2.28	4	10	0.3	-	-	[28] (2015)
ΔRH = 60%	170	1	2	-	0.05	1×10^{-11}	[29] (2018)
ΔRH = 60%	Dry 50 Wet 1	2.5	6	-	0.12	1.5×10^{-10}	[30] (2020)
ΔRH = 60%	38	5	-	-	-	-	[31] (2021)
ΔRH = 60%	Dry 2500 Wet 3	0.6	30	800	-	-	[32] (2021)
ΔRH = 60%	0.3	0.5	1	-	-	-	[33] (2022)
ΔRH = 50%	8500	-	7	0.4	-	1.42×10^{-11}	[34] (2020)
ΔRH = 5%	-	2	-	-	0.047	-	[35] (2022)
I_0 = 300 mW/cm^2 @ RH?	-	1	-	-	-	-	[36] (2022)
ΔV = 1.5V RH = 55%	1320	2.03	100	-	-	-	[37] (2023)
ΔRH = 60%	300	6	123	13	0.12	4.70×10^{-11}	This Ph.D Thesis [38] (2023)
I_0 = 100 mW/cm^2 @ RH = 50%	2	2	5	0.8	0.03	2.94×10^{-11}	This Ph.D Thesis [39] (2023)

Recently, two different approaches for the realization of hygroscopic actuators have been demonstrated by working on new structural paradigms. One efficient solution was provided by Pingan Zhu et al. [32]: inspired by tendrils of climbing plants, they fabricate using a microfluidic approach a diatomite-laden hygroscopically responsive fibers with a discontinuous ribbon of stiff, asymmetrically shaped, and hygroscopically inactive microparticles embedded inside. Driven by hygroscopic variable stiffness, the actuator changes its storage modulus from dry to wet condition by 1000%, delivering a force of about 800 mN.

Investigating the tissue structure of pinecones, Zhang et al. [33] discovered that the structural feature that permits the hygroscopic deformation was related to vascular bundles with unique parallelly arranged spring/square microtubular heterostructure. Inspired by this structural features, the authors manufactured a soft actuator, combining a spring/square shaped elastomer with embedded hygroscopic material (Figure 1.4D).

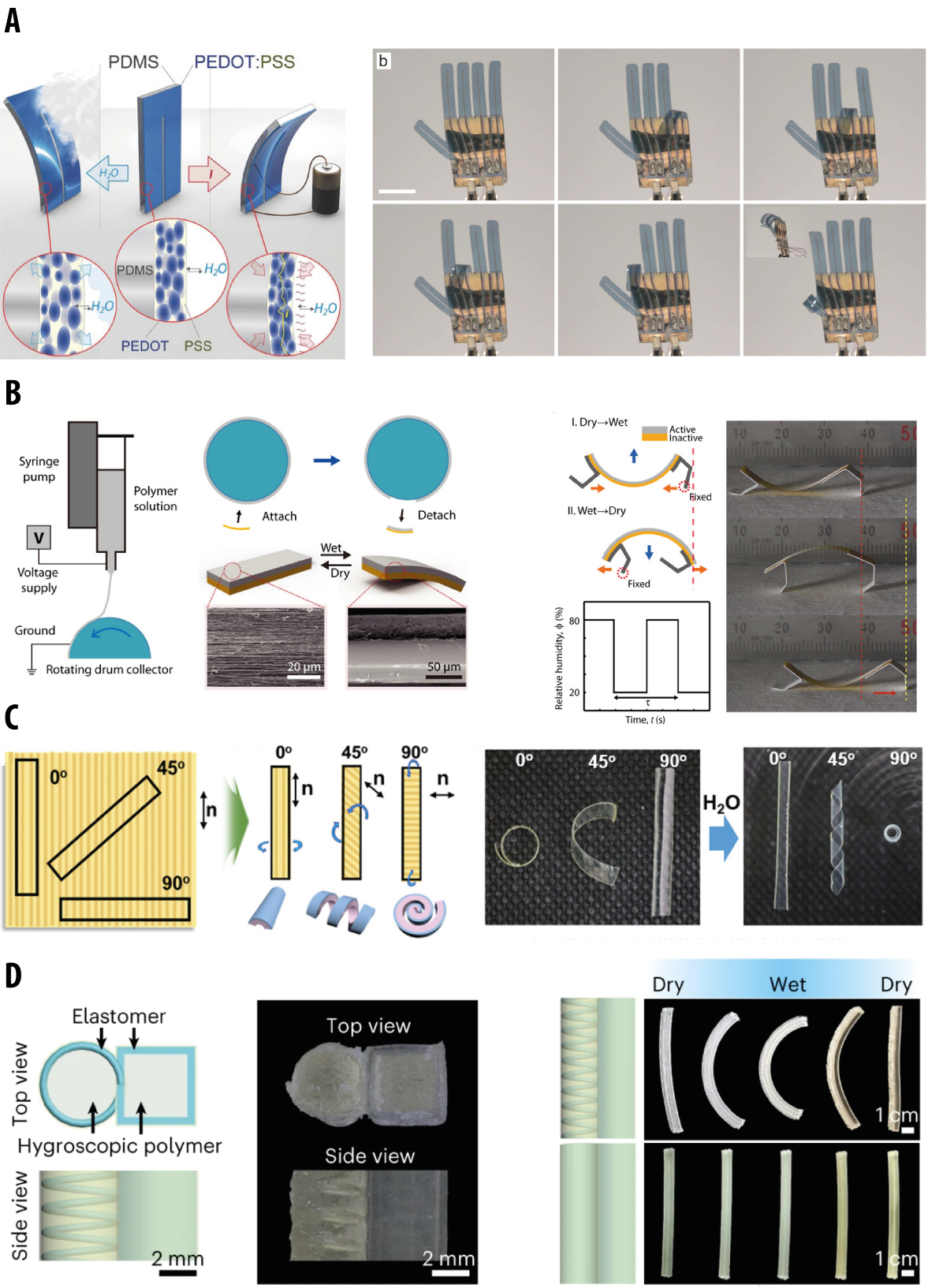

Figure 1.4: Examples of State of art of hygroscopic soft actuators. A) First hygroscopic and electrothermal actuator, with an example of a soft robotic hand [28]. B) Hygrobot: A self-locomotive ratcheted actuator powered by environmental humidity. We reported the electrospinning fabrication procedure and an example of hygroscopic locomotion [29]. C) 4D Printing of Hygroscopic Liquid Crystal Elastomer Actuators. Exploiting the deposition and orientation of hygroscopic liquid crystal element, the authors provided an example of bending and coiling soft actuator [31]. D) Pinecone inspired bending actuator, realized as a combination of spring and square tubes, with embedded in hygroscopic polymer [33]. Reprinted after request with Copyright.

The inclusion of photothermal properties in hygroscopic structures permits to power the actuator from the environmental illumination as a wireless system, without requiring any battery onboard. Since this solution is very attractive for robotics applications, several solutions using photothermal effect have recently been proposed in the literature. The standard figure of merit for photothermal effect is the photothermal conversion efficiency (PCE), which express the amount of radiative electromagnetic energy is converted into heat. The most promising materials that shows PCE of $\simeq$ 90% are MXenes [34–36] and graphene [37]. For instance, Zhao et al. [35] propose a bilayer structure composed by MXene costed-paper and polyethylene (PE). The multi-responsive actuator shows potential as smart gripper with application in soft robotics, and bionic prosthesis. Finally, it is possible to combine together hygroscopic, electrothermal and photothermal properties of materials to maximize the fields of application of these soft actuators. An example was provided in 2023 matching the hygroscopic properties of PSS:PEDOT with photothermal and electrothermal features of graphene [37].

We report in Table 1.2 a selection of the structural and material properties of the state-of-the-art hygroscopic actuator. The key characteristics of hygroscopic materials that represent the figure of merit are water diffusivity and CHE. It is important to note that these parameters are influenced not only by the chemical nature of the hygroscopic element, but also by the micro- and meso-structure at the tissue level. However, the mechanical design of the hygroscopic actuation system plays a key role, where the elastic modulus and the dynamic curvature variation are critical for soft robotic applications.

Finally, considering that hygroscopicity is inherently limited by the enthalpy variation of water adsorption, a trade-off between force/momentum and response time is well defined. The solution should be sought in new structural and chemical approaches, where bioinspiration is an appropriate starting point for design.

1.2.3 Thesis overview

This thesis addresses the need for biodegradable solutions for the realization of autonomous soft robots that can disperse in the environment to perform various monitoring and restoration tasks in environments not accessible to human operators, reducing the accumulation of waste in ecosystems.

We approached the challange by drawing inspiration from the natural world, particularly from the hygroscopic actuation mechanism of Erodium and Pelargonium seeds. These seeds are a remarkable example of the principle of least action, mediated by the evolutionary process of natural selection. The significance of this lies in the fact that these movements are executed with a finesse that minimizes exergy variation, a characteristic that we seek to emulate and harness in the development of sustainable actuation systems.

Considering the state of the art, we propose for the first time fully biodegradable solutions for the realization of hygroscopic actuators, combining together additive and subtractive manufacturing techniques. This required an interdisciplinary approach, starting from biomechanical analysis, moving through material selection and subsequent manufacturing and testing. Furthermore, we clarify a methodology for structural and performances characterization of hygroscopic actuators. We sought to elucidate the various characterization processes that can outline a protocol for the development of hygroscopic multilayer actuators.

The thesis was structured as follows.

In the first chapter, we provide a detailed examination of the Erodium and Pelargonium seeds, as reference of bioinspiration. We explore how these seeds disperse into the environment, shedding light on the unique features of their internal tissue organization that enable hygroscopic actuation. A comprehensive biomechanical analysis is conducted to understand the principles behind the movement triggered by humidity changes. We reported the same analysis published on a mini-review, in which are described the parameters necessary to undertake a biomechanical study of hygromorphic seeds (Morphological Computation in Plant Seeds for a New Generation of Self-Burial and Flying Soft Robots, DOI: `10.3389/frobt.2021.797556`). For the sake of completeness, we report also in this chapter the original results of the histological analysis for the natural hygroscopic actuator, to better highlight the bilayer nature of the seed's awn. Note that all histological analyses were performed by colleague Dr. Marilena Ronzan.

Moving forward, we present a suitable model to design and predict the behavior of helical cylindrical hygroscopic actuators. These deformable actuators are subjected to bending and torsion due to their inherent geometrical features. Starting from the kinematic model provided by Ha et al. [40], we utilize the laminated composite plates model to predict the kinematic deformation of the awn as function of relative humidity, specifically focusing on pitch and radius variation. Respect to the previous model reported in literature, we correct some formal analytical description, defining also the geometrical limit of validation for mid-curve reconstruction [41]. Additionally, we include a new description of static performances for the actuator (extensional force and torque) coupling the kinematic prediction with spring theory. To aid in practical applications, a Matlab script for predictive modeling is provided.

Next, we compile a collection of articles that have been published during the course of this Ph.D. research. Note that we have faithfully reported the materials

and methods sections, experimental results and images to the published articles. These articles showcase the practical application of bioinspired hygroscopic and photothermal actuation principles:

- **4D printing of Biodegradable Seed-Inspired Soft Robot**: this research resulted in the development of a biodegradable soft robot inspired by *Pelargonium appendiculatum* seeds. Starting from the literature results, we proceed to complete the biomechanical characterization of natural seed to extrapolate parameters for modeling of hygroscopic actuator. We provide a sustainable solution in manufacturing the first biodegradable hygroscopic robot, coupling together FDM printing with electrospinning. Moreover, we first present an high efficient hygroscopic material using coaxial electrospinning approach. The soft robot serves a dual purpose, functioning as an energy autonomous device for soil exploration and for hygromechanical visual humidity sensing (4D Printing of Humidity-Driven Seed Inspired Soft Robots DOI: 10.1002/advs.202205146, An autonomous biodegradable hygroscopic seed-inspired soft robot for visual humidity sensing DOI: 10.1016/j.matdes.2023.112408).

- **Photothermal-Hygroscopic Actuator**: we introduce a photothermal-hygroscopic actuator designed to operate under sunlight irradiance conditions. The general idea was to develop a surface functionalization tool, which permits to induce bending and torsion powered by a wireless and renewable source, as sunlight. Furthermore, this apporach permits to increase the power density and the actuation speed in hygroscopic actuator. The actuator harnesses both photothermal and hygroscopic effects to achieve sustainable and autonomous operation (A Bioinspired Plasmonic Nanocomposite Actuator Sunlight-Driven by a Photothermal-Hygroscopic Effect for Sustainable Soft Robotics DOI: 10.1002/admt.202202166).

- **Biodegradable photothermal actuator based on thermal expansion**: we present a preliminary prototype that utilizes biodegradable materials and exploits the thermal expansion of a polymer, coupled with wireless and sustainable actuation through photothermal effect. The biodegradable active material is based on lignin, which was homogeneously dispersed in polycaprolactone, allowing the blend to be FDM printed with three-dimensional geometries. This prototype demonstrates the feasibility of creating sustainable actuators with low environmental impact (Bioinspired Soft Actuator Based on Photothermal Expansion of Biodegradable Polymers DOI: 10.1007/978-3-031-38857-6_12) .

In conclusion, this Ph.D. thesis is a comprehensive exploration of sustainable actuation systems inspired by Erodium and Pelargonium seeds. Our research has led to the development of innovative actuators and sensors with low environmental impact, making significant strides in the direction of sustainability in technology. These contributions are expected to have a lasting impact on the field of bioinspired technology and sustainable engineering.

Note that all the non-original pictures are reported and reprinted after request with Copyright.

The Geraniaceae seeds: Pelargonium and Erodium genera

2

In this chapter, we will focus on self-burying seeds, in particular the seeds of the Geraniaceae family, which includes 841 species and 7 genera of annual and perennial herbs [42]. The Geraniaceae seeds (e.g., Erodium or Pelargonium genus') combine explosive dispersal strategy with a hygroscopic motion to promote germination, providing autonomous motion on terrain surface and penetration into soil fractures.

2.1 Morphology, structure and composition

Geraniaceae fruits generally have a five-carpelled schizocarp and a central axis called columella. Each carpel has a mericarp structure, which contains the seed, and a sterile robust tissue called awn, that extends along the central axis [43]. Differentiation in the family on the seed dispersal mode has led to a seed dispersal classification: the 'Erodium-type' (ET), the 'seed-ejection type' (SE), the 'carpel-projection type' (CP), and the 'inoperative type' (IT) [43, 44].

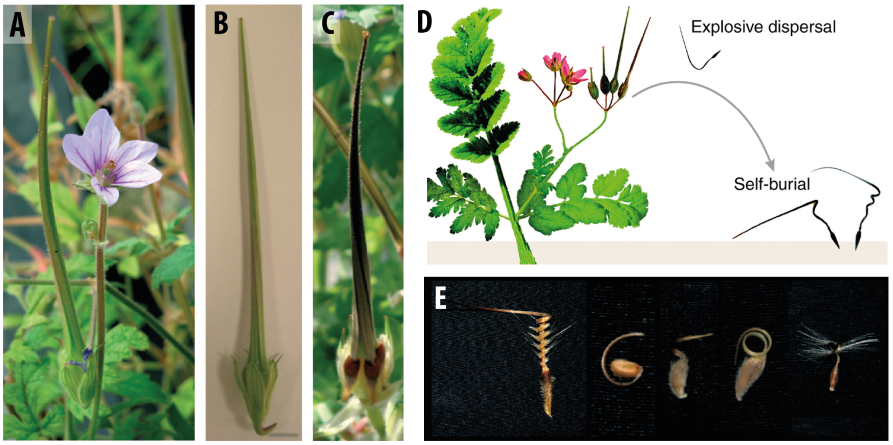

Figure 2.1: The Erodium-type plant family. A) Erodium gruinum flower and beak-shaped fruit. B) The 'beak' of the fruit consists of five awns attached to the seed capsule at the base of the fruit. C) As the fruit ripens, the awns dehydrate and induce a twisting deformation of the fruit 'beak'. [14] D) Erodium cicutarium launches seeds up to half a meter using energy stored elastically in a coil-shaped awn that is held straight before dehiscence. The awns subsequently bury the seed by drilling, as they wind and unwind with changes in ambient humidity. [16] E) Examples of Geraniaceae dispersal units (left to right): Erodium gruinum, Geranium pusillum, Geranium dolomiticum, Geranium reflexum, Pelargonium peltatum [14]. Reprinted after request with Copyright.

Erodium-type (ET) discharge, called after the genus Erodium, is characterized by an explosive launch in the air, in dry conditions, of the awn and mericarp fused. After detachment from the columella, the awn rapidly coils to its natural form releasing the mechanical energy previously stored (Figure 2.1). Once on the ground the hygromorphic awn can coil and uncoil in response to humidity changes and facilitating its self-burial [43, 45] (Figure 2.2).

ET discharge was suggested to be the most primitive dispersal mode, from which the other types originated [44], and is present in other genera of the family with some modifications occurring in the post-dehiscence processes of dispersal and seed burial [43]. Crawling and burying occur thanks to the hygroscopic seed helical unit (the awn) that responds to variations of external humidity by changing its configuration. In the Pelargonium genus, the structure of the awn is lighter and thinner, covered with feather-like hairs compared to the Erodium genus. This difference was explained as a condition necessary for the detachment from the columella through wind dispersal instead of being

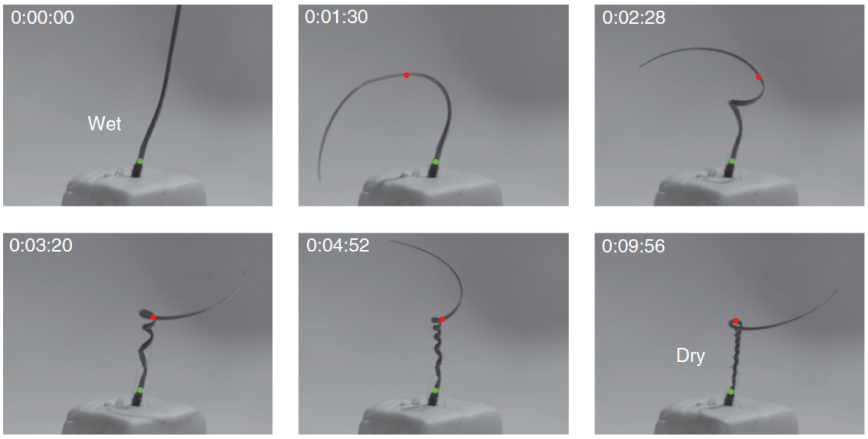

Figure 2.2: Representative example of Erodium cicutarium's awn re-winding upon drying. Green and red dots mark the proximal (seed) and distal ends of the actively bending region. Time is expressed in hh:mm:ss [16]. Reprinted after request with Copyright.

sprung away as Erodium seeds [14]. However, similarly to Erodium, once on the ground the awns start to coil in response to humidity, suggesting that the microstructure composing the awn especially, has evolved to function for self-burial only [45].

Erodium and Pelargonium seeds present a global structure in which three different sections can be distinguished , in terms of morphology and biological function (Figure 2.3): 1) the capsule, containing the seed embryo, which anchors the structure into the soil and converts rotational motion into burial behavior through anisotropic friction; 2) the awn, which acts as an independent hygroscopic actuator, thanks to the helical arrangement of cellulose microfibrils along the cells; the ventral part of cylindrical helix is the cap layer, while the dorsal one is the ridge layer; 3) the lever, which functions as a passive element that allows the self-lifting of the seed and applies torque, exploiting the intrinsic friction to act as an anchoring element (Figure 2.3) [38].

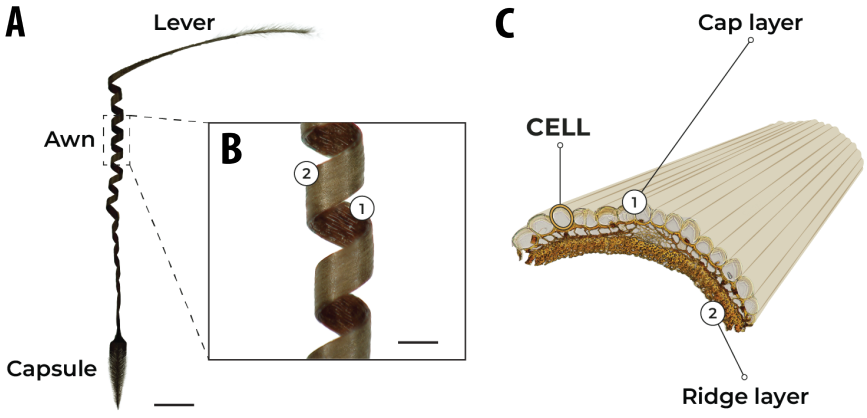

Figure 2.3: Morphological description of the awn in P. appendiculatum. A) Optical image of P. appendiculatum. Scalebar 5mm. B) Optical magnification of the awn. Scalebar 500 μm. C) Scheme and nomenclature of awn [38].

A focus on the awns coiling behavior has led to studies on the morphology and internal structure of Erodium and Pelargonium genus. The coiling deformation was attributed to specialized cells containing tight helices of cellulose microfibrils [14]. A difference in the composition and distribution of materials along the awn was observed, with a higher concentration of modified lignin on the cap layer of the awn and a lower concentration of modified lignin in the ridge layer, which increases the hydrophobicity of the cell walls [46].

In Pelargonium seeds, the awn is composed of a bilayer structure with the hygroscopically active cells aligned along a layer of inactive cells [29, 45]. The cell

in cap layer are characterized by an arrangement of cellulose microfibrils with a helix shape, where the helix axis is tilted with respect to the cell axis. We then report original results of histological analysis of Pelargohium and Erodium awn. In Figure 2.4, alcian blue histochemical stain shows the asymmetric localization of cellulose in the internal tissue of the awn, while lignin distribution was confirmed in all tissue, especially sclerenchyma, by its auto-fluorescence with blue light excitation (488 nm). In this frame, the ridge layer enacts the role of a hydrophobic passive substrate that prevents delamination of cellulose due to water solubilization. In the lever region, the sections lose their string shape, for a rounder one, with the inner tissue having a smaller cell size and the sclerenchyma tissue more extension in comparison to the awn. Since the concentration of cellulose is uniformly distributed, the lever is a non-hygroscopic element of the structure [38].

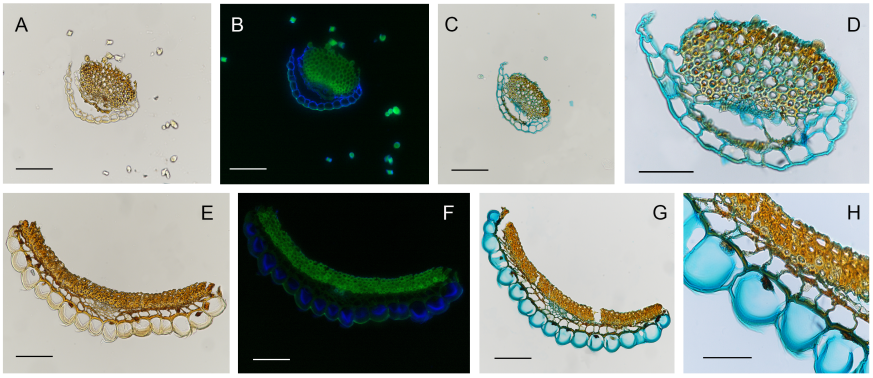

Figure 2.4: Histological analysis of Pelargonium appendiculatum awn and lever by bright field and fluorescence microscopy. Transversal sections of the lever (a, b, c, d) and awn section (e, f, ,h, g). Scalebar is 100µm for (a, b, c, e, f, g). Scalebar is 50µm for (d, h). [38]

The main differences between Pelargonium and Erodium genus, are the cell structure, the morphological distribution of cellulose and the material distribution in the awn. The Erodium cap layer is characterized by sclerenchyma cells (short rectangular cells with thick cell walls) with thick symmetric cell wall deposition, while the ridge layer is mainly composed by fibrous cells. The variable distribution of acidic polysaccharides and cellulose are higlighted with blue stain in Figure 2.5 [38].

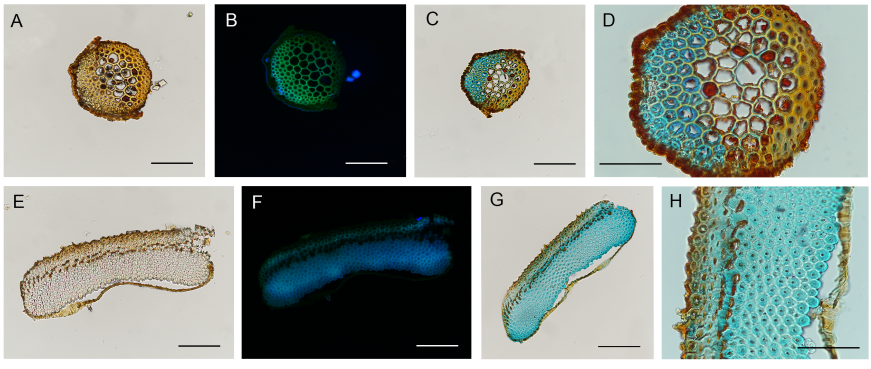

Figure 2.5: Histological analysis of Erodium malacoides awn and lever by bright field and fluorescence microscopy. Transversal sections of the lever (a, b, c, d) and awn (e, f, g, h). Bars = 100µm (a, b, c, e, f, g), 50µm (d, h). [38]

In both genera, the capsule plays a fundamental role in the anchoring of the seeds into the soil surface irregularities, such as crevices, which are then used by the seed to penetrate into it [16, 47]. For instance, the capsules of Erodium cicutarium seeds showed a hooked, tapered carpel-tip which are fully covered from stiff directional hairs [47]. Erodium capsules were structurally modified (e. g. hairs were removed with sandpaper, or tips were cut off) to investigate how the presence of hairs or tips affect the establishment of the seeds into soil substrates with different crevices sizes. The depths of burial, which indicates

the height of the seed capsule above the substrates, were measured in both unmodified and modified seeds and in small or large crevices, showing that depths of Erodium seeds with unmodified capsules were greater in small crevices [47]. By using Scanning Electron Microscopy (SEM) investigations, directional hairs-like microstructures were found also in other seeds families (e. g. Poaceae), where they may help the seeds to move as a ratchet into the soil [15].

2.2 Biomechanics of the awn

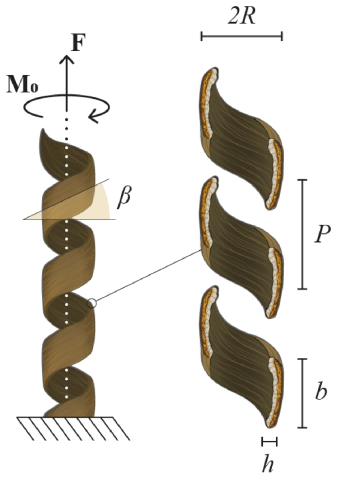

Figure 2.6: Schematic representation of geometrical parameters involved in the static evaluation of extensional force F and bending plus torque M_0. [38]

The helical movement of Gerianaceae's awn can be geometrically described by measuring the pitch (P) and radius (R) values of the helix during relative humidity changes [40]. Coiling and uncoiling of the awns of Erodium and Pelargonium seeds result in rotation and consequent digging of the seed in the soil fractures. Both movements are promoted by two different biomechanical effects: a force due to coil extension and torque caused by awn-tail rotation (Figure 2.6).

Due to its compositional and morphological nature, in first approximation the awn of Pelargonium and Erodium species can be split into an effective bilayer, which makes it more suitable for the design and bioinspiration of an artificial equivalent seed based on bilayered hygroscopic theory and structure [40, 48].

The metabolically inactive tissues in the awn are responsible for the passive movement of the seed, characterized by a combination of bending and torsional deformation. This occurs thanks to the internal hierarchical structure of the awn, described as a composite material, in which the hygroscopic active element (crystalline cellulose microfibrils) is embedded in a hygroscopic passive soft matrix of structural proteins, polysaccharides and aromatic compounds. Cellulose shows hydrophilic moiety, allowing water molecules to store between intermolecular hydroxyl groups via hydrogen bonding. Therefore, water adsorption determines a volumetric transversal expansion of cellulose tissues. The volume increase between intermolecular chains or networks leads to the swelling of wet tissues. Because water adsorption is a reversible process, the swollen tissue of the seed can shrink back to its initial size when dried [38].

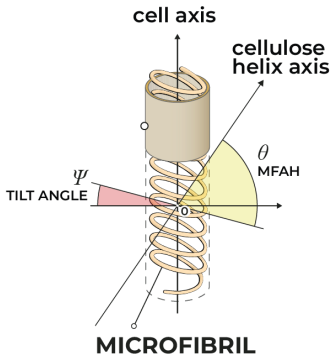

Figure 2.7: Cellulose microfibril distribution and definition of the characteristic angles. [38]

The cellulose microfibrils in the cell wall of these cells form a tilted helix configuration, in which the helix axis is at an angle to the cell's long axis. The microfibrils organization permits to define two angles defined with respect to the cell longitudinal axis, the microfibril angles (MFA). In literature it is also proposed another representation of the MFAs, where instead of using as reference the cell's axis, we use the microfibril helix axis. We define, the tilt angle Ψ, which is the angle between the cellulose helix axis and the cell's long axis, and the cellulose microfibril angle in relation to the cellulose helix axis (MFAH) Figure 2.7. Note that when $\Psi = 0$, the helix axis corresponds to the cell's axis. The cellulose microfibril orientation in isolated layer should be measured using small angle or wide angle X-ray scattering [49].

To define a reference axis in the measurement, the sample is positioned with awn's longitudinal axis perpendicular to the X-ray beam. Considering that the cells are aligned parallel to the awn axis, the microfibrils are tilted in helix arrangement within the cell wall. Moreover, the cellulose tilting direction is uniform in all cells, justifying the fact that this arrangement facilitated the cooperative way by which the cells induce the macroscopic coiling of the

Table 2.1: Values of the tilt angle and the cellulose microfibril angle in relation to the cellulose helix axis (MFAH) of cellulose microfibrils from the five Geraniaceae species, measured by small-angle X-ray scattering (SAXS) [14, 40].

	Erodium grunium	*Geraniuim pusillum*	*Geranium dolomiticum*	*Geranium reflexum*	*Pelargonium peltatum*	*Pelargonium appendiculatum*
Tilt angle [deg]	20	0	<3	0	19	15
MFAH [deg]	67-80	13-35	75	19	70	70

awn [49]. In table are reported the values of microfibril angles in the cap layer of different Geraniaceae species, characterized using Small Angle X-ray Spectroscopy (SAXS) [14, 40]. To reconstruct the microfibril angles from tilt angle (Ψ) and MFAH (θ), we recall the geometrical definition [40]: $\text{MFA}_1 = \Psi - \theta$ and $\text{MFA}_2 = \Psi + \theta$.

Considering that the stress generated in the structure is only dependent on hygroscopic swelling, the whole stress can be modeled according to $\sigma_h = D\alpha\Delta\phi$, where σ_h is the hygroscopic stress, D is material stiffness, α is Coefficient of Hygroscopic Expansion (CHE), and $\Delta\phi$ is the variation of RH in relation to humidity saturation concentration. Moreover, the coiled arrangement of hygroscopic active element (cellulose microfibril) will determine an anisotropic hygroscopic strain.

The CHE was measured only for Pelargonium appendiculatum using a thermo-hygrostat [40]. The measured value was comparable to the measured one by Dawson et al., 1997 [19], which studied the opening of the pinecones with a hygromorphic actuation mechanism similar to the Geraniaceae one. In particular the ventral/cap layer shows $\alpha_c = 0.06 \pm 0.02$, while the CHE of dorsal/ridge layer is $\alpha_r = 0.20 \pm 0.04$.

The different stiffness of the two layers were not measured so far in literature. However, Evangelista et al., 2011 took provides in their modeling dissertation on of Erodium cicutarium, a Young's modulus = 9 GPa; Poisson's ratio = 0.33, shear modulus= 3.4 GPa [16]. The value of Young's modulus E was measured also in the wild wheat awns [15], finding values that range from 10 GPa at the ridge, to 20.5 GPa at the cap, where lignin is more abundant.

For what concerns the static parameters of the natural hygroscopic actuator, few investigation were reported in literature. Coiling and uncoiling of the awns of Erodium and Pelargonium seeds result in rotation and consequent digging by the seeds. Digging arises from two different mechanical effects: force due to coil expansion and torque due to awn-tail rotation. The forces are exerted against a support provided by pebbles or bark of trees in nature [47]. Uncoiling of a helical structure into a straight configuration leads to a change in length along the axis of the helix, and thrust (F) is exerted normal to the surface of the soil. In addition, the relative rotation of the helical structure to the tip of the long tail produces torques (M_0 = r T, where r is the length of the lever). The thrust and torque together are responsible for self-burial of the seed. Jung et al., 2014 measured, with a load cell, the extensional force of Pelargonium carnosum by constraining the increase in length with the increase of humidity [45]. The authors also measured the torque by obstructing, with a load cell, the awn rotation during wetting. The maximum force was 1 mN and the torque 20 $\mu N \times m$ (moment arm 20 mm). The authors proved that the torque decreased in magnitude over time, consistently with the decrease of Young's modulus with increasing water content in the awn's tissues [45].

Mechanical modelling of bilayer hygroscopic actuators

3

The manipulation of materials to harness their unique properties for engineering applications has been a longstanding pursuit in the realm of biomimetic design. Nature has provided a plethora of intricate and efficient solutions to various challenges, inspiring the development of novel technologies across diverse disciplines. One captivating example of such natural ingenuity lies in the fascinating behavior exhibited by Geraniaceae seeds, specifically their hygroscopic response to changing environmental conditions. These seeds, found within the Geraniaceae family, exhibit a remarkable ability to undergo controlled deformations in response to variations in humidity. This ability has sparked interest in understanding and replicating the underlying mechanisms for the creation of advanced hygroscopic and thermal actuators.

In the pursuit of emulating this captivating phenomenon, this chapter delves into the comprehensive mechanical modeling of the kinematic and static descriptions in hygroscopic bilayers. The foundation of this study rests upon the inherent linear elastic properties of the materials involved, ensuring that the deformation remains within the confines of the linear elastic regime. Additionally, we assumed that the body deformation occurs predominantly in the thickness direction, simplifying the modeling approach.

The bioinspiration drawn from the Geraniaceae seeds' behavior serves as a guiding principle for this study. These seeds exhibit a coiling behavior in response to changes in relative humidity, wherein their awn undergoes helical cylindrical deformation. The focus of this research is to use laminate composite plates model for strips in stretching-regimes, that permits to correlate the variation in the radius and pitch of this helical coiling with changes in relative humidity. By gaining insights into this relationship, it becomes possible to harness this behavior to design novel hygroscopic actuators with tailored performance characteristics.

To assess the static performance of the natural actuator, the principles of helical cylindrical spring theory will be employed. This approach allows us to quantify the actuator's behavior in terms of extensional force and torque, and potential application scenarios. By correlating the model's predictions with experimental observations from the Geraniaceae seed, we can validate the efficacy of the proposed modeling approach. With a rigorous understanding of this behavior, it becomes feasible to analyze and predict the deformation patterns exhibited by the hygroscopic bilayer, thereby paving the way for the design of artificial actuators with controlled and reproducible behaviors. The implications of this research offer a pathway towards the creation of advanced artificial hygroscopic and thermal actuators with unprecedented potential for applications in engineering, materials science, and beyond.

3.1 Kinematic prediction: Laminate composite plates

A laminate composite plate is a structural material made by layering multiple thin sheets or layers of different materials to create a single, unified structure with enhanced mechanical properties. These materials are typically composed of high-strength fibers embedded in a matrix material. The combination of these layers results in a composite material that takes advantage of the individual strengths of each component while minimizing their weaknesses. To model the behaviour of a laminate composite, we assume that:

- The layers are perfectly bonded;
- Each layer is homogeneous;
- Individual layer properties can be isotropic, transverse isotropic or orthotropic;
- Each layer is in a state of plane stress;
- The laminate deforms according to the Kirchoff assumptions (thin layers): normals to the midplane remain straight and normal to the deformed midplane after deformation; normals to the midplane do not change length.

Considering an isotropic linear elastic material, the Cartesian strains resulting from a state plane stress ($\sigma_z = \tau_{xz} = \tau_{yz} = 0$) are:

$$\epsilon_x = \frac{1}{E}\left(\sigma_x - \nu\sigma_y\right)$$

$$\epsilon_y = \frac{1}{E}\left(\sigma_y - \nu\sigma_x\right)$$

$$\gamma_{xy} = \frac{1}{G}\tau_{xy}$$

where E is the Young's modulus, ν the Poisson's ratio and G the shear modulus. Using the matrix notation, these relations can be written as:

$$\begin{Bmatrix}\sigma_x\\ \sigma_y\\ \tau_{xy}\end{Bmatrix} = \frac{E}{1-\nu^2}\begin{bmatrix}1 & \nu & 0\\ \nu & 1 & 0\\ 0 & 0 & (1-\nu)/2\end{bmatrix}\begin{Bmatrix}\epsilon_x\\ \epsilon_y\\ \gamma_{xy}\end{Bmatrix} \tag{3.1}$$

where G has been replaced by $E/2(1+\nu)$.
If the material has a unidirectionally-renforced fiber composite, the elastic constitutive laws must be modified to account this anisotropy. Let's refer to an arbitrary coordinate system $(1, 2)$ (Fig.3.1B), called *principal material directions*, which represent respectively the direction along and transverse to the fiber axes.

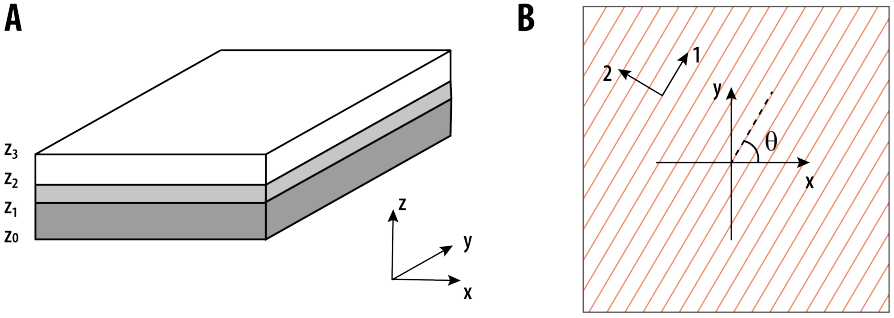

Figure 3.1: Schematic representation of multi-layer laminate composite plates. A) Reference Cartesian coordinates. B) Principal material directions.

Hence, the constitutive relation can be written as:

$$\begin{Bmatrix} \sigma_1 \\ \sigma_2 \\ \tau_{12} \end{Bmatrix} = \begin{bmatrix} E_1/(1-\nu_{12}\nu_{21}) & E_1\nu_{21}/(1-\nu_{12}\nu_{21}) & 0 \\ E_2\nu_{12}/(1-\nu_{12}\nu_{21}) & E_2/(1-\nu_{12}\nu_{21}) & 0 \\ 0 & 0 & G_{12} \end{bmatrix} \begin{Bmatrix} \epsilon_1 \\ \epsilon_2 \\ \gamma_{12} \end{Bmatrix} \tag{3.2}$$

The parameter ν_{12} is the principal Poisson's ratio, value that is not limited to to less than 0.5 as in the isotropic material case. For anisotropic structures, the independent variables are four: G_{12}, E_1, E_2 and ν_{12}, since the stiffness matrix is symmetric. Hence, to evaluate ν_{21} we consider the relation: $E_1/\nu_{12} = E_2/\nu_{21}$. The relations can be abbreviated further as:

$$\boldsymbol{\sigma} = \boldsymbol{D}\boldsymbol{\epsilon}$$

where $\boldsymbol{D}$ is the *stiffness matrix*. It is now important to transform the axis relation from $(1, 2)$ to the reference Cartesian coordinate system (x, y), considering that the fiber axis 1-direction is tilted by an arbitrary θ angle with respect to the x-axis. The *transformed stiffness matrix* $\overline{\boldsymbol{D}}$ can be rewritten as:

$$\overline{\boldsymbol{D}} = \boldsymbol{H}^{-1}\boldsymbol{D}\boldsymbol{R}\boldsymbol{H}\boldsymbol{R}^{-1}$$

where $\boldsymbol{H}$ is the *transformation matrix*:

$$\boldsymbol{H} = \begin{bmatrix} c^2 & s^2 & 2sc \\ s^2 & c^2 & -2sc \\ -sc & sc & c^2 - s^2 \end{bmatrix} \tag{3.3}$$

with $c = \cos\theta$ and $s = \sin\theta$, and $\boldsymbol{R}$ is the *Reuter's matrix*:

$$\boldsymbol{R} = \begin{bmatrix} 1 & 0 & 0 \\ 0 & 1 & 0 \\ 0 & 0 & 2 \end{bmatrix} \tag{3.4}$$

We now consider the case of fiber-reforced composite crossplied laminate, in which a sequence of arbitrary orientation ply are stacked together in perfect adhesion regime.

Coordinates x and y are the direction of the plate, and z is defined as the thickness direction and it is customarily taken as positive upward (Fig.3.1). It is then possible to assume that the mid-surface plane can be used to represent three-dimensional plates in two dimensional form under the *Kirchhoff assumption*. Hence, the constitutive relation for strain $\boldsymbol{\epsilon}$ can be written as:

$$\boldsymbol{\epsilon} = \begin{Bmatrix} \epsilon_x \\ \epsilon_y \\ \gamma_{xy} \end{Bmatrix} = \boldsymbol{\epsilon}^0 + \boldsymbol{\kappa} z \tag{3.5}$$

where $\boldsymbol{\epsilon}^0$ (unknown) is the midplane strain ($z = 0$), and $\boldsymbol{\kappa}$ (unknown) is the curvature:

$$\boldsymbol{\kappa} = \begin{Bmatrix} \kappa_x \\ \kappa_y \\ \kappa_{xy} \end{Bmatrix}$$

where the component κ_{xy} is the *twisting curvature*, that defines how the x-direction midplane slope changes with y. It is now possible to describe the stress as:

$$\boldsymbol{\sigma} = \overline{\boldsymbol{D}}\boldsymbol{\epsilon} = \overline{\boldsymbol{D}}\epsilon^0 + \overline{\boldsymbol{D}}\boldsymbol{\kappa} z$$

Each of the layer stresses must add to balance the force per unit width $\boldsymbol{N}$:

$$\boldsymbol{N} = \begin{Bmatrix} N_x \\ N_y \\ N_{xy} \end{Bmatrix} = \int_{-h/2}^{h/2} \boldsymbol{\sigma} dz = \sum_{k=1}^{N} \int_{z_k}^{z_{k+1}} \boldsymbol{\sigma}_k dz$$

where $\boldsymbol{\sigma}_k$ is the stress in the kth layer and z_k is the distance from the laminate midplane to the bottom of the kth layer. Using the same notation, the moment resultants per unit width $\boldsymbol{M}$ must be balanced by the moments contributed by the internal stresses:

$$\boldsymbol{M} = \begin{Bmatrix} M_x \\ M_y \\ M_{xy} \end{Bmatrix} = \int_{-h/2}^{h/2} \boldsymbol{\sigma} z dz = \sum_{k=1}^{N} \int_{z_k}^{z_{k+1}} \boldsymbol{\sigma}_k z dz$$

Removing the quantities from the integral, we obtain:

$$\boldsymbol{N} = \sum_{k=1}^{N} \left(\overline{\boldsymbol{D}}_k \boldsymbol{\epsilon}^0 \int_{z_k}^{z_{k+1}} dz + \overline{\boldsymbol{D}}_k \boldsymbol{\kappa} \int_{z_k}^{z_{k+1}} z dz \right)$$

$$\boldsymbol{M} = \sum_{k=1}^{N} \left(\overline{\boldsymbol{D}}_k \boldsymbol{\epsilon}^0 \int_{z_k}^{z_{k+1}} z dz + \overline{\boldsymbol{D}}_k \boldsymbol{\kappa} \int_{z_k}^{z_{k+1}} z^2 dz \right)$$

Evaluating the integrals, the expression can be written in compact form:

$$\begin{Bmatrix} \boldsymbol{N} \\ \boldsymbol{M} \end{Bmatrix} = \begin{bmatrix} \mathscr{A} & \mathscr{B} \\ \mathscr{B} & \mathscr{C} \end{bmatrix} \begin{Bmatrix} \boldsymbol{\epsilon}^0 \\ \boldsymbol{\kappa} \end{Bmatrix} \tag{3.6}$$

where $\mathscr{A}$ is the *extensional stiffness matrix* defined as:

$$\boxed{\mathscr{A} = \sum_{k=1}^{N} \overline{\boldsymbol{D}}_k \left(z_{k+1} - z_k \right)} \tag{3.7}$$

and $\mathscr{B}$ is the *coupling stiffness matrix* defined as:

$$\boxed{\mathscr{B} = \frac{1}{2} \sum_{k=1}^{N} \overline{\boldsymbol{D}}_k \left(z_{k+1}^2 - z_k^2 \right)} \tag{3.8}$$

and $\mathscr{C}$ is the *bending stiffness matrix* defined as:

$$\boxed{\mathscr{C} = \frac{1}{3} \sum_{k=1}^{N} \overline{\boldsymbol{D}}_k \left(z_{k+1}^3 - z_k^3 \right)} \tag{3.9}$$

The above relations provide a straightforward method of determining displacements and stresses in laminated composites subjected to in-plane forces and/or bending loads.

3.1.1 Hygroscopic and Thermal effects

It is possible to include internal forces in the model, related to the deformation tendencies associated to material properties. For instance, active tissues in Erodium and Pelargonium seeds are dominated by hygroscopic expansion. In general, an increase of relative humidity $\Delta\phi$ causes an hygroscopic strain $\boldsymbol{\epsilon}_H$, that is obtained without needing to apply stress. Supposing that the hygroscopic expansion be linear with respect to the relative humidity variation, the hygroscopic strain is modeled as:

$$\boldsymbol{\epsilon}_H = \boldsymbol{\alpha}\Delta\phi = \boldsymbol{\alpha}\left(\phi - \phi_0\right) \tag{3.10}$$

where $\boldsymbol{\alpha}$ is the linear coefficient of hygroscopic expansion (CHE), ϕ is the relative humidity and ϕ_0 is the value of relative humidity at which the mechanical system shows a curvature $\boldsymbol{\kappa} = 0$. To calibrate the considered model, ϕ_0 must be evaluated experimentally (as a working parameter accounting for, e.g., residual stresses and structural imperfections resulting from fabrication). The CHE is defined according to the fiber direction frame $(1, 2)$, hence we apply the transformation to common (x, y) axes obtaining:

$$\boldsymbol{\alpha} = \begin{Bmatrix} \alpha_x \\ \alpha_y \\ \alpha_{xy} \end{Bmatrix} = \boldsymbol{R}\boldsymbol{H}^{-1}\boldsymbol{R}^{-1} \begin{Bmatrix} \alpha_1 \\ \alpha_2 \\ 0 \end{Bmatrix} \tag{3.11}$$

Note that $\alpha_{12} = 0$ because the hygroscopic expansion causes normal strain only, so shearing components of the strain are unaffected. Knowing that the hygroscopic strain is obtained without needing to apply stress, we can rewrite the stress relation as:

$$\boldsymbol{\sigma} = \overline{\boldsymbol{D}}\left(\boldsymbol{\epsilon} - \boldsymbol{\epsilon}_H\right)$$

Balancing the stressed against the applied forces and moments as before, we obtain:

$$\boldsymbol{N} = \int \boldsymbol{\sigma} dz = \mathscr{A}\boldsymbol{\epsilon}^0 + \mathscr{B}\boldsymbol{\kappa} - \int \overline{\boldsymbol{D}}\boldsymbol{\alpha}\Delta\phi dz$$

$$\boldsymbol{M} = \int \boldsymbol{\sigma} z dz = \mathscr{B}\boldsymbol{\epsilon}^0 + \mathscr{C}\boldsymbol{\kappa} - \int \overline{\boldsymbol{D}}\boldsymbol{\alpha}\Delta\phi z dz$$

It is possible then to rearrange the "hygroscopic loads" as:

$$\boxed{\boldsymbol{N}_H = \sum_{k=1}^{N} \overline{\boldsymbol{D}}_k \boldsymbol{\alpha}_k \left(z_{k+1} - z_k\right)} \tag{3.12}$$

$$\boxed{\boldsymbol{M}_H = \frac{1}{2}\sum_{k=1}^{N} \overline{\boldsymbol{D}}_k \boldsymbol{\alpha}_k \left(z_{k+1}^2 - z_k^2\right)} \tag{3.13}$$

To determine kinematics in the case of passive actuators, we suppose that no external loads will cause the deformation of the laminate composite (e.g. $\boldsymbol{N} = 0$ and $\boldsymbol{M} = 0$). The unknown variables of our problem are the curvature and strain tensors, hence it is possible to solve the matrix relation as:

$$\begin{Bmatrix} \boldsymbol{\epsilon}^0 \\ \boldsymbol{\kappa} \end{Bmatrix} = \begin{bmatrix} \mathscr{A} & \mathscr{B} \\ \mathscr{B} & \mathscr{C} \end{bmatrix}^{-1} \begin{Bmatrix} \boldsymbol{N}_H \\ \boldsymbol{M}_H \end{Bmatrix} \tag{3.14}$$

From an experimental point of view, the analytical solution of the system can be obtained by measurement or micromechanical estimation of the four

independent anisotropic material parameters (e.g. E_1, E_2, ν_{12} and G_{12}) for each material type stacking in sequence, the evaluation of the linear expansion coefficients (e.g CHE) and the working parameter that accounts the residual stresses in the structure (e.g ϕ_0).
The same treatment can be extended to thermal expansion effects, in which an increase of temperature ΔT causes a thermal expansion:

$$\boldsymbol{\epsilon}_T = \boldsymbol{\beta}\Delta T \tag{3.15}$$

where ϵ_T is the thermally-induced strain and β is the coefficient of linear thermal expansion (CTE). Similarly to the hygroscopic case, it is possible to rearrange the "thermal loads" as:

$$\boldsymbol{N}_T = \sum_{k=1}^{N} \overline{\boldsymbol{D}}_k \boldsymbol{\beta}_k \left(z_{k+1} - z_k\right) \tag{3.16}$$

$$\boldsymbol{M}_T = \frac{1}{2} \sum_{k=1}^{N} \overline{\boldsymbol{D}}_k \boldsymbol{\beta}_k \left(z_{k+1}^2 - z_k^2\right) \tag{3.17}$$

The complete set of relations between applied forces and moments, and the resulting midplane strains and curvatures, can be summarized as a single matrix equation:

$$\begin{Bmatrix} \overline{\boldsymbol{N}} \\ \overline{\boldsymbol{M}} \end{Bmatrix} = \begin{bmatrix} \mathscr{A} & \mathscr{B} \\ \mathscr{B} & \mathscr{C} \end{bmatrix} \begin{Bmatrix} \boldsymbol{\epsilon}^0 \\ \boldsymbol{\kappa} \end{Bmatrix} \tag{3.18}$$

where $\overline{\boldsymbol{N}} = \boldsymbol{N} + \boldsymbol{N}_H + \boldsymbol{N}_T$ and $\overline{\boldsymbol{M}} = \boldsymbol{M} + \boldsymbol{M}_H + \boldsymbol{M}_T$.

3.1.2 Mid-curve reconstruction in coiled strips

To reconstruct the helix shape of the strip, we have to determine the principal curvature κ_0. From the laminate composite plates model, we can express the curvature tensor $\overline{\boldsymbol{b}}$ as:

$$\overline{\boldsymbol{b}} = \begin{bmatrix} \kappa_x & \kappa_{xy} \\ \kappa_{xy} & \kappa_y \end{bmatrix}$$

The reference curvature tensor $\overline{\boldsymbol{b}}^*$ is obtained evaluating the eigenvalues $\lambda(\kappa_1, \kappa_2)$ of the curvature tensor [40], such that:

$$\overline{\boldsymbol{b}}^* = \begin{bmatrix} \kappa_1 & 0 \\ 0 & \kappa_2 \end{bmatrix}$$

The principal curvature is represented by the maximum eigenvalue associated to the reference curvature tensor [40]: $\kappa_0 = \max(\kappa_1, \kappa_2)$.

To reconstruct the mid-curve, we have to relate the curvature and strain derived from the laminate composite plate model to the macroscopic geometrical features of the helical strip, i.e. the radius and the pitch. Considering a strip of length l and width w, the dimensionless elastic energy of a non-Euclidean shell is dominated by the superposition of stretching and bending effects [41]. The transition from bending to stretching dominated regime is related to a dimensionless figure of merit $\tilde{w}$, which is defined as [41]:

$$\tilde{w} = w\sqrt{\frac{\kappa_0}{h}} \tag{3.19}$$

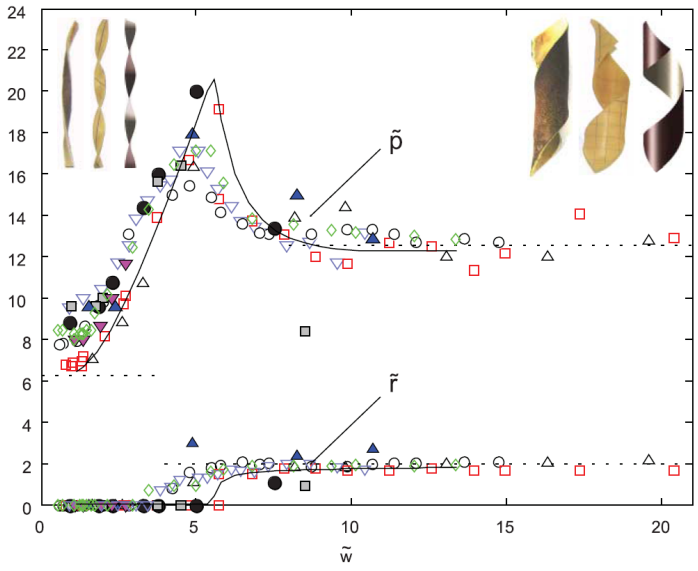

Figure 3.2: Transition from bending to streching dominated regime in latex sheets. Dimensionless radius, $\tilde{r} = r\kappa_0$, and pitch, $\tilde{p} = p\kappa_0$, versus dimensionless width, $\tilde{w}$, for various strips cut from latex sheets at $\Psi = \pi/4$ [41].

In particular, if $\tilde{w} >> 1$ the strip is in stretching dominated regime (wide strips). We recall that the longitudinal axis of hygroscopic fibers forms an angle Ψ with respect to the x-axis. Consequently, we can relate the normal curvature κ and the geodesic torsion τ to the principal curvature κ_0 and the tilt angle Ψ, using the Euler's formula: $\kappa = \kappa_0 \cos^2 \Psi$ and $\tau = \kappa_0 \cos \Psi \sin \Psi$. In this case, the radius and pitch of the helix assume the form [41]:

$$\text{Radius} = \frac{\kappa}{\kappa^2 + \tau^2} = \frac{1}{\kappa_0} \qquad \text{Pitch} = \frac{2\pi\tau}{\kappa^2 + \tau^2} = \frac{2\pi}{\kappa_0} \tan \Psi \tag{3.20}$$

Instead, if $\tilde{w} \leq 1$ the strip is in a bending dominated regime (narrow strip). This implies that radius and pitch can be derived considering that [41]:

$$\text{Radius} = \frac{1}{\kappa_0} \cos 2\Psi \qquad \text{Pitch} = \frac{2\pi}{\kappa_0} \sin 2\Psi \tag{3.21}$$

In an intermediate width regime, it is not possible to have an explicit formulation for the mid curve reconstructions, since the mathematical procedure consists in minimizing the energy with respect to the metric functions [41].

3.2 Static prediction: helical cylindrical spring theory

To evaluate the force and the moment generated by the actuator, we consider the theory of mechanical springs subjected to large deformations. Modelling the structure as a homogeneous helical cylindrical spring with rectangular cross-section, it is possible to calculate the extensional force F_E and the moment M_0 in closed form.

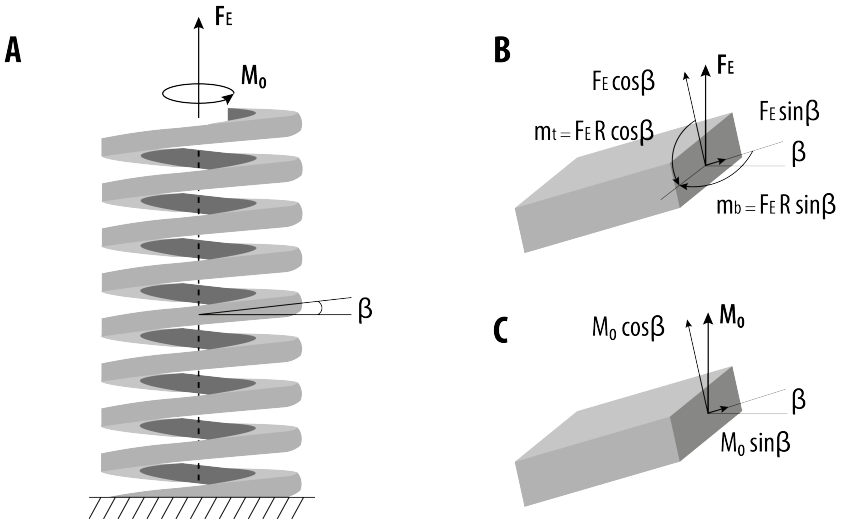

Figure 3.3: Sketch of extensional force and torque acting on an helical cylindrical spring with rectangular cross section. A) Example of spring with ends fixed against rotation. B) Bending and twisting moment acting on the spring due to extensional force. C) Bending and twisting moment acting on the spring due to torque.

It is shown from the theory of elasticity that the change in a bar or wire curvature as the spring deflects from an initial pitch angle β_0 to a different pitch angle β is:

$$\Delta\kappa = \frac{\cos^2\beta}{R} - \frac{\cos^2\beta_0}{R_0}$$

$$\Delta\theta = \frac{\sin\beta\cos\beta}{R} - \frac{\sin\beta_0\cos\beta_0}{R_0}$$

where $\Delta\kappa$ is the change in curvature of the wire, $\Delta\theta$ is the angle twist per unit length, R the radius of the cylinder and R_0 the initial radius.
The pitch angle β is defined from geometrical consideration as:

$$\beta = \arctan\left(\frac{P}{4R}\right)$$

The moment M_0 and the extensional force F_E are acting on the spring simultaneously, so the bending and the the twisting moment m_b and m_t acting on the wire will be:

$$m_b = M_0\cos\beta - F_E R\sin\beta$$

$$m_t = M_0\sin\beta + F_E R\cos\beta$$

The change in curvature of the wire due to the bending moment is equal to the moment divided by the flexural rigidity EI, where E is the Young's modulus and I is the moment of inertia of rectangular cross section:

$$\Delta\kappa = \frac{m_b}{EI} \quad I = \frac{1}{12}wh^3$$

where w is the width and h the thickness. Moreover, the change in twist angle per unit length due to twisting moment is equal to moment divided torsional

rigidity J of rectangular cross section:

$$\Delta\theta = \frac{m_t}{GJ} \quad J = k_s w h^3$$

where G is the shear modulus, k_s the shape factor:

$$k_s = \frac{1}{3}\left[1 - \frac{192h}{\pi^5 w}\sum_{n=1}^{\infty}\frac{1}{(2n-1)^5}\tanh\frac{(2n-1)\pi w}{2h}\right] \simeq \frac{1}{3} + 0.21\frac{h}{w} + 0.0175\left(\frac{h}{w}\right)^5$$

Combining together the previous equations, we obtain the analytical solution for the extensional force and moment for an helical cylindrical spring:

$$F_E = \frac{1}{R}\left[Gk_s w h^3 \cos\beta\left(\frac{\cos\beta\sin\beta}{R} - \frac{\cos\beta_0\sin\beta_0}{R_0}\right) + \right.$$
$$\left. - \frac{1}{12}Ewh^3\sin\beta\left(\frac{\cos^2\beta}{R} - \frac{\cos^2\beta_0}{R_0}\right)\right] \quad (3.22)$$

$$M_0 = Gk_s w h^3 \sin\beta\left(\frac{\cos\beta\sin\beta}{R} - \frac{\cos\beta_0\sin\beta_0}{R_0}\right) +$$
$$+ \frac{1}{12}Ewh^3\cos\beta\left(\frac{\cos^2\beta}{R} - \frac{\cos^2\beta_0}{R_0}\right) \quad (3.23)$$

Note that the geometrical changes in radius as function of relative humidity can be predicted using the laminate composite plates model described above. In the case of bilayer actuators, we assume that the composite structure can be simplified as a homogeneous material by means of rule of mixtures, where the properties of the composite are evaluated considering the volume fraction f of the fiber active layer with respect to the substrate passive layer. Since the surface of the passive and active layer are equal by definition, we obtain:

$$f = \frac{h_a}{h_a + h_p} = \frac{h_a}{h}$$

$$E = E_a f + (1-f)E_p \qquad \nu = \nu_a f + (1-f)\nu_p \qquad G = \frac{E}{2(1+\nu)} \quad (3.24)$$

where ν is the approximated Poisson's ratio, a and p subscript represents the physical and geometrical properties of the active and passive layers.

3.3 Water adsorption in hygroscopic tissues: the Diffusion equation

Water permeation in hygroscopic tissues is modeled considering one dimensional Fickian diffusion along the thickness axis (z-axis), where a constant concentration source ϕ_0 is located at the top of the surface (z = 0) [29, 40].

$$\frac{\partial \phi}{\partial t} = D \frac{\partial^2 \phi}{\partial z^2}$$

where $\phi = \phi(t, z)$ describe the RH level in the domain of the active layer $z \in [0, h]$ (z is the coordinate describing the thickness of the active layer) and the time $t \in [0, \infty)$, while D is the moisture diffusivity. The boundary conditions for the diffusion equations are:

$$\phi(0, t) = \phi_\infty; \quad \phi(z, 0) = \phi_0; \quad \left.\frac{\partial \phi}{\partial z}\right|_{z=h} = 0$$

where ϕ_∞ is the RH level at the interface of the active layer wit the air (constant concentration source), ϕ_0 is the initial RH level in the active layer (constant), and the last boundary condition is used to describe the impossibility of the movement of water molecules through the active and inactive interface. The obtained solution $\phi(z, t)$ is:

$$\phi(z, t) = \sum_{k=0}^{\infty} \left[\frac{2(\phi_0 - \phi_\infty)}{(k + 1/2)\pi} \sin \frac{(k + 1/2)\pi z}{h} \exp -t/\tau_k \right] + \phi_\infty \tag{3.25}$$

where the diffusion time τ_k is:

$$\frac{1}{\tau_k} = D \left[\frac{(k + 1/2)\pi}{h} \right]^2 \tag{3.26}$$

Since the diffusion coefficient can be evaluated experimentally, it is possible to describe the kinetics of the actuator with the time variation of relative humidity in the hygroscopic layer.

3.4 An example: *Pelargonium appendiculatum* seed

To explain the overall awn deformation in *Pelargonium appendiculatum* seeds, we conceptually decompose the cap layer into two identical and homogeneous sublayers, which differ only in the fiber orientation. The helical windings of cellulose microfibrils will determine two microfibril angles (MFA), θ_1 and θ_2. The deformation of each active layer is anisotropic as confined by the microfibril angles. Then, the awn can be simply modeled as a trilayer structure having two active layers and one inactive layer.

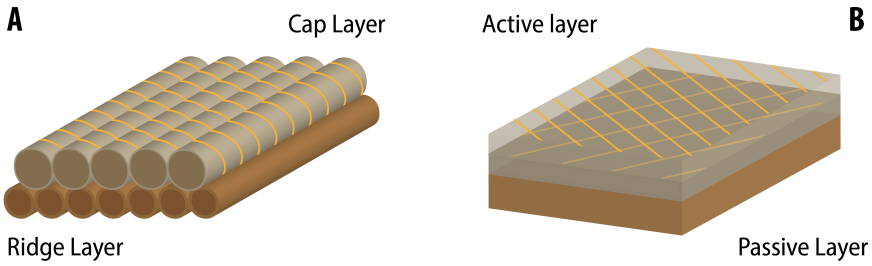

Figure 3.4: Trilayer decomposition of the *Pelargonium appendiculatum* seed's awn. A) Representation of the cap and ridge layer. B) Trilayer decomposition of the awn.

Considering that the overall thickness of the awn (0.07 mm) relative to their length (18 mm) and width (0.43 mm), it is possible employ a theory of laminated composite plates to evaluate stresses and curvature of the trilayer strip. To reconstruct the mid-plane, i.e. evaluate the radius and the pitch of the coiled awn as function of RH, we assume that each active layer will determine the same hygroscopic stress on the structure, since we assumed identical active sublayers (same geometrical and material properties). By doing so, the effective tilt angle Ψ can be defined as the mean value of the two microfibril angles:

$$\Psi = \frac{\theta_1 + \theta_2}{2}$$

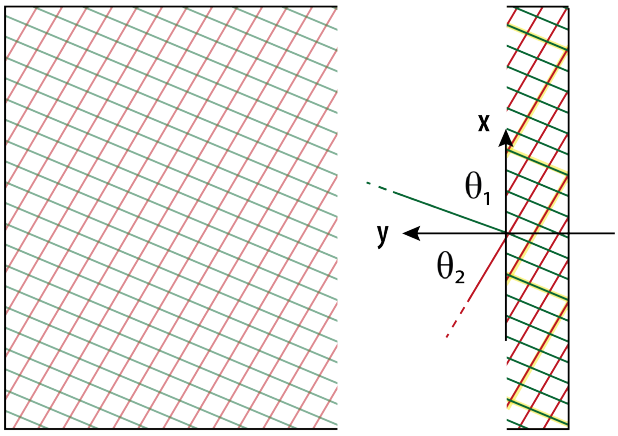

Figure 3.5: Schematic of the angle representation in the trilayer decomposition.

To implement the algorithm, we have then to follow three different steps:

- At first, we have to characterize the kinematic behaviour of the hygroscopic strip (e.g. the awn of the seed), so how the pitch and the radius changes as function of the relative humidity. This permits to evaluate the mismatch strain $\alpha\phi_0$, which takes into account all the residual stresses and structural

imperfection resulting from the fabrication (e.g. biological growth of the seed).

- Hereafter, we describe the material properties of each layer and their relative geometrical parameters which are used for the laminate composite plate model. Its important to note that according to the available parameters on the material characterization, we have to assume isotropic or anisotropic linear elasticity. For sake of simplicity, we described the Pelargonium seed's awn with isotropic stiffness matrix, and considering also that cellulose microfibril will hygroscopically expand in the transverse direction with respect to the principal material direction. In the last part of this step, it is fundamental to consider the energy regime of the structure. Since Pelargonium shows $\tilde{w} \simeq 1$, we consider the structure in bending dominated regime, and so radius and pitch are evaluated from the principal curvature considering Eq.3.21.

- If the modeling results match the kinematic characterization, we can finally proceed to the prediction of the static extensional force and the relative moment, using spring theory.

Table 3.1: *Pelargonium appendiculatum* seed's awn modeling parameters and results.

	Ridge Layer	**Cap Layer**
Geometrical parameters		
Length [mm]	18.54±3.1	
Width [μm]	428±38	
Thickness [μm]	59.66±9.82	39.77±6.86
MFA [deg]	/	(1) 55 (2) -85
Material properties		
Young's Modulus [GPa]	1.478±0.249	0.780±0.286
Poisson's coefficient [a.u.]	0.33	0.33
CHE [a.u.]	0.06±0.02	0.20±0.04
Dynamic parameters		
Weigth [mg]	5.2±0.2	
Diffusivity [m^2/s]	2.34±0.70 $\times 10^{-11}$	
Max Force [mN]	5.06±1.06	
Model Force [mN]	5.65	
Max Torque [μN m]	20.66±2.51	
Model Torque [μN m]	57.70	

3.4.1 Matlab implementation

Get experimental data, physical and geometrical parameters

```
%% Pelargonium appendiculatum
% Experimental data
x_conc          = [30 40 50 60 70 80 90] / 100;                                 %[%]
x_Dconc         = [2.5 2.5 2.5 2.5 2.5 2.5 2.5] / 100 ;                         %[%]

x_radius        = [0.15467 0.15 0.18333 0.21667 0.24667 0.25333 0.3]*1e-3;      %[m]
x_dradius       = [0.00503 0.01 0.02082 0.01528 0.01528 0.02082 0.01]*1e-3;     %[m]
x_pitch         = [0.57 0.61767 0.634 0.79767 0.82667 0.92667 1.14667]*1e-3;    %[m]
x_dpitch        = [0.011 0.01266 0.07529 0.0676 0.02517 0.08021 0.05508]*1e-3;  %[m]

% params for model
N = 101;
conc            = linspace(0.3,0.9,N);       %[%]

%% Get calibration points from experiments
[RH0, slope, p1, p2]    = x_calibration(x_conc, x_radius, in.psi);
x_curvature             = p1 * conc + p2;

%% parameters
% Processing parameters
in.N_layer      = 3;                % Number of layers
in.phi_0        = RH0;              % Mismatch strain eps = alpha*(phi_0 - conc)

% Material properties [Ridge Layer - Cap Layer]
in.E            = [1.478*1e9 0.78*1e9 0.78*1e9];      % Young's Modulus, Pa
in.ni           = [0.33 0.33 0.33];                   % Poisson's coefficient, a.u.
in.alpha        = [0.08 0.24 0.24];                   % CHE, -
in.D            = 2.84e-11;                           % Diffusion time, m^2 s^-1

% Geometrical parameters
in.theta        = [0 -85 55]*pi/180;                  % Microfibril Angles (MFA), rad
in.psi          = 0.5*(in.theta(3)+in.theta(2));      % Tilt angle, rad
in.hp           = 59.66*1e-6;                         % Passive Layer thickness, m
in.ha           = 39.77*1e-6/2;                       % Active Layer half thickness, m
in.l            = 18.54*1e-2;                         % Length, m
in.w            = 428*1e-6;                           % Width, m

%% go
% Laminate composite model
[r, p]                  = LCM_kinematics(in,conc);
[F_E,M0]                = LCM_static(in,conc);
```

Evaluation of the mismatch strain from experimental data

```
function [RH0, slope, p1, p2] = x_calibration(RH, R, psi)
rho     = cos(2*psi)./R;
[p,S]   = polyfit(RH,rho,1);

% return
RH0  = -p(2)/p(1);
slope  = p(1);
end
```

Laminate composite plates algorithm

```
function [r, p] = LCM_kinematics(in, conc)
%% parameters
N_layer         = in.N_layer;           % Number of layers
% Processing parameters
phi_0           = in.phi_0;             % Mismatch strain, a.u.
% Material properties
E               = in.E;                 % Young's modulus, Pa
ni              = in.ni;                % Poisson's ratio, a.u.
% Geometrical parameters
theta           = in.theta;             % MFA, rad
psi             = in.psi:               % Tilt angle, rad
hp              = in.hp ;               % Passive layer thickness, m
ha              = in.ha ;               % Half of active layer thickness, m
% Hygroscopic expansion coefficeint
alpha_1     = [0    0    0];            % Longitudinal axis
alpha_2     = in.alpha;                 % Transversal axis
alpha_12    = [0    0    0];            % Shear plane

%% Laminated composite model
%% initialization
Samples     = length(conc);
r           = zeros(1,Samples);         % Radius, m
p           = zeros(1,Samples);         % Pitch, m

%% Algorithm
h1 = [0 hp ha ha];
h  = cumsum(h1);                        % Thickness vector, m
h = h - 0.5*h(end);                     % Define the midplane: Kirchoff assumption

% Reuter's Matrix
R = [1 0 0;
     0 1 0;
     0 0 2];

for j = 1:Samples
    % Variation of Relative Humidity
    phi = phi_0 - conc(j);

    % Init Matrices
    N = zeros(3,1);
```

```
    M = zeros(3,1);
    A = zeros(3,1);
    B = zeros(3,1);
    C = zeros(3,1);

    for i = 1:N_layer

        % Transformation Matrix
        cc = cos(theta(i));
        ss = sin(theta(i));

        H = [ cc^2, ss^2, 2*ss*cc; ...
              ss^2, cc^2, -2*ss*cc; ...
             -ss*cc ss*cc cc^2-ss^2];

        % Stiffness Matrix in isotropic assumption
        D = E(i)/(1-ni(i)^2)* ...
            [1 ni(i) 0; ni(i) 1 0; 0 0 (1-ni(i))/2];

        D = H^(-1)*D*R*H*R^(-1);

        % Coefficient of Hygroscopic Expansion (CHE) Vector
        alpha = [alpha_1(i); alpha_2(i); alpha_12(i)];
        alpha = R*H^(-1)*R^(-1)*alpha;

        % Forces
        N = N + D*alpha*phi*(h(i+1)-h(i));
        % Moments
        M = M + 1/2*D*alpha*phi*(h(i+1)^2-h(i)^2);
        % Extensional Stiffness
        A = A + D*(h(i+1)-h(i));
        % Coupling Stiffness
        B = B + 1/2*D*(h(i+1)^2-h(i)^2);
        % Bending Stiffness
        C = C + 1/3*D*(h(i+1)^3-h(i)^3);

    end

    % Inverse Laminate Stiffness Matrix
    LSM = [A B; B C];
    NM  = [N; M];
    eps0_k = LSM\NM;
    % Reference curvature tensor
    b =  [eps0_k(4) eps0_k(6); ...
          eps0_k(6) eps0_k(5)];
    % Principal curvature
    k0 = max(eig(b));
    % Radius
    r(j) = cos(2*psi)/k0;
    % Pitch
    p(j) = 2*pi*sin(2*psi)/k0;
    end % for j
end % of fcn
```

Evaluation of static force and moment

```
function [Force, Moment] = LCM_static(in, conc)
    [r, p]      = LCM_kinematics(in, conc);

    % Upper bound - Mixture Rule
    w           = in.w;
    h           = in.hp + in.ha*2;                      % Whole thickness, m
    f           = in.ha*2/h;                            % Fiber layer fraction, a.u.
    E           = f*in.E(2) + (1-f)*in.E(1);            % Young's Modulus, Pa
    ni          = f*in.ni(2) + (1-f)*in.ni(1);          % Poisson's coefficient, a.u.
    G           = 0.5*E/(1 + ni);                       % Shear modulus, Pa

    % Define coil angle beta
    beta        = atan(p./(4*r));
    % Define shape factor for rectangular cross section
    ks          = (1/3 - 0.21*h/w + 0.0175*h^5/w^5);

    % Extensional Force
    Force       = -(G * ks * w * h^3 * cos(beta)./r .* (sin(beta).*cos(beta)./r - sin
    (beta(1))*cos(beta(1))/r(1)) - 1/12 * E * w * h^3 * sin(beta)./r .* (cos(beta)
    .^2./r - cos(beta(1))^2/r(1)));

    % Moment
    Moment      = -(G * ks * w * h^3 * sin(beta) .* (sin(beta).*cos(beta)./r - sin(
    beta(1))*cos(beta(1))/r(1)) + 1/12 * E * w * h^3 * cos(beta) .* (cos(beta).^2./r
    - cos(beta(1))^2/r(1)));

end
```

Diffusion equation

```
function phi = diffusion_1D(in, conc, time)
    % Dummy variables
    inf         = 1e3;
    k           = linspace(0,inf-1,inf);
    T           = length(time);
    phi         = zeros(1, T);

    % Define paramters
    D           = in.D;                     % Diffusion constant, m^2 s^-1
    z           = 2*in.ha;                  % Thickness cartesian coordinate, m
    h           = 2*in.ha;                  % Thickness active layer, m
    conc_0      = in.conc_0;                % Initial RH concentration, %

    % Analytical solution of 1D diffusion equation
    tau_k = (D.*((k + 0.5)*pi/(2*in.ha)).^2).^(-1);
    for t = 1:T
        phi(t) =  sum( 2*(conc_0 - conc(t)) ./ ((k + 0.5)*pi) .* ...
                  sin( (k + 0.5)*pi*z/h ) .*  exp(-time(t) ./ tau_k) ) + conc(t);
    end
end
```

Sustainable seed-inspired soft actuators and sensors

4

4.1 4D Printing of Humidity-Driven Seed Inspired Soft Robots

Geraniaceae seeds represent a role model in soft robotics thanks to their ability to move autonomously across and into the soil driven by humidity changes. The secret behind their mobility and adaptivity is embodied in the hierarchical structures and anatomical features of the biological hygroscopic tissues, geometrically designed to be selectively responsive to environmental humidity. Considering the Geraniaceae seed family, Pelargonium genus represent a perfect candidate for bioinspiration, due to its pure bilayer structure. We first investigated the kinematic and static performances of *Pelargonium appendiculatum* (L.f.) Willd seeds to develop and validate a model for the design of a biomimetic soft robot.

According with the natural study, we proceed to manufacture a soft miniaturized artificial seed. The robotic structure autonomously explores soil and penetrates inside fractures, extracting energy from the environmental humidity changes. The development of such autonomous soft robots required the use of advanced technology for the fabrication. Considering emerging additive manufacturing techniques, four-dimensional (4D) printing permits to replicate natural physio-mechanical variations over time [50, 51]. 4D printed structures have the unique ability to create dynamic morphological changes under environmental stimuli (i.e. humidity), generating environmental propulsion. According to the material design, structures can be programmed to re-shape and to perform work, adapting its morphology to the selected scenario.

We used 4D printing techniques with biodegradable polymers for the realization of the artificial seed, including Fused Deposition Modeling (FDM) of polycaprolactone (PCL, hygroscopic inactive material), [52] coupled with coaxial electrospinning of hygroscopically active fibers, composed by a polyethylene oxide (PEO) shell [53] and a cellulose nanocrystals (CNC) core. [54] The artificial and natural seeds have comparable geometrical dimensions and biomechanical performances. In the natural seed, the measured torque and extensional force were 20.7 ± 2.5 μNm and 5.1 ± 1.1 mN, respectively, while in the artificial one 30.4 ± 5.1 μNm and 2.4 ± 0.6 mN, respectively. Moreover, the purposively developed theoretical model predicts, within the confidence interval, the kinematics, and statics of the seeds, making it a tool to design a new class of soft robots that explore topsoil by adapting their morphology according to soil composition, roughness, and stiffness.

Compared with the State-of-Art [28–30], we developed for the first time a complete biodegradable soft robot, coupling together two fabrication techniques (FDM and electrospinning), that allow for a wide range of possibilities in the fabrication of hygroscopic actuators, with arbitrary shapes and high performance. Moreover, we developed a bioinspired protocol to characterize and highlight the morphological and mechanical features for the realization of seed-like soft robots. Finally, we generalized a description of the material and structural features necessary to completely describe an hygroscopic actuator.

4.1.1 Materials and Methods

Biological investigation: *Pelargonium appendiculatum* (L.f.) Willd seeds were purchased from Greenmarket di Barbone Valerio, Bergamo Italy. Morphometric analysis of the awns was carried out using a digital caliper (RS PRO 150mm Digital Caliper 0.0005 in, 0.01 mm, Metric and Imperial, UK) with a resolution of ± 0.01 mm and a digital microscope (KH-8700, Hirox, Japan). The seed mass was measured with an analytical balance (KERN ABS-N, Germany) with a resolution of ± 0.0001 g. Pelargonium awns were separated between active and inactive hygromorphic regions and cut into 5 mm sections. Samples were softened with 4% ethylenediamine for 3-4 days, dehydrated and embedded in paraffin [55] and cut into 10 μm sections with a manual microtome (Leica SM2010R). In the fluorescence analysis, the sections were stained with Fluorescent brightener 28 for cellulose identification, whereas lignin autofluorescence was visible with the blue light excitation (488nm). Cellulose detection was also achieved with the Alcian blue histochemical stain. Images were captured with Nikon Eclipse Ni-U optical and fluorescence microscope.

Pitch and Radius measurements: A climatic test chamber (CTC256, Memmert GmbH) was used to investigate the humidity-responsive deformation of samples in a spatially homogeneous humid air environment. Samples were subjected to humidity ramp at controlled temperature (30 °C) from 30% RH to 90% RH with 10% RH gap, while simultaneously video recording the variation of radius and pitch (Logitech Brio Stream, Logitech). To ensure a complete moisture diffusion in hygroscopic active layer, each humidity value was fixed for 5 minutes. The RH inside the chamber was monitored using standard precalibrated humidity meter. To evaluate the variation of geometrical parameters, all the video-data are post-processed using ImageJ software.

Extensional Force and Torque measurements: Natural and artificial samples are tested in controlled temperature and humidity environment (T=20°C and RH = 40%), measuring the force through a load cell (Futek LSB200, Futek Advanced Sensor Technology Inc.) and abruptly increasing the local humidity using a water aerosol. To reduce mechanical vibrations, the load cell was fixed on an optical bench suspended on passive isolator. A commercial humidity and temperature sensor (Sensirion SHT21) was used to monitor constantly the sample in analysis.

Diffusion Constant measurement: Hygroscopic structures have been subjected to a humidity stepwise function from RH = 30% to RH = 90%, flowing locally a water aerosol, and monitoring the variation of geometry using a camera (Logitech Brio Stream, Logitech). With the kinematic and morphological analysis, it was possible to determine diffusion time and consequently the diffusion constant.

Substrate Fabrication: The PCL (Number average molar mass 45,000 g/mol, Sigma Aldrich) substrate was produced through fusion deposition modeling (3DBioplotter, EnvisionTEC), keeping the temperature of hot-melt extruder at 150°C, stabilizing the melt polymer for 10 min and using cylindrical nozzle (3mm length and 0.2mm internal diameter). The PCL was printed on aluminum foil cleaned in ethanol, then fixed on printing plate at a temperature of 40°C. To optimize printing condition, the extrusion pressure was set at 6 bar, the printing speed at 11 mm/s. Nozzle offset was set to 100μm for beam samples and to 75μm for artificial seed samples. Printing direction is fixed at 70° with distance between strands of 0.20mm.

Surface Activation: To guarantee adhesion with aqueous-based fibers, an air plasma treatment (Tucano, Gambetti Kenologia Srl) was applied on the 3D printed substrate. The plasma time was set to 30s, gas stability time to 15s, power setpoint to 150W, gas setpoint 30 sccm (cm^3/min) and base vacuum to 0.50 mbar. To evaluate the effectiveness of the process, a contact angle measurement was done with an optical tensiometer (Theta OneAttension, Biolin Scientific).

Nanofiber deposition: The fiber deposition was carried out by electrospinning technique. The electrospinning apparatus (Linari RT Advanced, Linari Engineering srl) consists in a syringe pump, a coaxial needle (internal diameter 1.2 mm, external diameter 1.8 mm), a rotary drum collector (10cm diameter) and a high voltage supply. The distance between the end of the coaxial tip and the sample substrate is set to 5 cm, while the collector rotates at 2500 rpm (tangent velocity on collector surface 13.08 m/s). The syringe's vertical speed is set to 1 cm/s and the voltage applied to the polymer drop is 20kV (electric field mean modulus 4 kV/cm). All the processes were carried out at RH=20% and T=20°C, with a number of round-trip cycles (RTC) equal to 250 (6h:30min). Fiber orientation and diameter analysis were evaluated using ImageJ software [56]. The solution used for the realization of the core fiber is composed by CNC 5% (Nanografi Nanotechnology AS), dispersed in ultrapure water (Millipore Milli-Q gradient A10, resistivity >18 $M\Omega cm^{\tilde{}1}$) under continuous stirring (500rpm) at room temperature for 24h. The shell component is a 10 wt% aqueous solution of PEO, (viscosity-average molecular weight 300,000 g/mol, Sigma Aldrich) and 10 vol% of ethanol (96% of concentration, Sigma Aldrich), dispersed under continuous stirring (100 rpm) at T = 80°C for 4h. The solutions were preserved under chemical hood in continuous stirring, at most for one week.

Elastic Modulus measurement: Cap and ridge layer Young's modulus were measured using nanoindentation technique (INano, Nanomechanics Inc.). Natural samples were investigated applying Oliver-Pharr method, [57] using Berkovitch tip (Young's modulus E = 1141 GPa, Poisson's ratio $\nu = 0.07$) and applying a target triangular function load of 5 mN, target depth 300 nm, with an indentation strain rate of 0.2 %/s. For artificial samples, dynamic nanoindentation [58] was done due to the viscoelastic nature of polymers involved. A cylindrical flat tip was used, with a punch diameter of 105μm. The surface approach distance was fixed at 15μm, with surface approach velocity of 500 nm/s, applying 100 nm of pre-test compression. During the measurement the temperature was kept at constant humidity RH = 50% and temperature T = 25°C. Moreover, we investigate the variation of Young's Modulus of the hygroscopic material in relation to RH using a tensile test.

Morphology of artificial structures: Thickness measurements of 3D printed PCL and electrospun fiber layer were performed using an optical profilometer (Leica DCM3D, Leica Microsystems, Italy). The fiber layer thickness was evaluated after a localized deposition on flat aluminum substrate, then gently scratched and finally cut using razor blade. SEM images (Zeiss EVO LS10, Germany) were obtained with 10kV accelerating voltage, after gold sputtering. Optical microscopy was done by Hirox KA 8700 (Japan) digital microscope.

Statistical Analysis: The normality of data distribution was tested with the Shapiro–Wilk test; normally-distributed data were analyzed with ANOVA followed by LSD post hoc with Bonferroni correction and expressed as average ± standard error. Non-normally distributed data were analyzed with the Kruskal–Wallis test followed by pairwise Wilcox post hoc test with Holm correction and expressed as median ± 95% confidence interval. Each experiment has been performed in triplicate (n = 3), if not differently indicated.

4.1.2 Biomechanical analysis of *Pelargonium appendiculatum* for soft robot design

To properly describe the kinematic and static behaviour of *Pelargonium appendicultum*'s awn, we first define a procedure to characterize geometrically and mechanically the structure. The first step is to highlight the morphometry of the seed, to observe the macroscopic geometrical features of the structure, as well as the effective mechanical role of the bilayer through hystological analyisis and nanoindentation of the ridge and cap layer.

In Figure 4.2, a detailed morphometric analysis is provided (n = 10). The hystological analysis permits to observe the bilayer nature of the awn. Transverse sections show that string-like shape composed of lignin-rich sclerenchyma cells and a layer of larger cells aligned in parallel with each other. The ridge layer is mainly composed by lignin-based sclerenchyma cells, which enacts the role of a hydrophobic passive substrate. Instead, the cap layer presents an higher contribution of cellulose, stained with alcian blue, that makes it the effective hygroscopic active layer Figure 4.1.

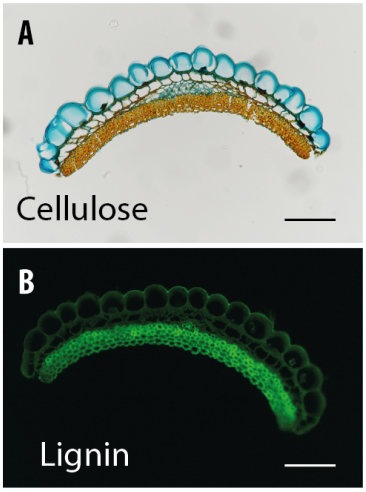

Figure 4.1: Hystological analysis of Pelragonium's awn transverse section. A) Transverse section of the awn with cellulose stained with Alcian blue. Scalebar 100μm. B) Fluorescent image of a transverse section of the awn with lignin auto-fluorescence, excitation at 488nm. Scalebar 100μm.

Relative thicknesses evaluated through SEM, bright and dark field microscopy of the section, show that the thickness of the cap and ridge layer are respectively h_{Cap}= 39.8 ± 6.9 μm and h_{Ridge}= 59.7 ± 9.8 μm (n = 6). Due to its compositional and morphological nature, the awn in P. appendiculatum can be split into an effective bilayer, which makes it more suitable for the design and bioinspiration of an artificial equivalent seed based on bilayered hygroscopic theory and structure [28].

The cap and ridge layer stiffness were analyzed separately, due to different morphological and compositional structures. Considering the small volumes of material involved, Young's modulus cap and ridge layer are characterized by the nanoindentation technique at fixed humidity and temperature (RH = 50%, T = 25°C): E_{Cap}= 0.78 ± 0.29 GPa and E_{Ridge}= 1.48± 0.25 GPa (n = 5). From a biomechanical point of view, the dried tissue in Pelargonium mediates the hygroscopic movement and is composed of a combination of lignin and hemicellulose, as in the pinecone. So, the linear coefficient of hygroscopic expansion (CHE) of the cap and ridge layer is selected according to Dawson et al. [19] measurement: α_{Cap}= 0.20 ± 0.04 and α_{Ridge}= 0.06 ± 0.02.

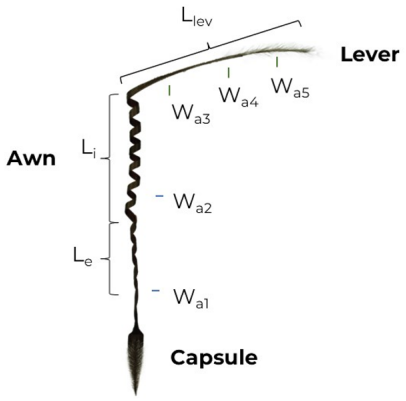

Pelargonium Appendiculatum	
Number Samples Analysed	10
Mass dry (mg)	5.2±0.2
Mass wet (mg)	6.8±0.8
L_i dry (mm)	13.4±0.8
L_i wet (mm)	21.7±1.1
L_e dry (mm)	4.3±0.4
L_e wet (mm)	5.2±0.3
L_{lev} (mm)	17.1±2.3
W_{a1} (um)	258±11
W_{a2} (um)	428±38
W_{a3} (um)	212±21
W_{a4} (um)	138±10
N_c	6-7

Figure 4.2: Morphometric analysis of *Pelargonium appendiculatum* seed. The seed is divided into three main components (capsule, awn and lever) and the relative geometrical measurement are reported in the table.

The coiling configuration of the awn is determined by the geometrical arrangement of microfibrils that cause an anisotropic hygroscopic expansion along the main direction, defined by the microfibril angle (MFA). Since this angle is tilted compared to the cell axis, it is possible to define two angles to describe

microfibril expansion: the tilt angle Ψ, which is the angle between the cellulose helix axis and the cell axis, and the cellulose microfibril angle θ in relation to the cellulose helix axis (MFAH). Tilt angle and MFAH are already reported and measured by using small-angle X-ray scattering (SAXS) [14, 40], reported in Table 2.1. Furthermore, from a macroscopic point of view, the helical motion of the awn can be predicted considering the radius (R), which represents half of the cylindrical helix diameter, and the pitch (P), or rather the spatial period of windings along the cylinder helix axis, as a function of RH (ϕ).

According to the data provided in literature, further extended with thickness and nanoindentation characterization, we were able to predict the kinematic deformation of the awn using the theory of laminate composite anisotropic plates, where only thickness is involved in deformation (Chapter 3). Figure 4.3 show pitch and radius variation as a function of ϕ measured in a climatic chamber at 30 C, with humidity increase from 30% to 90% with 10% step variations in $\Delta\phi$. Each level of humidity was fixed for at least 5 minutes, to overcome the moisture diffusion limit in the cap layer. Figure 4.3 shows that kinematic modeling predicts coherently the geometrical variation of P and R in the whole range of RH considered.

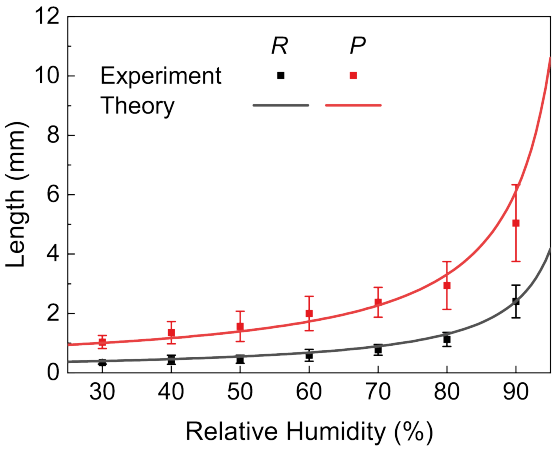

Figure 4.3: Comparison between laminate composite model and experimental results in measuring kinematic parameters (pitch and radius) as a function of RH.

The ability of the seed to move, interact with objects, self-dig and consequently explore soil is mediated by the extensional force F and moment M_0 (as combination of bending and torsion) that can be generated by the awn during the variation of RH. Since water diffusion in the cap layer is mediated by Fickian mechanism [29, 40], we first provide an evaluation of diffusivity D, defined as $D = h_c^2/t_s$, where h_c is the thickness of cap layer and t_s is diffusion time: $2.3 \pm 0.7 \times 10^{-11}$ m^2/s.

We experimentally measured the torque at the end of the lever (which represents the moment arm) and the extensional force during uncoiling, by abruptly increasing RH from 35% to 90% using water aerosol. In Figure 4.4, we report the extensional force and moment: considering well-fitted prediction of static behavior, time-variation in experimental results is mainly associated with buckling. Maximum force is reached at t = 65 ± 12 s, with a value of F_{Max}= 5.1 ± 1.1mN , while the model prediction is F_{Model}= 5.6 mN. The reduction of extensional force is not only associated with Young's modulus reduction due to increasing water content in the cap layer tissue [45], but it is also related to the reduction of spring deflection with the increase of RH. The maximum moment modulus is equal to 20.7 ± 2.5 μNm reached at time 104 ± 23 s, while

the model prediction is 57.7 μNm. This overestimation (within the same order of magnitude) is because the model does not consider the buckling effect: abrupt variation of moment is repeated cyclically because the awn periodically loses contact with the force sensor due to cylindrical axis deformation.

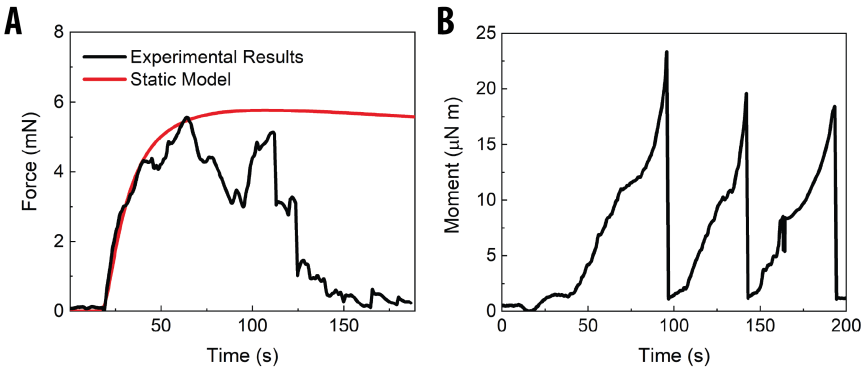

Figure 4.4: Extentional force and moment of *Pelargonium appendiculatum*'s awn. A) Comparison between time evolution of extensional force F and relative behavior of the static model. B) Time evolution of moment M0.

Considering that the model predicts within the confidence interval kinematic and static of awn of P. appendiculatum, we used it as a reference calibration to design the hygroscopic actuator for the artificial seed.

4.1.3 4D printing of the hygroscopic actuator

4D printed structures can reshape in a pre-programmed and passive manner over time due to RH changes and may be accompanied with function evolvement in the process [50, 51]. We exploited this advantage to realize a hygroscopic actuator capable of mimicking the deformation of the awn through a bilayer structure. The inactive layer was fabricated through FDM printing of PCL thermoplastic. Then, we activate the hydrophobic PCL surface with oxygen plasma to increase the adhesion with hydrophilic fibers. Finally, we deposited on the top of the substrate PEO/CNC hygroscopic fibers using coaxial electrospinning. The coupling of FDM and electrospinning techniques permits to realize a support inactive structure independently from the design of active fibers, increasing the degrees of freedom in the prototyping of soft robots.

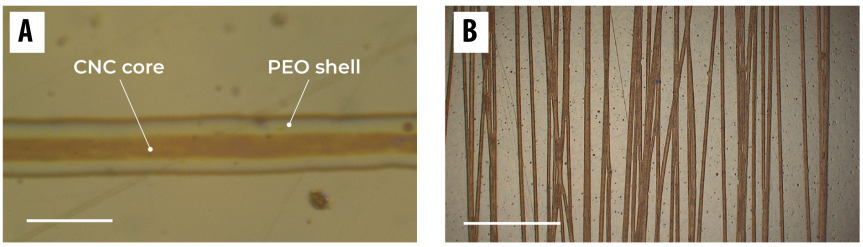

Figure 4.5: Electrospun PEO-CNC fiber. A) Optical image of a coaxial fiber. The shell is composed of PEO and the core by CNC. The difference in color of the fibers is due to the birefringence caused by different refractive indexes of the materials involved. Scalebar 15μm. B) One round trip cycle of electrospun fibers on sample substrate. Scalebar 500μm.

Electrospun hygroscopic fibers compose the active layer and are formed by a core element of CNC and a shell of PEO (Figure 4.5A). The two materials are characterized by an enzymatic biodegradable behavior [52, 53]. The coaxial electrospinning approach has two main advantages in developing hygroscopic actuators. First, CNC shows a reinforced stiffness potential when included in a polymer matrix, increasing the hygroscopic deformation capabilities [59]. Second, considering that water adsorption is a superficial phenomenon, the PEO coefficient of hygroscopic expansion is not altered by CNC since they are fully included in the PEO shell. In Figure 4.5B we evaluate the morphology

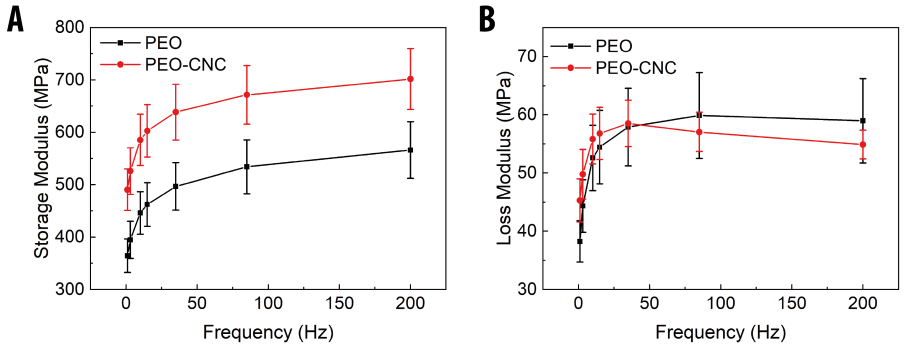

Figure 4.6: Dynamic nanoindentation coaxial PEO/CNC electrospun fibers. A) Storage modulus. B) Loss modulus.

and orientation of fibers. The mean diameter of a fiber is 12.7 ± 0.9 μm (n=33), with a CNC core diameter of 5.4 ± 1.2 μm (n=10). Furthermore, the fibers show an orientation degree of 90° ± 3°, therefore the fibers mainly align along the electrospun direction.

We performed dynamic nanoindentation on polymeric fibers. The obtained results (Figure 4.6) show a statistically relevant increase of Storage modulus compared to homogeneous PEO fibers (paired t-test $p^* < 0.05$), increasing the value by 34.62%, from 364.5 ± 31.9 MPa to 490.2 ± 39.8 MPa, with constant temperature T= 25 °C and humidity RH= 50%.

To understand the mechanical behavior of bilayers, we carried out a tensile test in a climatic chamber to define Young's modulus of the PEO/CNC fibers layer (Figure 4.7). The material shows a decay in stiffness with the increase of RH, both in longitudinal and transversal arrangements. Experimental results are interpolated by cubic-polynomial fitting. Although the mechanical properties of the fiber layer are anisotropic, the addition of the CNC core increases the transversal stiffness compared to the experimental results on PEO fibers provided in the literature [30]. Since the hygroscopic expansion phenomenon involves surface adsorption of water, we consider the CHE value of PEO reported in the literature [30, 40]: α_{PEO}= 0.10 ± 0.03.

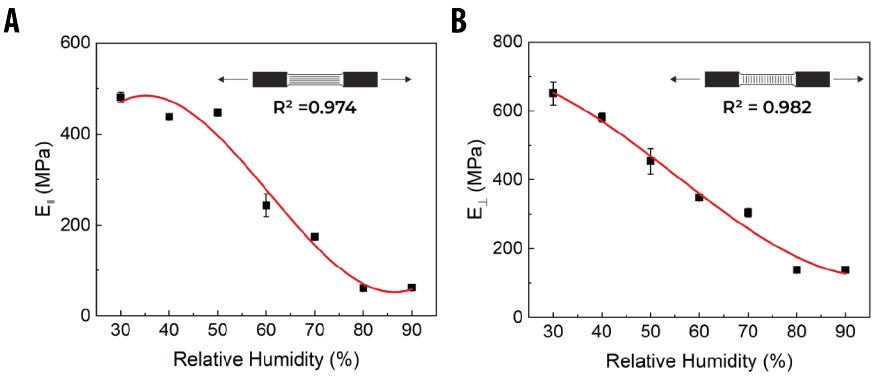

Figure 4.7: Evaluation of Young's modulus in PEO/CNC fibers as function of RH. A) Fibers longitudinal Young's modulus. B) Fibers transversal Young's modulus.

The passive layer of the hygroscopic actuator is realized in PCL, a thermoplastic semi-crystalline aliphatic polyester. This material is selected because of its biodegradability, both hydrolytic and enzymatic, chemical resistance, humidity inertness, flexibility, and elongation capabilities [52]. Furthermore, it is suitable to print with FDM in a one-step process and apply geometrical features according to a specific design. We printed testing beams in PCL with length l = 30 ± 0.5 mm, width w = 5.0 ± 0.5 mm and thickness t= 123.3 ± 6.8 μm (n = 5). Considering the low melting point of PCL (60 °C), we chose to print on a

heated plate (40 °C) to fuse the patterned fibers. The result is a homogeneous flat substrate with no preferential direction (isotropic behaviour). To increase adhesion between hydrophobic PCL and water-based electrospun fibers, we performed a surface activation through oxygen plasma, and we verified the effects of the treatment through contact angle measurement: samples processed with 150W plasma for 30s show a statistically significant (paired t-test $p^* < 0.05$) reduction of the contact angle from 69.8° ± 1.1° to 26.6° ± 3.3°. Moreover, to understand the effects of plasma treatment on elastic modulus, we carried out dynamic nanoindentation on PCL structure. This characterization shows that treatment does not change with a statistical relevance the Storage Modulus (paired t-test $p^* > 0.05$): 254.3 ± 16.1 MPa at a testing frequency of 1 Hz (n = 5).

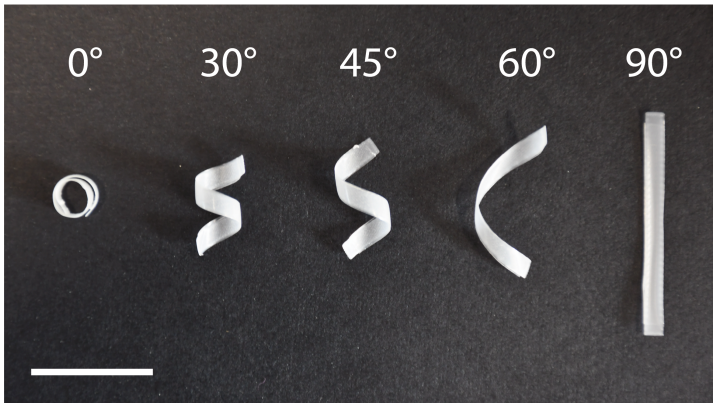

Figure 4.8: Deformation behavior of bilayered beams, with fibers oriented at different angles. Scalebar is 2cm.

We then manufactured five flat bilayered beams (Figure 4.8) with electrospinning, depositing fibers with different orientations (0° 30° 45° 60° 90°). In Figure 4.9 we can observe SEM images of 90° sample, both in surface and cross-section. Fibers tend to conglomerate in a continuous structure during deposition, maintaining their directionality. From a morphological point of view, we deposited an active layer of thickness equal to h_a= 72.9 ± 6.5 μm. Processed structures show bending and torsional deformation thanks to the fiber tilt angle and the relative longitudinal expansion of hygroscopic fibers. Specimens show reversible coiling/uncoiling behavior as the awn in Pelargonium.

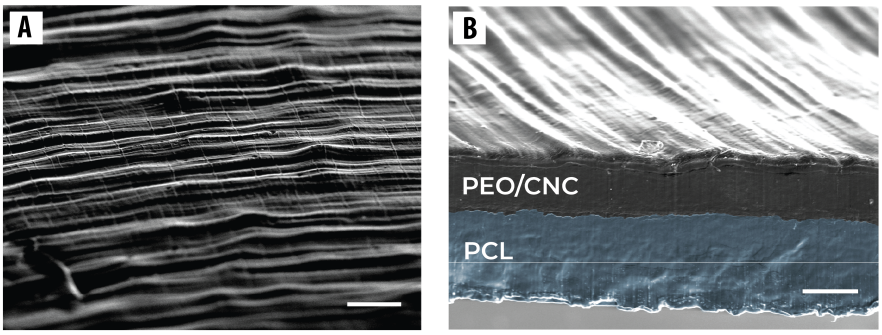

Figure 4.9: Surface morphology and cross section of the actuators. A) SEM picture of the beam surface highlighted the fibrous composition at the top of the active layer. Scalebar 50 μm. B) SEM picture of the beam cross-section, realized through blade cut. The sample preparation for this analysis required a dehydration protocol, in which the hygroscopic actuator was heated at 40°C under vacuum overnight. Then, we proceeded to cut the structure with a lancet for the cross-section visualization. Because of these destructive operations, the fibers tend to conglomerate, avoiding the observation of the internal structure. Scalebar 40 μm.

4.1.4 Design and performance of the artificial seeds

We designed a seed-like soft robot, following a biomimetic approach, based on biomechanical characterization of P. appendiculatum, the modeling procedure, as well as the 4D printing technique and materials characterization previously reported. The whole design, 4D printing process and material training are reported in Figure 4.10.

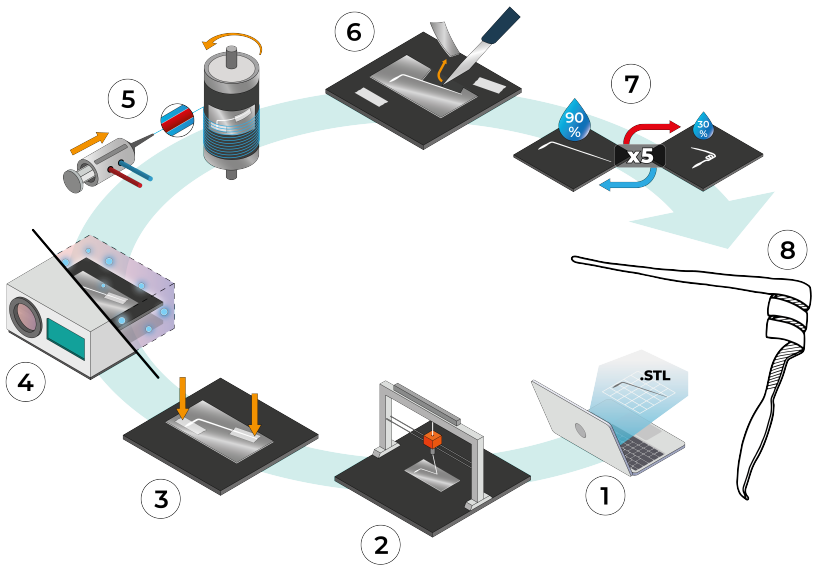

Figure 4.10: Schematic representation of the 4D printing processing. (1) Design of the seed with CAD software for .stl production. (2) FDM printing of PCL on aluminum foil paper. (3) Adapting tape on artificial capsule and lever section. (4) Surface activation through oxygen plasma of artificial awn. (5) Hygroscopic functionalization of the artificial awn through coaxial electrospinning of PEO/CNC. (6) Blade cut of the structure from aluminum-foil paper. (7) 4D deformation in a climatic chamber through 5-times humidity cycles. (8) Example of 4D printed artificial seed.

The design of the artificial capsule was processed considering the contour of the natural one and adapting the relative dimension, which maintains the same scale factor as to the whole size of the artificial seed. The artificial lever is designed considering a triangular profile with a length r = 17 ± 1 mm (n = 5). We model the actuator as in stretching-dominated regime, such that the dimensionless figure of merit $\tilde{w} > 1$.

In agreement with the model, we selected width b = 1523 ± 54 μm, length l = 30.3 ± 1.1 mm, passive layer thickness of h_p = 100.7 ± 4.6 μm and active layer thickness h_a = 72.9 ± 6.5 μm (n = 5). Following a biomimetic approach, we set the direction of fiber deposition equal to the tilt angle Ψ = 15° of the natural seed, to better compare natural and artificial seed performances. We recall that PEO/CNC fibers present a longitudinal hygroscopic expansion, while pure cellulose is subjected to transversal expansion [40]. After fiber deposition, the artificial awn starts to deform according to the humidity level. We then accelerated the deformation transient process (i.e. material training) by changing the humidity level in the climatic chamber. Consequently, they show a completely reversible and reproducible (n = 15) behavior after 5 ± 1 humidity cycles (from RH = 30% to 90%). Overall, the volumetric dimension of the artificial seeds is 10 times bigger than the natural ones. The mass of the device is equal to 21.6 ± 0.4 g (four times the mass of a natural seed), while the artificial awn shows a mass of 12.6 ± 0.6 g (n = 5). Next, we evaluated the equivalent kinematic parameters of the artificial seed following the same characterization procedure made for P. appendiculatum. We model the mid-curve reconstruction according to Eq.3.20. In Figure 4.11 we observe that the model predicts within a confidence interval of 99% the experimental results of pitch and radius variation as a function of RH.

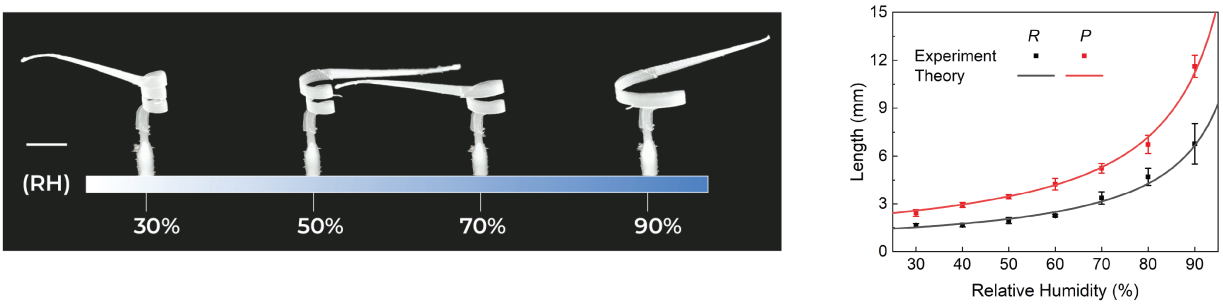

Figure 4.11: Kinematic characterization of the artificial seed. A) Experimental visualization of pitch and radius as a function of relative humidity. B) Comparison between laminate composite model and experimental results in measuring kinematic parameters (pitch and radius) as a function of RH.

Considering the kinematic variation of the structure, we measured the diffusion constant on the fiber layer, obtaining a diffusivity of $4.7 \pm 0.5 \times 10^{-11}$ m^2/s, almost two times higher than the natural one.

Finally, we evaluated the extensional force and moment in the artificial seed, and performances compared to the natural one (Figure 4.12). The maximum force is reached at t = 123 ± 32 s, with a value of F_{Max}= 2.40 ± 0.58 mN, while the model prediction is F_{Model}= 2.0 mN. Moment measurement exhibited a maximum value at t = 112 ± 24 s, with $M_{0_{Max}}$= 30.4 ± 5.1 μN m and $M_{0_{Model}}$=33.4 μNm. In this case, the awn does not lose contact with the force sensor, because the structure did not show cylindrical axis deformation. The artificial seed has slower dynamics than P. appendiculatum since the law of diffusivity scales linearly with the thickness of the active layer and it is inversely proportional to square root diffusivity. Upon exposing the artificial seed to 100 cycles of RH variation between 0.3 to 0.9, we found that the amount of change in curvature was less than 10%.

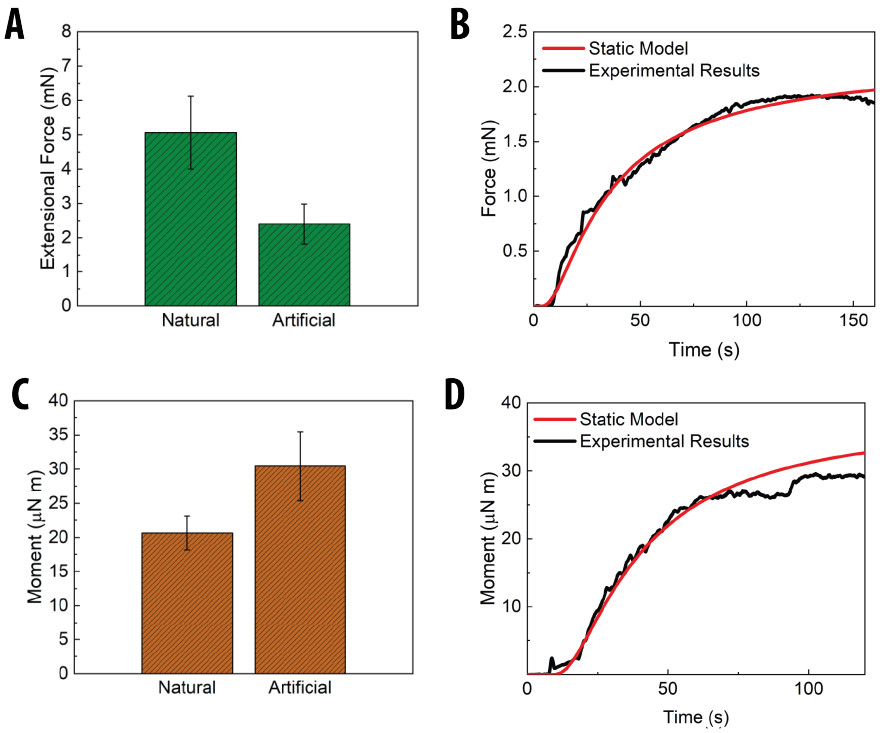

Figure 4.12: Static characterization of artificial seed. A) Comparison between natural and artificial seed performances in extensional force, considering width b = 1.52 mm, length l = 30 mm, tilt angle 15° and printing direction 70°. B) Extensional force comparison between experimental and modeling results. C) Comparison between the experimental evaluation of moment in the natural and artificial seeds. C) Moment comparison between experimental and modeling results.

To understand the abilities of the artificial seed in humidity-driven soil exploration, we first performed a lifting analysis (Figure 4.13). Once we observed

self-lifting in artificial samples, we tested the maximum stress performances of the device. We fixed the artificial lever and tied 1g weight to the artificial capsule and, by changing the humidity level from 35% to 90%, the hygroscopic actuator lifted about 120 times its weight by 5mm. Considering that the water adsorption enthalpy is the only source of energy, the absolute potential energy related to the lifting process was $\simeq 49\mu$J. The main limitation associated with this observation is the reduction of ultimate tensile stress of the hygroscopic layer with the increase of RH. Consequently, the fibers have a mechanical yield, which does not allow the structure to return to its initial position.

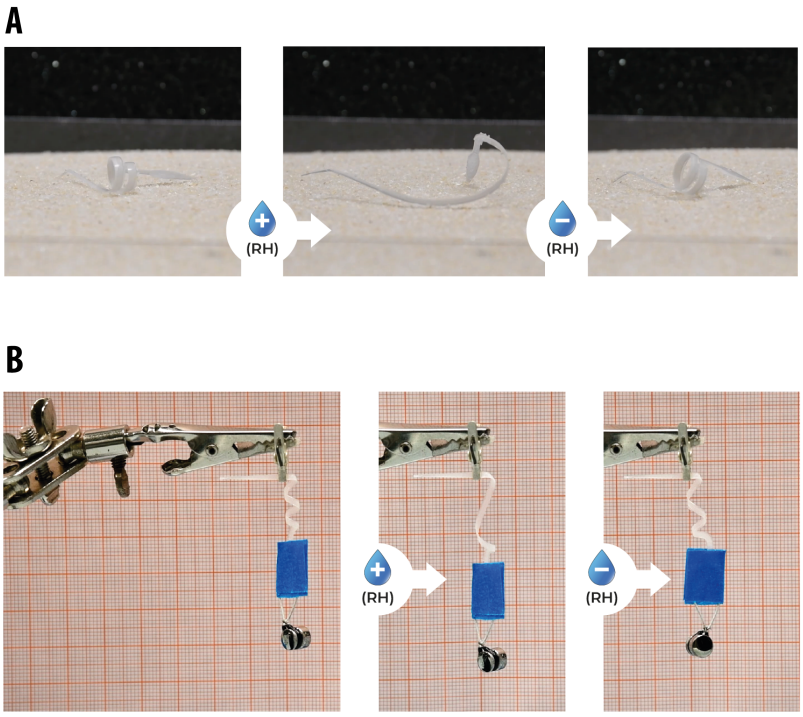

Figure 4.13: Lifting performances of the artificial seed-like robot. A) Example of the artificial seed self-lifting. B) From idle conditions (RH = 35%) the artificial seed is subjected to abrupt variation of humidity with water aerosol (RH = 90%). Water desorption is then promoted by environmental humidity.

We investigated the movement of the artificial seed in sample soil: the test consists of monitoring and tracking the spontaneous movements of the seed-like robot due to humidity changes in randomly distributed clay. The hygroscopic actuator (artificial awn) was used as a biomimetic propulsor, matched with the capsule and the lever which act as anchoring points (or interaction points) for the hygroscopic actuator.

The substrate was composed of variable roughness and fractures to have the widest possible range of dynamic interactions between the terrain and the device. The fractures represent 8.95% of the whole surface, with an average roughness of 5 mm. The test was done in a climatic chamber, with T = 30°C and RH changing linearly from 30% to 90% (triangular shaped function). The climatic chamber provides a homogeneous distribution of humidity, so there is not a preferential direction in the RH source. In Figure 4.14 it is possible to observe the movement of four different artificial seeds after 19 humidity cycles. The RH cycle is represented by a triangular waveform ϕ(t) with a rise/fall time of 30mins per cycle.

In the first approximation, the time-varying behavior of the specimen can be modeled as a succession of random steps in a three-dimensional continuous

space (random walk). Therefore, the initial position of the seed determines the random evolution of the whole system, since the device chaotically interacts with soil and fractures. The reversible shape commutation mechanism is then a successful approach for soil exploration if the soil presents variable geometrical and physical properties since the soft robot progressively moves towards a fracture only if he can interact with the soil roughness.

The coiling/uncoiling behavior is confirmed by motion tracking of the seed capsule since the mean speed measurement follows linearly the duty cycle of periodic humidity input. Moreover, we verified that the dispersing movement of the artificial seeds is mediated by the autonomous adaptation of the soft body across the soil, highlighting different classes of behavior: North-West seed penetrates with the capsule a fracture 3 cm far after 12 humidity cycles (0.63 ± 0.42 mm/cycle); South-West seed presents a directional movement, with a mean speed of 0.93 ± 0.90 mm/cycle, reaching a peak of 6 mm/cycle and at the 19th RH cycle anchors both capsule and lever in a fracture; North-East and South-East seeds roll over a confined position during all the experiment, due to lever anchoring with soil fractures.

The natural and artificial hygroscopic seed actuators show an energy density of 564.80 kJ/m^3 and 52.16 kJ/m^3 (power-to-mass ratio of 423.62 μW/kg and 154.38 μW/kg), respectively. The experimental energy density of the actuator reaches a peak of 4 J/kg, value that is comparable with the current state-of-art for soft hygroscopic actuators (from 0.5 to 10 J/kg).

Table 4.1: Artificial seed's awn modeling parameters and results.

	Ridge Layer	**Cap Layer**
Geometrical parameters		
Length [mm]	30.3±1.1	
Width [μm]	1523±54	
Thickness [μm]	100.75±4.62	72.93±6.47
MFA [deg]	/	15±3
Material properties		
Young's Modulus [GPa]	0.49±0.04	0.25±0.02
Poisson's coefficient [a.u.]	0.442	0.36
CHE [a.u.]	0	0.1±0.03
Dynamic parameters		
Weigth [mg]	21.6±0.4 (12.6±0.6)	
Diffusivity [m^2/s]	4.69±0.48 $\times 10^{-11}$	
Max Force [mN]	2.40±0.58	
Model Force [mN]	2.03	
Max Torque [μN m]	30.42±5.06	
Model Torque [μN m]	33.35	

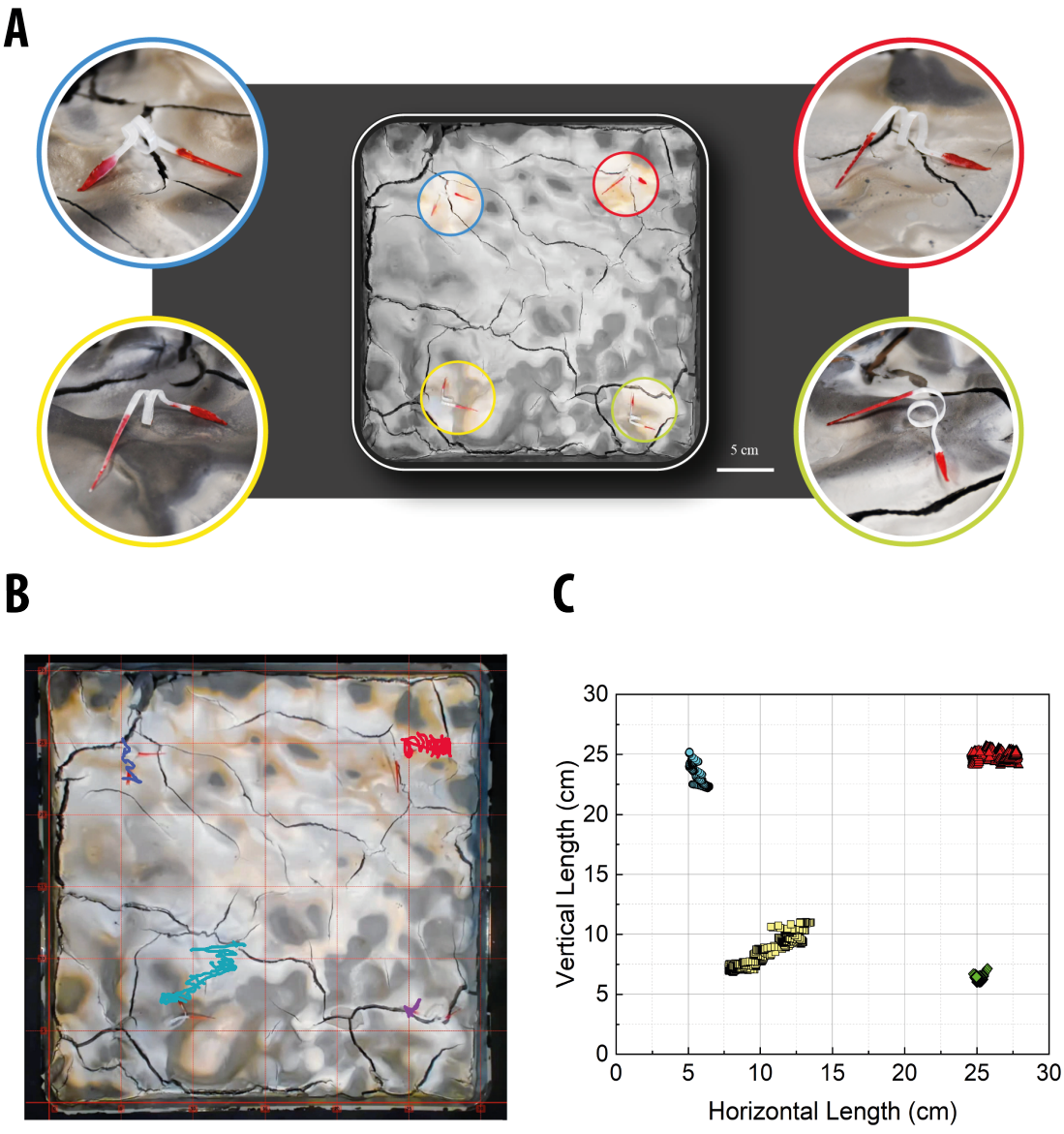

Figure 4.14: Artificial seeds in humidity-driven soil exploration. A) The initial condition of two different samples placed on artificial clay soil. The central image represents the top view of the soil. The corner arrangement was chosen to minimize the interaction among the different specimens. The final position of the samples after 19 humidity cycles in a climatic chamber (T = 30°C and RH range from 30% to 90%). Due to humidity-driven motion, the artificial seeds interact with multifaceted soil and its cracks. Scalebar is 5 cm. B) Motion tracking provided elaborating with Kinovea software. C) Motion tracking representation in 2D Cartesian coordinate system.

4.2 A Hygroscopic Seeds-Inspired Robot for Visual Humidity Sensing

Visual sensors designed for measuring relative humidity (RH) play a crucial role in decentralized and self-sufficient environmental monitoring systems. Many existing visual humidity sensors rely on colorimetric sensing, employing hygroscopic inorganic pigments or photonic crystals (PCs). However, the potential environmental hazards associated with the toxicity of certain inorganic pigments pose a concern, especially during in-situ measurements. Additionally, PCs, due to their angle-dependent structural colors, are not ideal for autonomous and in-situ environmental monitoring. In this study, we introduce a novel visual humidity sensor utilizing an artificial, hygroscopic seed-like robot inspired by the *Pelargonium appendiculatum* seed [38]. The design of artificial seed is bioinspired by the hygroscopic and layered tissues of the seed, and it is manufactured using additive techniques with biodegradable polymers. The hygro-mechanical response of artificial seed leads to reversible changes in the artificial seed structure, specifically the angular displacement and diameter variation of the awn, in relation to RH. These variations in geometric properties can be accurately measured and correlated with RH across a wide range (30%-90%), achieving an accuracy of 97-98%. The sensor demonstrates a high resolution within the range of 0.176-0.521% of RH and exhibits good reproducibility, with an average Relative Standard Deviation (RSD) of 14.7%. The straightforward and inventive method employed in creating a hygrometer is appealing for producing a new category of hygro-mechanical instruments. These instruments boast high precision and accuracy, while also being extremely cost-effective, environmentally friendly, and easily interpretable without the need for onboard electronics.

4.2.1 Materials and Methods

Humidity sensing with natural Pelargonium appendiculatum and artificial seeds robot: Humidity sensing measurements and calibration with the activated and hygroscopically-responsive artificial seed were carried out in climatic chamber (CTC256, Memmert GmbH, Germany), fixing temperature T = 30°C (resolution= 0.5 % and an accuracy=1 %). The choice of temperature value was chosen to guarantee the maximum humidity dynamics of the machine, that ranges from 30% to 90% with steps of 10% every 10-20 minutes. Response times (Rt, s) and sensitivity (S, °/s) were evaluated through the abrupt increase of humidity from 30% to 90% using a water aerosol. Videos and pictures were acquired using Logitech Brio Stream, Logitech (Swiss), aligned to Pelargonium appendiculatum seed or artificial seed and placed at a distance at a distance of 10 cm. The videos and picture were elaborated with Editor Video (Windows 10, Microsoft). Digital measurement of the awns' angle displacements and of the awns' radius changes related to the humidity content in the air was carried out using ImageJ software.

4.2.2 Hygromechanic sensing of *Pelargonium appendiculatum* and artificial seed

In the first step, we studied the applicability of the hygromechanic effect of the natural *Pelargonium appendiculatum* for visual humidity sensing purposes.

The camera position was selected to be orthogonal to the central axis of the helicoidal awn to evaluate digitally the angular displacement of the lever at different RH values with ImageJ Figure 4.15. We monitored the differential angular displacement of the lever angle (Δ, °) every RH steps equal to 10%, or compared to the initial lever position at RH=30% (Δ30, °) testing spanning RH conditions (30-90%). The response time (Rt expressed in s) and the sensitivity (S, expressed in °/s) related to Δ_{30} were also monitored.

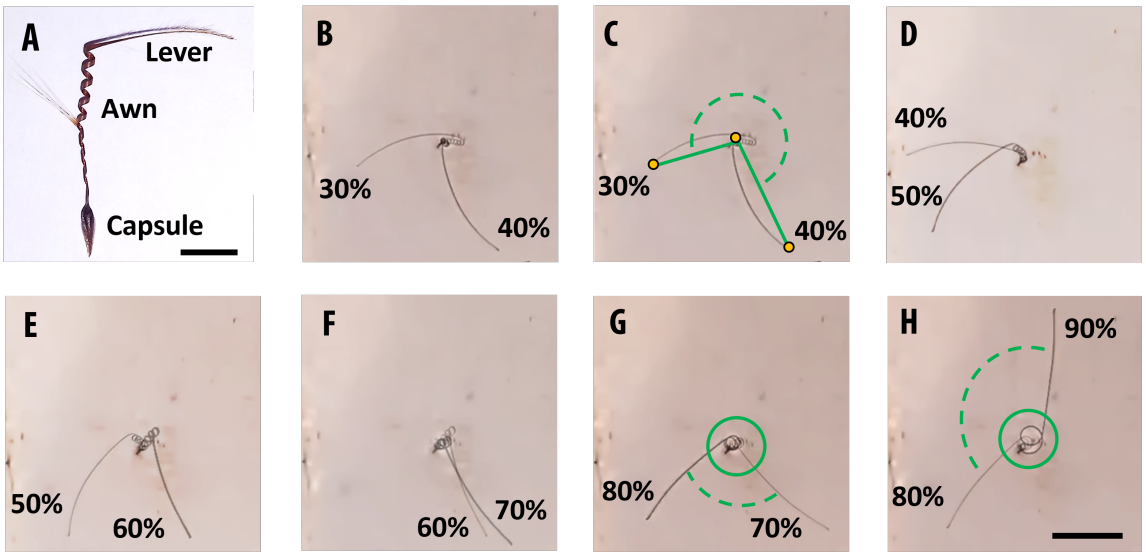

Figure 4.15: Angle variation in *Pelargonium appenmdiculatum* as function of RH. A) Picture of a Pelargonium appendiculatum seed showing capsule, awn, and lever. Scalebar is 1 cm. B) Superimposed captured frame of the Pelargonium appendiculatum seed lever position at %RH values of 30% and 40%. C) Angle displacement measurement of the lever rotation from RH 30-40%. C-H) Superimposed frame of the Pelargonium appendiculatum seed lever rotation at different %RH variation: 30-40% (C); 40-50% (D), 50-60% (E), 60-70% (F), 70-80% (G), and 80-90% (H).

Figure 4.15 shows a progressive increase in angular displacement as the RH increases. Compared to the initial lever position for RH=30% the angular displacement Δ_{30} (°) vs. RH (%) could be fitted with linear function Δ_{30}= 38.1 RH(%) – 1334 (R^2 = 0.985) (Figure 4.16). In first approximation, the data extracted from the geometrical characterization of the seed over different RH values proved that the geometrical parameter changes (i.e., awn's lever angular displacements) due to the hygro-mechanical response of *Pelargonium appendiculatum* could be visually quantified and correlated for visual humidity sensing purposes.

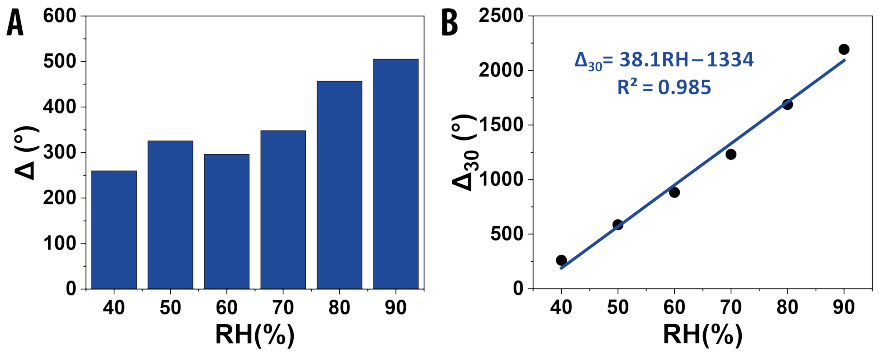

Figure 4.16: Hygromechanic sensing of *Pelargonium appendiculatum*. A) Diagram showing Angle variation (Δ) at different RH value for *Pelargonium appendiculatum* seed lever. B) Angle variation compared to RH= 30% (Δ_{30}) at different RH value for *Pelargonium appendiculatum* seed lever. Linear fitting functions are also reported (RH(%)).

The response times (Rt, s) and sensitivity to RH variation (S, °/s) from 30% to 90% RH were also evaluated accordingly to the procedure reported in Experimental Section. The Rt was 207s and the calculated sensitivity was 10.6 °/s. After assessed the suitability of the natural *Pelargonium appendiculatum* seed

as a visual humidity sensor, we tested the performance of the artificial seed (with statistical validation) using the previously reported setup and experimental methodology.

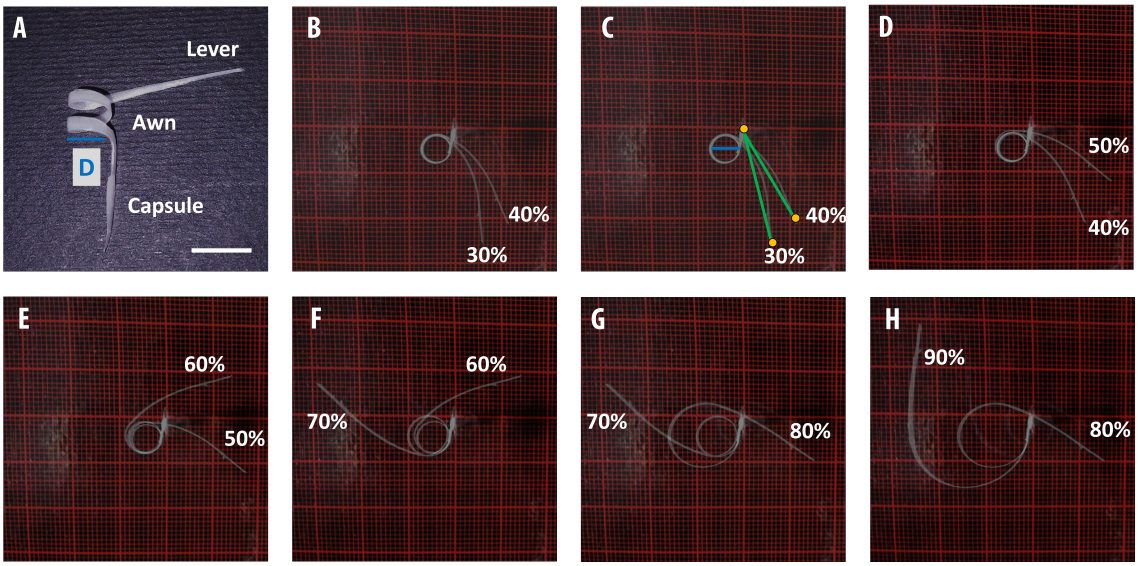

Figure 4.17: Angle variation in artificial seed as function of RH. A) Picture of a artificial seed showing capsule, awn, and lever. Scalebar is 1 cm. B) Superimposed captured frame of the Pelargonium appendiculatum seed lever position at %RH values of 30% and 40%. C) Angle displacement measurement of the lever rotation from RH 30-40%. C-H) Superimposed frame of the *Pelargonium appendiculatum* seed lever rotation at different %RH variation: 30-40% (C); 40-50% (D), 50-60% (E), 60-70% (F), 70-80% (G), and 80-90% (H).

The design and manufacturing of 4D printing of a soft seed-like robots is reported in [38]. The artificial seed was conceived for explore the soil passively, driven by humidity changes, and penetrates fractures similarly to the natural ones, for environmental exploration and monitoring. In this research, the awn's lever angular displacements (Δ and Δ_{30}), once inserted the capsule in a hole, were measured as a function of the humidity for humidity sensing measurements (Figure 4.18).

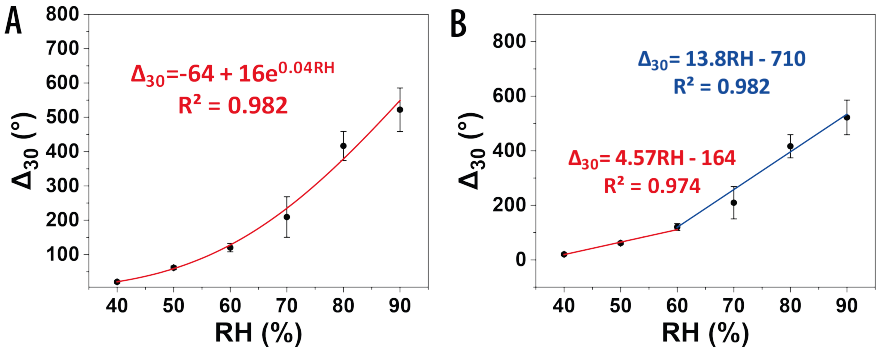

Figure 4.18: Hygromechanic sensing of artificial seed. A) Diagram showing Angle variation (Δ) at different RH value for *Pelargonium appendiculatum* seed lever. B) Angle variation compared to RH= 30% (Δ_{30}) at different RH value for Pelargonium appendiculatum seed lever. Linear fitting functions are also reported (RH(%)).

In addition, from a macroscopic point of view, the helical motion of the awn and of the lever could be predicted considering the diameter of the awn (D). Also, D was measured and correlated to the humidity changes. Considering the geometrical parameters that characterize the hygroscopic actuator (length, width and thickness), the structure behaves like a laminate composite where only thickness participates in the deformation of the body. This hypothesis is valid if and only if the thickness is sufficiently lower with respect to width and length (Kirchhoff assumption). Therefore, for the proposed design the variation of radius, pitch and angles as function of RH are independent on width and length.

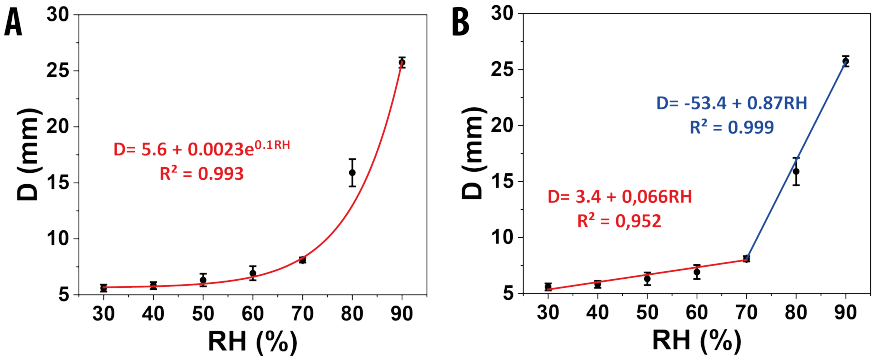

Figure 4.19: Diameter variation of artificial seed as function of relative humidity. A) Diameter fitting behaviour. B) Two-steplinearization of diameter.

Figure 4.18 and Figure 4.19 reports the angular and diameter variation for the artificial seed as the RH increases from 30% to 90%. The achieved data confirmed that artificial seed could be used as visual humidity sensor considering the angular variation displacement Δ_{30} at the different RH. The reproducibility expressed as average relative standard deviation (RSD) for Δ_{30}, at the different humidity levels, was 14.8% (n = 4). The trend could be fitted with logistic exponential (sigmoidal function, (R^2=0.982, Figure **??**A). The exponential fitting (i.e., the increase of sensitivity with the increase of the humidity) is in agreement with the decrease of the storage modulus of PEO fibers and coaxial PEO/CNC fibers of the artificial seed (hygroscopic section) with the increase of RH measured through tensile test dynamic nanoindentation in [30, 38]. Alternatively the trend can be fitted approximately with two linear function (Figure **??**B) for perspective sensing applications: Δ_{30} = 4.57 RH(%) – 164 (R^2 = 0.974 (RH ≤ 60%)) and Δ_{30} = 13.8 RH(%) – 710 (R^2 = 0.982, (RH ≥ 60%)). The reproducibility expressed as average relative standard deviation for D at the different humidity levels was 5.8% (n = 3). The trend can be fitted with exponential function, D(mm) = 5.6(mm) + 0.0023 exp $0.1RH(\%)$ (R^2 = 0.993) or alternatively with two linear function D(mm) = 0.066 RH(%) + 3.4(mm) (R^2 = 0.952 (RH ≤ 60%) and D(mm) = 0.87RH(%) – 53.4(mm) (R^2 = 0.999 (RH ≥ 60%)).

Rt (s) of the artificial seed showed an average value of 85.3 ± 9.3s for the whole tested humidity ranges 30-90%. The Rt was the 41.2% of Pelargonium appendiculatum one. This result proved the artificial seed was faster in terms of Rts (i.e., more responsive) than the natural seeds (Figure 4.20A). The average angular/temporal sensitivity (°/s) of the artificial seed was 5.61 ± 1.67 °/s and it was roughly the 53% compared to the Pelargonium appendiculatum one (Figure 4.20B).

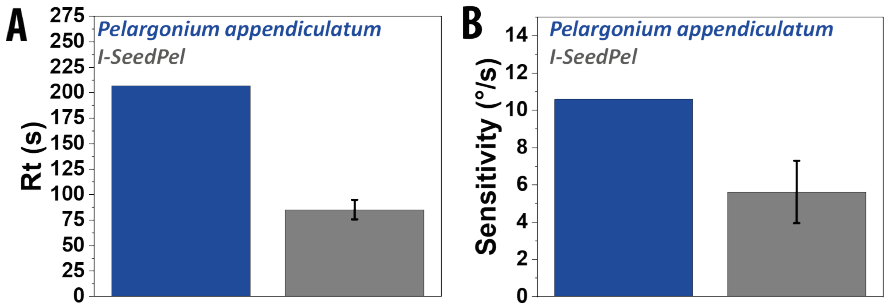

Figure 4.20: Response time and sensitivity of natural and artificial hygro-mechanic sensor. A) Response time (Rt, s) of the Pelargonium appendiculatum seed and artificial seed levers from 30-90% RH. B) Sensitivity (°/s) of the *Pelargonium appendiculatum* seed and artificial seed lever from 30-90% RH.

We also estimated the resolution (R) of the artificial seed RH sensor in terms of %RH, considering the lower measurable lever angular displacement by our camera after a zoom of 2X and 6X and after a post-processing image analysis. We defined the angular displacement Δ_r resolved when the distance between

the acquired levers (before and after the humidity changes) was equal to the thickness of the lever itself. A $\Delta_R = 2.36°$ was measured. Considering the two linear fitting reported in Figure 4.20 two different humidity sensor resolutions R were calculated: 0.52% and 0.17% for the linear fitting with slope 4.57°/% (RH ≤ 60%) and 13.8 °/% (RH ≥ 60%), respectively. It is interesting to point out that R values achieved are much lower than those of colorimetric systems based on photonic crystals or interferometric films which range from 1.5 to 10% [60].

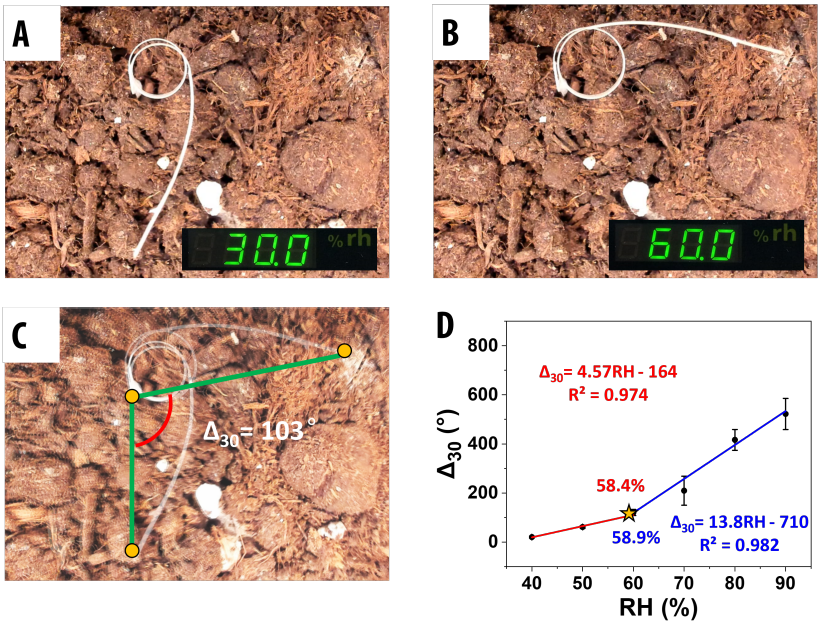

Figure 4.21: On soil measurement of RH for artificial seed. A) Picture of the artificial seed lever at a RH value of 30% once the artificial seed is inserted in the ground. B) Picture of the artificial seed lever at a RH value of 60% once the artificial seed is inserted in the ground. C) Angle measurement of the lever angular displacement from RH= 30% (A) to RH= 60%. D) Interpolation of the RH(%) value considering the linear fitting reported in Figure 4.18B, for the accuracy measurement evaluation

In addition, we would like to stress that this type of sensor, made of biodegradable materials and battery-free has a resolution comparable to the DHT11 temperature and humidity digital sensor (1%) [61, 62]. All the reported performances confirmed the suitability of the artificial seed for the environmental RH measurements. At this purpose, as a simulation of a perspective real application case, we put the artificial seed on a model soil, testing RH variation from 30% to 60% and recording the Δ_{30} angular variation displacement (Figure 4.21) and exploiting the linear relationships reported in Figure 4.18B. The measured Δ_30 was 103° and from the linear interpolations, the achieved RH values were 58.4% and 58.9% (Figure 4.21) resulting in a high accuracy of 97.3% and 98.1%, respectively. Alternatively, using the exponential interpolation reported in Figure 4.18 (Δ_{30}= -64 + 16 exp $0.04RH$), the achieved RH value is 58.6%, resulting in a similar accuracy of 97.7%. These results confirmed the feasibility of using this autonomous green sensor, powered by humidity itself and made of biodegradable polymers, for humidity measurements on the field.

4.3 A Plasmonic Actuator Sunlight-Driven by a Photothermal-Hygroscopic Effect

The photothermal effect is a phenomenon associated with the photoexcitation of a material, that adsorb electromagnetic energy and dissipate as thermal energy. The exploitation of this effect has attracted particular attention in the field of sustainable actuators, as it is possible to implement a wireless device using sunlight as a source. Combined photothermal-hygroscopic effects enable novel materials actuation strategies based on renewable and sustainable energy sources such as sunlight. Plasmonic nanoparticles have gained considerable interest as photothermal agent, however, the employment in sunlight-driven photothermal-hygroscopic actuators is still bounded, mainly due to the limited absorbance once integrated in nanocomposite actuators and the restricted plasmonic peaks amplitude (compared to the solar spectrum). Inspired by the hygroscopic behaviour of Geraniaceae' seeds, we focused the goal of our research on the use of cellulose as building-block of hygroscopicity and increasing the dynamic performance of an hygroscopic actuator by accelerating its desorption processes through photothermal effects.

We report a nanoparticles based plasmonic and photothermal-hygroscopic actuator driven by sunlight. Specifically, a trilayer structure was implemented, with a PDMS base layer (BL) for structural support upon which a nanometric middle AgNPs layer (Plasmonic Photothermal Layer, PPTL) was synthesized for exploiting heat generation upon solar radiance, and an upper anisotropically hygroscopic layer (HL), based on cellulose, devised to finally transduce actuation through bending. As regards the photothermal mechanism, the AgNPs were synthesized by adapting a single-step, in-situ, and fluoride-assisted synthesis reduction protocol recently disclosed by one of the authors [63, 64], only using the PDMS layer (as reducing agent) and AgF in ethanolic solution. Such a novel synthesis allowed the achievement of high-yield surface coverage (40%) of AgNPs firmly anchored to the PDMS surface, with broadband and high absorption value in the visible range (>1) and a P.C.E. around 40% under 1 Sun irradiation (100 mW/cm^2).

As regards the hygroscopic mechanism, aligned tracks of hygroscopic carboxymethyl cellulose (CMC) were printed on the BL/PPTL actuator by taking inspiration from the Geraniaceae seed structure. Since cellulose materials have a hygroscopic and water-swelling nature thanks to the abundant hydrophilic groups, we adopted CMC because it is an anionic charged cellulose derivative with a more pronounced water-swelling ratio than native cellulose.

Thanks to the photothermal effect of AgNPs, the loss of humidity induced in the CMC enacts actuation, with strong curvature changes (over 40%) in a short response time (6.8 ± 0.3 s) and a force generation of 0.76 ± 0.02 mN under 1 Sun irradiation. A laminate composite plates model predicted the kinematics and the statics under controlled humidity exposure [38]. Moreover, crawling, coiling/rolling, gripping and weightlifting capabilities were also demonstrated for a rectangular actuator, as well as shape reconfiguration illustrated by implementing the trilayer into an actuator devised for programmed motion responsive to sunlight. The achieved results disclose the possibility of using sunlight to drive photothermal-hygroscopic actuators based only on plasmonic MNPs as photothermal agents.

4.3.1 Materials and Methods

Materials and chemicals: Silver fluoride (AgF, 99.9%), absolute ethanol (EtOH, 99.9%), Carboxymethyl cellulose (CMC) were purchased from Merck Millipore (Massachusetts, USA). Polyvinyl alcohol (PVA, 98-99% hydrolyzed, high molecular weight) was purchased from ThermoFisher Scientific (Massachusetts, USA). PDMS (polydimethylsiloxane), Sylgard 184 base and thermal curing agent were purchased from Dow Corning Corporation (USA). Deionized water (DIW) was purified by Arium-advance EDI (Sartorius, Germany) and filtered using syringe filters (Minisart NML Syringe Filters 1.20 μm, (Sartorius, Germany).

Preparation of the BL/PPTL/HL actuator: The actuator consisting of PDMS (Base Layer, BL) decorated with silver nanoparticles (AgNPs, Plasmonic Photothermal Layer, PPTL) and Carboxymethyl cellulose (CMC, Hygroscopic Layer, HL), printed by Direct Ink Writing (DIW). PDMS was prepared by mixing base and curing agents (10:1, w:w) and then vacuumed for 30 min using a rotation pump to avoid the formation of air bubbles. Then 0.50g of the mixture was poured into a polystyrene Petri dish (9 cm in diameter) and spin coated (1200 rpm for 60 s). The PDMS was then thermally cured in the oven (Vacutherm, Thermo Scientific, USA) at 80°C for 90 minutes.
A 20 mM AgF ethanolic solution was used for the synthesis of AgNPs on PDMS. 20 ml of solution was cast in a 9 cm Petri dish for 30, 60, 120, 240, and 360 minutes at room temperature (i.e., 20°C). After decoration, the PDMS/AgNPs in the Petri dish was thoroughly rinsed with ethanol and dried under a gentle nitrogen flow.
The PDMS/AgNPs surface was treated with air/oxygen plasma (Tergeo, Pie Scientific, LLC, USA) to increase its hydrophilicity. The plasma time was set to 60s, gas stability time to 15s, power setpoint to 75W, gas setpoint 30 sccm (cm^3/min) and base vacuum to 0.50 mbar. The activated PDMS/AgNPs surface was spin-coated with PVA (1ml, 1% in DIW, 4000 rpm for 60s), according to the procedure reported in [65] to stabilize the hydrophilicity PDMS and dried in the oven at 80 °C for 15 minutes.
Carboxymethyl cellulose (CMC) was printed via Direct Ink Writing (DIW) using a 3DBioplotter, EnvisionTEC (Germany). CMC hydrogel was prepared in deionized water (10% w/w) under magnetic stirring for 4 hours at 60 °C and then vacuumed to remove air bubbles and poured in the 3D Bioplotter nozzle. The CMC was printed directly on the PDMS/AgNPs activated surface using a conical nozzle with a 200 μm diameter and by fixing the printing plate temperature at 25 °C. The extrusion pressure was set at 1.7 bar and the printing speed at 33 mm/s. The nozzle offset was fixed at 160 μm for beam samples with a distance between the strands of 1.5 mm. The printed CMC tracks were dried in the oven at 80° for 1 h.
Direct-write CO2 laser (Flux BEAMO, Flux Europe) with tunable laser power, speed, and resolution was then used to cut and pattern the PDMS/AgNPs/CMC surface to fabricate a wide range of soft actuator designs and configurations. Test rectangle samples (2.0 × 1.0 cm) were cut and peeled off from the Petri dish.

Surface activation: Contact angle measurements were carried out with an optical tensiometer (Theta OneAttension, Biolin Scientific, Sweden) to evaluate the success of the surface treatments.

Morphological characterization of the PDMS, PDMS/AgNPs and PDMS/AgNPs/CMC surface: Morphological surface characterization was performed using a Helios NanoLab 600i Dual Beam Focused ion beam/field-emission

SEM instrument (FEI, USA). The size, distribution, and surface coverage of AgNPs were evaluated by post-processing the images with ImageJ software. Images of the cross sections were also acquired after cutting with a razor blade. Hirox KH-7700 digital microscope (Japan) was also used for morphological characterization.

Optical characterization of the PDMS/AgNPs surface: Transmittance spectra of the PDMS/AgNPs samples (1cm × 1cm × 50 μm), synthesized at different times (30-360 minutes), were collected with a LAMBDA 45 spectrophotometer (Perkin Elmer, USA) in the UV-Vis range (400-1000 nm wavelength). Reflectance spectra of the PDMS/AgNPs samples, synthesized at different times (30-360 minutes), were collected with a UV–vis–NIR light NanoCalc-XR source and spectrophotometer (Micropack Ocean Optics, USA). Acquisition parameters of the transmittance spectra were: integration time of 1000 ms, average scan number 1, boxcar width 0.

Photothermal characterization of the PDMS/AgNPs surface: Photothermal characterization of the PDMS/AgNPs samples (1cm × 1cm × 50μm), synthesized at different times (30-360 minutes), was carried out with an IR thermal camera (A700, FLIR Systems, USA). The experiments were performed in ambient air (about 20 °C, 60% RH). The samples were irradiated under laser light using RLTMDL-808-1W, 808 nm (Roithner Lasertechnik, Austria), 1 W cw laser at different powers (100-1000 mW, 250-2500 mW/cm^2) or simulated sunlight using a SciSun 300 Solar Simulator (Sciencetech, Canada) at different powers (50-150 mW/cm^2, 0.5-1.5 Sun) with intermitting solar irradiation (60s irradiation / 60s of darkness). Power densities of the laser were calculated after the measurement of the power exiting from the fiber with a power meter (Nova II, Ophir, Israel) and the measurement of the irradiated surface with an IR thermal camera (A700, FLIR Systems, USA). Power densities of the simulated sunlight were verified using an RS PRO solar energy meter (RS, UK).

Tape test of the PDMS/AgNPs surface: Tape tests were carried out on the PDMS/AgNPs surface (240 minutes synthesis) to investigate the adhesion properties of the nanoparticles. Tesa® Professional 53988 tape (Germany) tape and the PDMS/AgNPs surface were put in contact applying a pressure of 570 kPa for 1 minute, with a peeling angle of 90°. The tape was then peeled off and the reflectance spectra of the PDMS/AgNPs surface was acquired as reported in Optical characterization of the PDMS/AgNPs surface to monitor possible changes due to nanoparticle transfer from PDMS to the tape surface.

Tape test of the PDMS/AgNPs/CMC surface: Tape tests were carried out on the PDMS/AgNPs/CMC surface to investigate the adhesion properties of the CMC tracks on the PDMS/AgNPs layer mediated by PVA. Tesa® Professional 53988 tape (Germany) tape, with a tensile strength of 25 N/cm, and the PDMS/AgNPs/CMC surface were put in contact applying a pressure of 570 kPa for 1 minute, with a peeling angle of 90°. The tape was then peeled off and the integrity of the CMC tracks was examined through microscopy with a Hirox KH-7700 (Japan).

Mechanical characterization: We evaluate the stress-strain relation of PDMS/AgNPs (BL/PPTL) synthesized with AgF for 240 minutes and CMC (HL) using a tensile stress test (ZwickRoell Z100). We used a 1kN sensitive load cell, with a speed test of 500 mm/min and 100 mm/min for PDMS/AgNPs and CMC, respectively, and with a pre-load of 0.05N. Young's modulus and Poisson's ratio of PDMS/AgNPs do not give statistically relevant differences with respect to the blank PDMS. The geometrical features of the dumbbell

specimens were: length 35 mm, width 4 mm and thickness 50 μm. CMC samples were prepared using the bar coating technique (bar thickness 1mm, speed 20 mm/s) with a DIW solution of 10%wt CMC. Samples were subsequently laser cut in dumbbell specimen shape with geometrical dimensions: length 35mm, width 4 mm, thickness 100 μm.

Curvature radius measurement: The evaluation of macroscopic geometrical features allowed us to describe the bending deformation, and therefore the kinematics of the actuator. We calculated the relative humidity variation of the curvature in a climatic chamber (CTC256, Memmert GmbH) with the temperature fixed at 30°C. This value was set to guarantee the maximum humidity dynamics of the machine, which ranges from 30% to 90% RH. After comparing kinematics with modelling results, we were able to determine the curvature time evolution time of the curvature and so, the diffusivity of the cellulose layer. The procedure consisted in: abruptly increase in the humidity level using a water aerosol (from 40% to 80%); the collection of visual data with a camera; data analysis with the software ImageJ [66]. We used the same approach to evaluate the curvature kinematics and the curvature evolution time when the sample was irradiated by sunlight.

Force measurements: The PDMS/AgNPs/CMC moment was evaluated under RH increase (from 60% to 90%) and 1 Sun at RH=60%. In the experimental setup, the samples were in contact with a suspended 10g sensitive load cell (Futek LSB200, USA). The load cell was calibrated (mV vs mN) using samples with a weight force equal to 0.59 mN.

Pictures and video acquisition: Videos and pictures were acquired using Logitech Brio Stream, Logitech (Swiss) and elaborated with Editor Video (Microsoft Windows).

4.3.2 Synthesis and characterization of PDMS-AgNPs layer

Figure 4.10 illustrate the fabrication of the plasmonic photothermal-hygroscopic nanocomposites consisting in: 1) PDMS preparation (Base Layer, BL); 2) in-situ synthesis of plasmonic AgNPs (Plasmonic Photothermal Layer, PPTL); 3) CMC printing using Direct Ink Writing (Hygroscopic Layer, HL). The multilayered structure BL/PPTL/HL was actuated by photothermal-hygroscopic effect under 1 Sun irradiation.

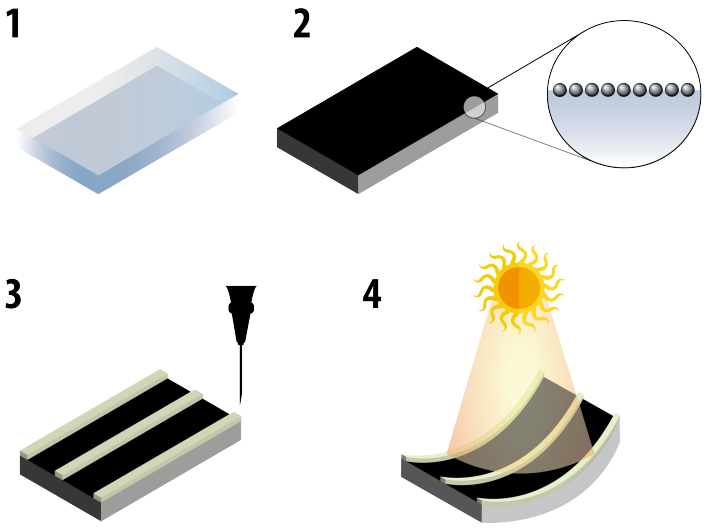

Figure 4.22: Fabrication sketch of the photothermal-hygroscopic actuator consisting of: 1. PDMS preparation (Base Layer, BL); 2. In-situ synthesis of plasmonic AgNPs through a fluoride-assisted method (Plasmonic Photothermal Layer, PPTL); 3. Carboxymethyl Cellulose (CMC) printing on PPTL through Direct Ink Writing (DIW) (Hygroscopic Layer, HL); 4. Photothermal-hygroscopic actuation under 1 Sun.

The thickness of the PDMS (BL) was 49 ± 4 μm (n = 8). AgNPs were formed on the PDMS adapting the one-step and in-situ redox reaction occurring between unreacted Si-H bonds of the curing agent and Ag^+ available in the ethanolic AgF solution. The fluoride ions in the metal solution improved density and accelerated the kinetics of the synthetic process with respect to state-of-the-art fluoride-free approaches [63].

Figure 4.23A shows both blank PDMS (not decorated, BL) and PDMS decorated with AgNPs by casting 20 mM AgF ethanolic solutions for different times (PPTL), namely from 30 to 360 minutes. PDMS showed from brownish to black color intensities increasing with the decoration time. This effect is ascribable to Localized Surface Plasmon Resonance (LSPR) cumulative absorption of the formed NPs, which increase both in size and distribution, combined with a plasmonic interparticle coupling as previously reported both for AgNPs (adsorbed onto solid surfaces) [67] and AuNPs in liquid solutions **[kwon]**.

SEM analysis of the PDMS petri decorated in ethanolic solutions of AgF at 60, 120, 240 and 360 minutes is reported in Figure 4.23B. SEM EDX analysis for the AgNPs synthesis of 240 minutes, shows the appearance of a strong Ag signal (Weight%= 63.88 ± 0.35%) due to the in-situ synthesis. It is interesting to note that the oxygen signal (due to Si-O-Si bonding in the PDMS structure) is higher (Weight%= 11.26 ± 0.58 %) compared to the expected one (Weight%= 9.28 %) and this is due to the oxidation of the silicon during the in-situ redox reaction as reported in [68, 69].The AgNPs average sizes increased from 21 nm to 35 nm as the decoration time increased from 60 to 360 minutes (Figure 4.23C). All the NPs distributions were well fitted by Gaussian profiles (R^2=0.99) Figure **??**. The surface coverage of the AgNPs was 23.31%, 40.36%, 40.72% and 41.02%, for 60, 120, 240 and 360 minutes of decoration, respectively.

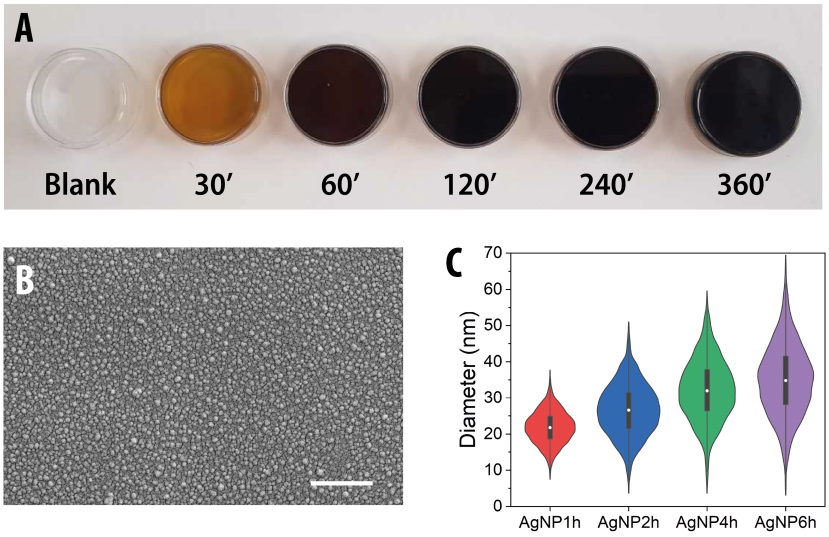

Figure 4.23: PDMS-AgNPs substrate. A) Pictures of PDMS prepared in Petri dishes and decorated with AgNPs in a fluoride solution (i.e., 20 mM AgF) for 30-360 minutes. B) SEM image of the PDMS surface decorated with AgNPs for 240 minutes. Scalebar is 1 μm. C) Violin plot of the size distribution for the decorated samples.

We monitored the decoration process by using VIS absorption spectroscopy (Figure 4.24) after the measurement of the reflectance and transmittance spectra in the visible range (400-900/1000 nm) given that the sunlight simulator has significant irradiance values only between 400-1000 nm. In the spectrum recorded at t = 30 min an intense absorption peak (A_{max} 1.4) appeared at 400 nm, which was associated with the LSPR of the spherical AgNPs [63]. At t = 60 min and 120 min the LSPR had a broader band, which agreed with: the increase in AgNPs size; the broadening of the distribution recorded; the increase of the surface

coverage and the interparticle coupling [63]. At t= 240 and 360 min, a further broadening of the LSPR peaks was observed with an absorbance value over the whole wavelength range (400-900 nm) of roughly 1.2 and 1.1. The higher absorbance value for the sample synthesized after 240 minutes compared to the 360 minutes could be explained by the lower reflectance.

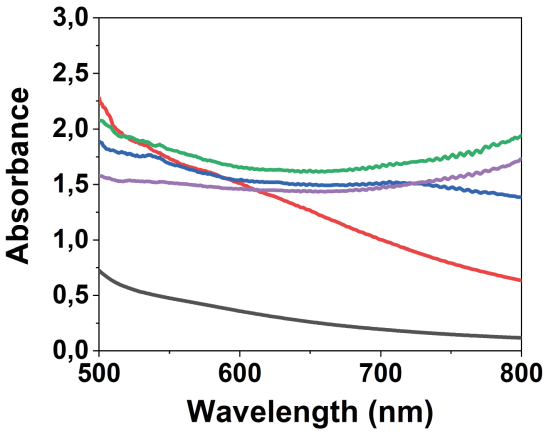

Figure 4.24: Absorbance spectra of PDMS decorated with AgNPs. Black curve is PDMS subjected to 30′ of decoration. Red, Blue, Green and Violet are respectively 1h, 2h, 4h, 6h of decoration.

The synthesized BL/PPTL nanocomposites were then tested in photothermal conversion upon irradiation with visible light by simulating the sunlight radiation, with a power density of 100 mW/cm^2 (1 Sun) in air, and using a thermocamera (Figure 4.25). All the photothermal profiles showed an increase in temperature over time well-fitted with an asymptotic exponential trend (R^2=0.99). The trend of the maximum ΔT (°C) vs decoration times reached the maximum value in the BL/PPTL samples decorated for 240 minutes with AgNPs (ΔT 14.6 ± 0.3 °C after 7s of irradiation, n = 3). This decoration also showed the highest temperature gradient upon illumination (7.3 ± 0.4 °C/s for t= 0s, n = 3).

We tested the adhesion properties of AgNPs formed on PDMS in a 20 mM AgF ethanolic solution for 240 min. Differently from the conventional premixing of photothermal agents (e.g., CNT) [70], the in-situ synthesis of AgNPs onto the PDMS surface did not change mechanical properties significantly. In particular, the Young's Modulus of PDMS and PDMS/AgNPs (240 minutes synthesis) were not statistically different, being 2.55 ± 0.52 MPa and 1.95 ± 0.34 MPa, respectively. For the above-mentioned reason, the BL/PPTL sample decorated

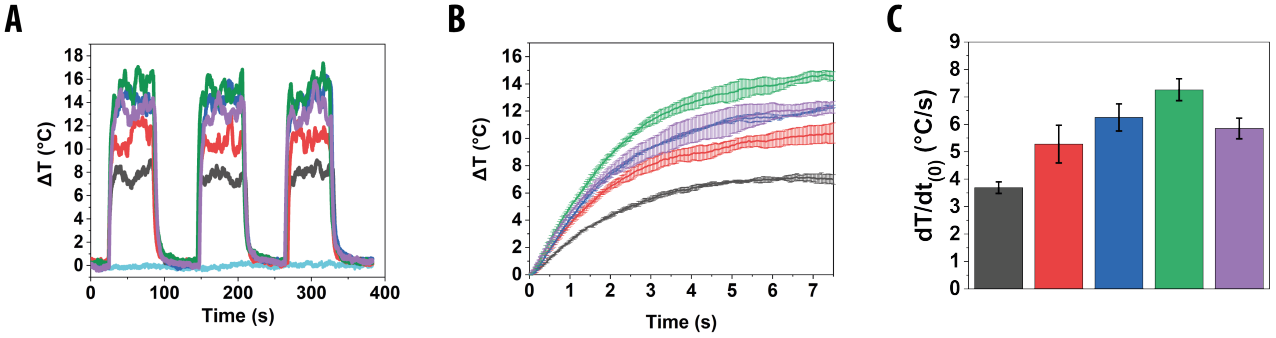

Figure 4.25: Photothermal behaviour of decorate PDMS samples. A) Temperature variations (ΔT, °C) over time on the PDMS/AgNPs samples and exposed to a solar simulator light with a power density of 100 mW/cm^2 with intermitting solar irradiation (60s irradiation / 60s of darkness). B) Synchronized temperature variations (ΔT, °C) over time on the PDMS/AgNPs samples. Data are provided as average values over 3 replicates with error bars representing one standard deviation. C) Temperature sensitivity of the samples.

for 240 minutes with AgNPs was used for the subsequent development of the photothermal-hygroscopic actuator.

4.3.3 Photothermal effect: evaluation of photothermal conversion efficiency in thin layers

To understand the effectiveness of decoration treatment, we analyse the standard figure of merit of photothermal materials, η the photothermal conversion efficiency (PCE). It is defined as the ratio of thermal power (extinction) over the absorbed optical power (absorption), and it gives an indication of the temperature kinetics when an electromagnetic wave impinges the photothermal materials.

We model the heat transfer of a thin layer structure composed by photothermal layer on top of passive substrate, suspended in air and subjected to surface homogeneous and synchronous electromagnetic irradiation (e.g. Laser, SUN simulator). At first, we evaluate the internal conduction problem. Due to homogeneity condition, we assume that the surface of the whole structure is coherently at the same temperature. This permits to reduce the problem from 3D to 1D. Let's consider a one-dimensional uniform and isotropic material, with a photothermal source on the top of the surface. The heat equation is then described as:

$$\frac{\partial T}{\partial t} = \frac{k}{\rho c_p} \frac{\partial^2 T}{\partial z^2} \tag{4.1}$$

where k is the thermal conductivity, c_p the specific heat capacity, ρ the density, $T = T(t, z)$ describe the temperature in the domain of the active layer $z \in [0, h]$ (z is the coordinate describing the thickness of the active layer) and the time $t \in [0, \infty)$. The boundary conditions for the heat equation are:

$$T(0, t) = T_s(t); \quad T(z, 0) = T_0$$

The thermal diffusion time τ_T is is consequently derived as:

$$\tau_T = h^2 \frac{\rho c_p}{4k} \tag{4.2}$$

Assuming that the thickness of the structure is sufficiently thin such that $h \longrightarrow 0$ (*thin film approximation*), we can state isothermal condition in the entire structure. From an experimental point of view, this assumption is valid if the diffusion time is at least two orders of magnitude lower with respect to the characteristic time of the photothermal effect, as defined later on. It is now possible to evaluate the photothermal conversion efficiency considering the conservation of energy. We model the body as a 2D isothermal horizontal plate, heated by irradiation (photothermal property), which exchange heat with atmospheric air in natural convection regime (infinite reservoir at constant temperature T_{Air}). The heat transfer can be written as:

$$\frac{\partial Q_r(\lambda)}{\partial t} - \frac{\partial Q_c}{\partial t} = \sum_{i=1}^{N} m_i c_{p_i} \frac{\partial T_i}{\partial t} = \frac{\partial T}{\partial t} m c_p \tag{4.3}$$

where Q_r is the irradiation heat,Q_c the convection heat and m the mass. The convection heat transfer for a 2D isothermal plate is defined as:

$$\frac{\partial Q_c}{\partial t} = h_t S \left(T(t, \lambda) - T_{Air} \right) \tag{4.4}$$

where h_t is the average heat transfer coefficient, S the surface exposed to atmospheric air. We model the irradiation heat transfer according to Beer-Lambert's law:

$$\frac{\partial Q_r(\lambda)}{\partial t} = \eta(\lambda) I_0(\lambda) \left[1 - 10^{-\alpha(\lambda)}\right] \tag{4.5}$$

where I_0 the optical power, α the absorbance and λ the wavelength of the impinging light source. Combining together Eq.4.3 4.4 4.5 we obtain:

$$\frac{\partial T(t,\lambda)}{\partial t} = \eta(\lambda) \frac{I_0(\lambda)(1 - 10^{-\alpha(\lambda)})}{mc_p} - \frac{hS}{mc_p}[T(t,\lambda) - T_{Air}] \tag{4.6}$$

Considering T_0 as an arbitrary initial temperature, the non-homogeneous linear ordinary differential equation admits a solution equal to:

$$T(t,\lambda) = T_{Air} + \frac{A(\lambda)}{B}(1 - e^{-Bt}) + (T_0 - T_{Air})e^{-Bt} \tag{4.7}$$

where:

$$A(\lambda) = \eta(\lambda) \frac{I_0(\lambda)(1 - 10^{-\alpha(\lambda)})}{mc_p} \tag{4.8}$$

$$B = \frac{hS}{mc_p} \tag{4.9}$$

Hence, we used the experimental results of temperature kinetics to fit A and B considering the characteristic time $\tau = 1/B$ and the variation of temperature $\Delta T = A/B$. The PCE is finally evaluated as:

$$\eta(\lambda) = A(\lambda) \frac{mc_p}{I_0(\lambda)(1 - 10^{-\alpha(\lambda)})} = \frac{\Delta T(\lambda)}{\tau(\lambda)} \frac{\rho_1 c_{p_1} t_1 + SC\rho_2 c_{p_2} t_2}{J_0(\lambda)(1 - 10^{-\alpha(\lambda)})} \tag{4.10}$$

Where ρ is the density, t the thickness, J_0 the optical power density, 1 and 2 refer to PDMS and AgNPs materials, respectively, SC the surface coverage of AgNPs. It is now important to note that for each wavelength of the input light source there is a unique value of $A(\lambda)$, and so a unique solution of the PCE.

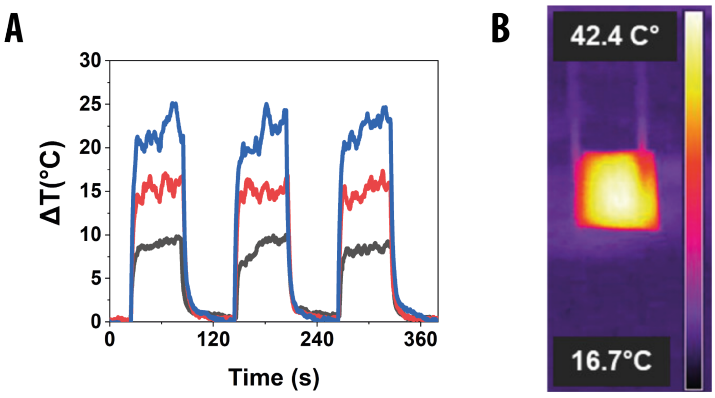

Figure 4.26: Photothermal properties of PDMS-AgNPs sample decorated for 4h. A) Temperature variations (ΔT, °C) over time on the PDMS sample with AgNPs decorated for 240 minutes and exposed to solar simulator light with different power densities of 50, 100 and 150 mW/cm2 (0.5, 1 and 1.5 Sun, Black, Red and Blue respectively) and with intermitting solar irradiation (60s irradiation / 60s) of darkness. B) Photothermal camera image of the PDMS surface decorated with AgNPs for 240 minutes and exposed to a solar simulator light with a power density of 100 mW/cm^2. The thermal color scale shows the maximum and minimum temperature values recorded in the image.

The photothermal conversion efficiencies (η) calculated were 31.3%, 40.8%, and 30.1% for 120, 240 and 360 minutes of decoration times, respectively. The higher η value for the 240 minutes of decoration agrees with the higher absorbance values reported in Figure 4.24. For completeness, the photothermal properties of such BL/PPTL layer were also evaluated at other sunlight power densities (i.e., 0.5 and 1.5 sun) (Figure 4.26) and under IR laser irradiation at 808 nm at high power density (1586 mW/cm^2). Under laser irradiation, the surface

temperature reached the value of 208.2 ± 0,6 °C (n = 3) in 7 seconds. Interestingly the reached value was higher than the one obtained using a PDMS layer with a similar thickness (66 μm) and covered with graphene (one of the most exploited materials for photothermal actuation) and AuNPs as photothermal enhancers i.e., 150°C under an IR laser (808 nm) and a similar irradiation power (3000 mW/cm^2). The PCE results for single wavelength laser source and broad solar spectrum agreed: 41.7% and 40.8%, respectively.

4.3.4 Design of the phothermal-hygroscopic actuator

We designed the BL/PPTL/HL actuator, taking inspiration from the hygroscopic multi-layer structure of the Geraniaceae seeds. To guarantee adhesion between hydrophobic PDMS/AgNPs substrate and hydrophilic cellulose layer, we used air plasma followed by the nanometric coating with PVA, as described in the protocol reported in [71]. The combined plasma oxidation and PVA treatment has been reported to be long-term stable, ensuring long-term hydrophilicity of the PDMS surfaces in contrast to the only plasma oxidized PDMS, which tends to regain its surface hydrophobicity 1 day after treatment. The increase in hydrophilicity was confirmed by the contact angle analysis (Figure 4.27).

SEM EDX analysis for the AgNPs synthesis of 240 minutes before and after the use of air plasma shows the O% weight increases from 11.26 ± 0.58 % to 11.87 ± 0.10% (n = 3). However, this increase could not be considered statistically significant (Student's t-test confidence leveln95%). Also, the temperature variations (ΔT, °C) over time (s) under sunlight exposure (1 Sun) did not show a significant variation of the photothermal properties due to plasma.

Based on the mechanical characterization of the materials, we design the CMC layer thickness to minimize the curvature of the actuator. To this purpose, we predict the kinematic behaviour comparing the results of Timoshenko beam model [48], and the laminate composite plates model. In particular, we consider the actuator as a trilayered structure, in which the PDMS/AgNPs passive substrate is stacked with a PVA buffer layer, and the hygroscopic CMC layer is deposited on the topmost part.

CMC hydrogel (10% in deionized water) was printed via DIW on the activated PDMS/AgNPs surface and totally dried in the oven to obtain a pattern of CMC tracks wide 0.91 ± 0.06 mm (n = 6), distanced 0.67 ± 0.02 mm (n = 6)

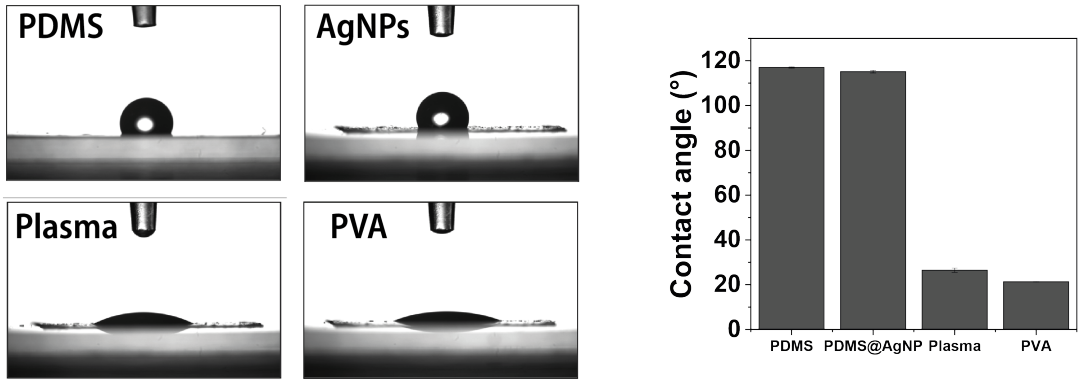

Figure 4.27: Contact angle measurements on the actuator during the different fabrication steps (i.e., PDMS preparation, AgNPs synthesis, plasma treatment and PVA spin-coating with relative water droplet.

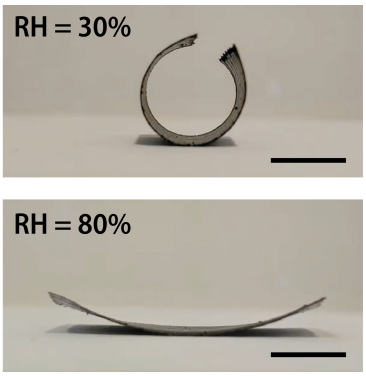

Figure 4.28: Pictures of the BL/PPTL/HL actuator exposed to relative humidity equal to 30% and 80%. Scalebar is 5mm.

and thick 20.8 ± 2.1 μm (n = 6). Accordingly, an equivalent thickness equal to 13.5 ± 2.5 μm was calculated. We tested the adhesion properties of CMC on PDMS/AgNPs surface. The surface microscopy images captured after the adhesion test proved the integrity of the CMC tracks and the good adhesion between the PDMS/AgNPs and CMC mediated by PVA.

Considering the key role played by hygroscopic actuation in the proposed multi-physics-driven system, we preliminarily characterized the actuator response versus RH only. We first addressed the hygromorphic behavior of the considered actuator in regard to both its kinematics (curvature) and statics (force) performance as a function of %RH. When the environmental %RH decreased, it induced a contraction of the CMC tracks, thus increasing actuator curvature (positive curvature intended as the folding of the hygroscopic layer); reciprocally, a decrease in %RH caused a reduction in the actuator curvature, i.e., to unbend (Figure 4.28).

Considering that, at least at a first approximation, the curvature of a thin multilayer (plate) can be modeled regardless of sample width (w) and length (l) [48], so that actuation force is consequently computed per unit width [28], we fixed the geometrical dimensions of the rectangular sample actuator as w = 1 cm and l = 2 cm. We characterized the curvature response in a climatic chamber (Figure 4.29). From the recorded data, we also extracted the humidity value ϕ_0= 80% associated with null curvature, to be used for model calibration. Both laminate composite plates and Timoshenko model predicted the curvature response within 95% confidence interval. These results highlighted that we can accurately control the actuator curvature based on RH.

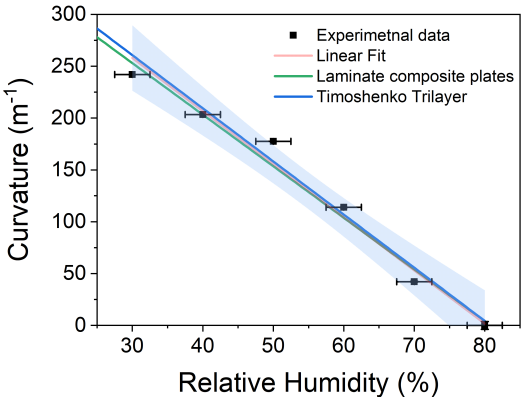

Figure 4.29: Curvature vs. Relative Humidity characterization of photothermal hygroscopic actuator.

We then proceeded to analyze the time response of the hygroscopic actuator. Considering that water adsorption in the cellulose layer was driven by diffusion [28, 30], we first characterized the time evolution of the curvature by increasing the humidity level (step increase from 40% to 80%) using deionized water aerosol (i.e., working conditions over the diffusion limit). Figure 4.30A shows the time behavior of the actuator subjected to an RH stepwise function. During water adsorption, the structure decreased its curvature from κ=2.01±0.15 cm^{-1} to $\kappa = 0 \pm 0.12$ cm^{-1} in τ_{RH} =4.11±0.23 s. Moreover, considering that the actuation was mediated by Fickian diffusion upon the cellulose layer, the diffusivity of CMC layer could be evaluated as $D_{CMC} = h^2_{CMC}/\tau_{RH} = 2.94 \pm 0.34 \times 10^{-11}$ m^2/s. Figure 4.30B reports the force produced by the hygroscopic actuation (under quasi-static conditions) by varying the humidity level from RH = 60% to RH = 80%, with the maximum force equal to F_{RH}= 0.57 ± 0.07 mN. The considered force was predicted by both the Timoshenko model (F_T=0.58 mN)

and the laminate composite plates model (F_{LC}=0.56 mN) within a confidence interval of 95% . The force estimate turned out to be in good agreement with the experimental results (thus corroborating the working assumptions introduced for ease of model derivation).

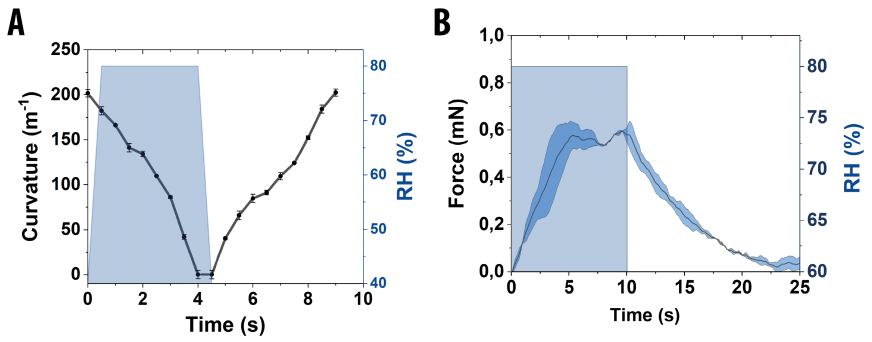

Figure 4.30: Hygroscopic time response of the actuator. A) Curvature of the actuator (m^{-1}) vs time (s) with RH changing from 40% to 80% (average %RSD= 2.7%, n = 3). B) Forces (mN) vs time (s) with %RH changing from 60% to 80%.

Thanks to the photothermal effect, we promoted water desorption increasing the substrate temperature with a broad solar spectrum with 1 Sun power density. Considering water adsorption enthalpy, an increase in temperature at constant environmental RH led to a bending of the actuator. An increase in temperature determined an increase in the rate of humidity desorption and so, the localized amount of humidity in the cellulose layer was consequently reduced. At first approximation, the solar irradiance and humidity could be analyzed as independent variables. We characterized the kinematics and statics of the actuator by varying the optical power density (0.5-1.5 Sun) at a fixed initial (RH = 60%) humidity level (Figure 4.31A). The curvature shows a linear trend (R^2 = 0.99) up to 1 Sun of solar irradiance, above which curvature saturation occurs. Based on the previous characterization results on purely hygroscopic actuation, the residual RH was < 20% on the cellulose layer for solar irradiance > 1 Sun. Figure 4.31B shows the response of the load-free actuator driven at 1 Sun (step application of the solar irradiance). Here, we can observe the combined effect of photothermal conversion and water desorption. The actuator changed its curvature from κ = 1.71 ± 0.05 cm^{-1} to κ = 2.54 ± 0.03 cm^{-1} in t_{Sun}= 6.84 ± 0.26 s. In Figure 4.31C we analyzed the static performance when the actuator was irradiated with a stepwise function from 0 to 1 Sun, reaching a maximum force of F_{Sun} = 0.76 ± 0.02 mN. We tested the non-fatigable reversibility during the actuation at 1 Sun irradiation over 100 cycles. The curvature change was only of 5% in dark condition and 0.5% under irradiation.

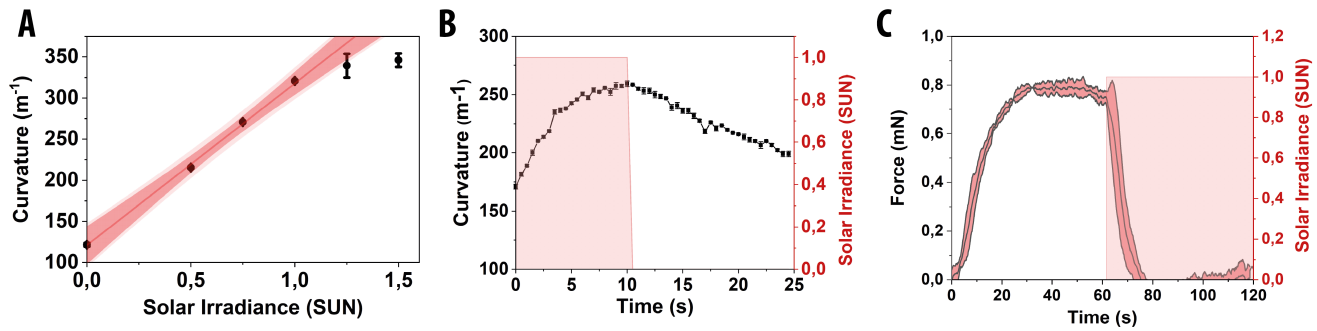

Figure 4.31: Photothermal-hygroscopic time response of the actuator. A) Curvature variation of the actuator vs time (s) exposed to 0-1.5 Sun at a fixed %RH=60%. B) Curvature variation of the actuator vs time (s) exposed to 1 Sun (average %RSD= 0.7%, n = 3). C) Force (mN) vs time (s) of the actuator exposed to 1 Sun at a fixed %RH=60%. Data are provided as average values over 3 replicates with error bars representing one standard deviation.

4.3.5 Photothermal actuator for soft robotics applications: a proof of concept

To illustrate the potential for application of the proposed BL/PPTL/HL actuator, while keeping implementation efforts in line with the present developmental stage, we introduced several sunlight-driven demonstrators, namely grasper, crawler, coiler/roller, weightlifter and a final reconfiguration obtained by implementing an actuator devised for uniaxial programmed motion responsive to sunlight (Figure 4.32).

The BL/PPTL/HL actuator (2 cm × 1 cm × 0.006 cm, mass 13.9 ± 0.9 mg, n = 6) could act as a wireless soft grasper. The soft grasper is shown in Figure 4.32A. With light exposure (1 Sun), the bilayer bent to grip a cargo with size (14 cm × 1.70 cm × 0.75 cm, mass 156 mg). When the light was turned off the cargo was released. In the reported test, the grasper handled a cargo with a mass greater than 11-fold its mass (and a volume greater than about 1500-fold its volume).

A crawler demonstrator (with the same embodiment of the previous grasper) is shown in Figure 4.32B. Locomotion was driven by cyclic irradiance, leading to cyclic contraction/extension of the crawler structure (it contracted under sunlight actuation, and stretched back upon irradiation removal). A constant unidirectional movement was obtained thanks to the different friction forces between the two ends of the actuator, modified with 5 iron threads in front (bent at 110 °) and 5 behind (straight), respectively. The average walking speed upon 4 locomotion cycles was 0.31 mm s^{-1}. The proposed crawler moves at 1 BL/min considering the experimental variation of irradiance as function of time. Considering the driving illumination, the crawler moves at 0.3BL/Sun cycle. Lifting tests on such demonstrators were also reported using payloads of 42.6 and 144.1 mg (3 and 10-fold the actuator mass). Under sunlight exposure the actuator could lift the 42.6 mg payload of 4 mm (work 1.6 μJ) and the 144.1 mg payload of 2 mm (work 2.7 μJ), corresponding to an energy density of 0.13 J/m^3 and 0.22 J/m^3, respectively. A demonstrator capable of coiling/uncoiling (4.5 cm × 0.5 cm × 0.006 cm) (Figure 4.32C) was also implemented by laying the CMC tracks at a 20° angle with respect to the actuator longitudinal axes, similarly to the microfibril angle (MFA) in Geraniaceae seed structures. Such a demonstrator could also be used to implement rolling motions: we obtained an average rolling speed of 0.4 mm s^{-1} upon 2 locomotion cycles, yet further investigations on helical radius reduction and boundary conditions to trigger rolling upon coiling are necessary to design rolling systems with enhanced performance. Taking advantage of the possibility of printing the tracks in different directions on the same BL/PPTL, we have also designed and fabricated a reconfigurable structure devised for uniaxial programmed motion (Figure 4.32D), recalling the uniaxial opening/closing motion of some flowers (e.g., Carlina aucalis). When exposed to 1 Sun, the considered structure reconfigured its shape in nearly 7 seconds, and the starting configuration was recovered upon removing the solar stimulus. The dynamic temperature profile caused by irradiation further elucidated the photothermal-hygroscopic actuation strategy introduced in the present demonstrator.

Overall, and commensurate with the present developmental stage, the reported demonstrators support the potential for effective implementation of the proposed photothermal-hygroscopic actuation strategy in a variety of applications involving soft material systems, and in particular soft actuators.

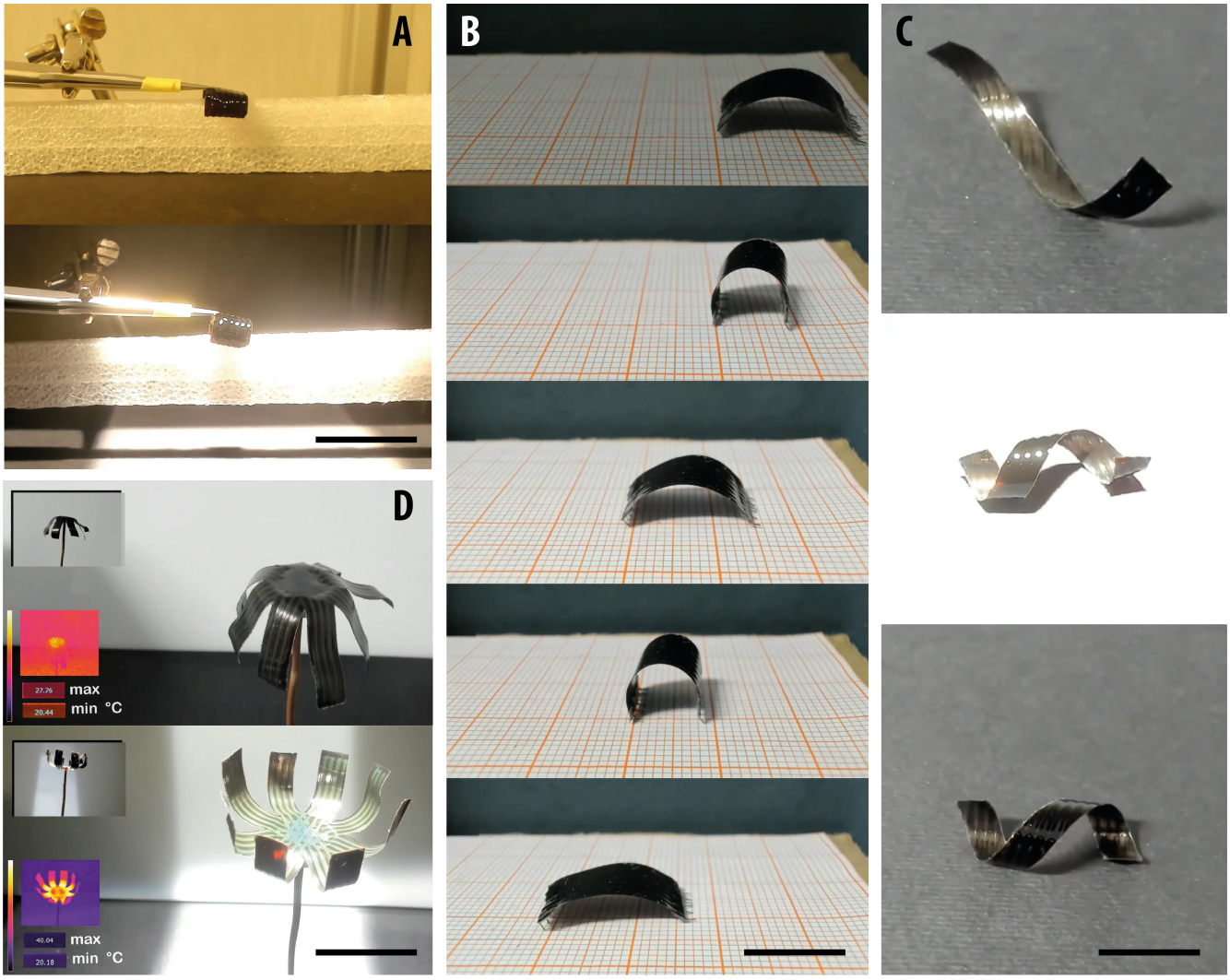

Figure 4.32: Photothermal actuator for soft robotics applications. A) Grasping test of a polystyrene sample (156 mg mass, 11-fold the actuator mass) with a BL/PPTL/HL rectangular actuator (2 x 1 cm). The test consists of: 1. Approaching; 2. Grasp activation under light exposure; 3. Sustained grasping; 4. Grasp deactivation; 5. Sample release. B) Crawling test of the rectangular BL/PPTL/HL actuator (2 × 1 cm) under subsequent light exposure. Scalebar is 2 cm. C) Rolling test of the rectangular actuator (0.5 × 4.5 cm) with CMC tracks printed with an angle of 20° with respect to the longitudinal axis, under dark(1)/light exposure(2)/dark(3) cycles. Scalebar is 1 cm. D) Artificial light-responsive actuator structure devised for uniaxial programmed motion based on the BL/PPTL/HL in lateral and tilted view exposed to a dark(1)/light exposure(2)/dark(3) cycle. Scalebar is 1 cm. Thermocamera image during the exposure of the actuator structure devised for uniaxial programmed motion under sunlight. All the experiments are performed under a simulated sunlight power density of 1 Sun.

4.4 Bioinspired Biodegradable Soft bending actuator

The combined effects of thermo-sensitive and photothermal materials pre-sent novel actuation strategies for wireless application and the use of sustainable energy sources, such as the sunlight. To understand the operating features of multifunctional materials, bioinspired multi-layer actuators represent a simple solution as a testing platform. Moreover, growing interest in green chemistry drives researchers in finding sustainable and innovative solutions. Inspired by the material composition of natural hygroscopic actuators (i.e. pinecones, Geraniaceae seeds, wheat), we defined lignin an outstanding candidate for the fabrication of photothermal actuators, as it is one of the most abundant materials and has a photothermal conversion efficiency of about 20% [72].

Here, we report the fabrication of a bilayer photothermal and biodegradable bending actuator, based on thermal expansion of polycaprolactone-lignin blend (PPL), 3D printed on cellulose acetate substrate. When the actuator is irradiated with 300 mW/cm^2 of simulated solar irradiance, it shows a change in curvature of 25.34%, with a bending moment of 80.2 μN·m and with a characteristic actuation time of 30s. Moreover, the photothermal blend shows a conversion efficiency of 13.5%.

Due to the photothermal and biodegradability properties, the actuator could be used as a battery-free tool for different tasks, in a scenario where no contamination of the environment is required.

4.4.1 Materials and Methods

Materials and chemicals: PCL (Number average molar mass 80 kg/mol) was purchased from ThermoFisher Scientific (Massachusetts, USA). Alkaline lignin was purchased from Tokyo Chemical Industry (Japan). Pluronic F127 and acetic acid (CH3COOH, 99.8%) were purchased from Merck Millipore (Massachusetts, USA). CA 25μm thick film was purchased from Goodfellow GmbH (Germany).

Preparation of PPL blend: The PPL blend was prepared using solvent casting method, mixing 6.5g of PCL, 0.5g of Pluronic F127, 0.5g or 2g of alkaline lignin (7% w/w and 17% w/w with respect the total weight of the blend) with 10 ml of acetic acid. The solution was continuously stirred at 200rpm with a temperature of T=80°C for 48h. Next, the solvent was removed via evaporation, keeping the temperature constant at T = 150°C for 60 minutes. **4D printing of the bending actuator**: We extruded the solid and homogeneous blend with FDM printer (3DBioplotter, EnvisionTEC) using the following printing conditions: nozzle internal diameter 0.3mm, temperature 150°C, needle offset 0.24mm, pressure 6 bar, speed 22 mm/s, pre-flow 0.05s, post-flow -0.05s. Hence, we fabricated the actuator depositing aligned fibers of PPL with distance between strands 1.5mm on a CA film. Finally, the CA-PPL sheet is cut using CO2 laser cutter (Beamo, FLUX) with relative power 20 (defined by Beam Studio GUI) and cutting speed 8 mm/s.

Plasma activation: To promote adhesion between the two polymers, we activated the CA surface using air plasma (Tergeo, Pie Scientific). The plasma time was set to 60s, power setpoint to 75W, gas setpoint 30 sccm (cm3/min) and base vacuum to 0.50 mbar.

Photothermal characterization: FDM printed PPL samples (1cm × 1cm × 300µm) were irradiated under solar spectrum SciSun 300 Sun Simulator (Sci-encetech, Canada) at different powers (100-300 mW/cm^2). Samples were sus-pended in air using Teflon tweezers to avoid any thermal diffusion in the sample holder. Power densities of the simulated sunlight were verified using an RS PRO solar energy meter (RS, UK). The variation of temperature due to photothermal effect was carried out with an IR thermal camera (A700, FLIR Systems, USA). The experiments were performed in ambient air (T=25 °C, 30% RH).

Curvature evaluation: The actuator was exposed to 300 mW/cm^2 of simulated solar irradiance (SciSun 300 Sun Simulator Sciencetech, Canada), while simultaneously video recording the variation of radius (Logitech Brio Stream, Logitech). To ensure complete thermalstability, the samples were exposed for 5 minutes. To evaluate the variation of curvature, all the video-data are post-processed using ImageJ software. The experiments were performed in ambient air (T=25 °C, 30% RH measured using RS PRO RS-325A Digital Hygrometer). The evaluation of curvature variation due to hygroscopic effect was performed in climatic test chamber (CTC256, Memmert GmbH), fixing the temperature T=30°C and chang-ing RH from 30% to 90%.

Static Moment test: For the moment evaluation, force is measured with 10g sen-sitive load cell (Futek LSB200, USA), calibrated using samples with a weight force equal to 0.59 mN. Solar irradiance was selected using the Sun Simulator SciSun 300 (Sciencetech, Canada). The measurement consists in putting in contact with a suspended load cell the CA-PPL bilayer sample (1cm × 2 cm,width and length, respectively) and subsequently the actuator is irradiated cyclically (period 15 mins with 50% duty cycle) from 0 to 300 mW/cm2. The experiments were performed in ambient air (T=25 °C, 30% RH measured using RS PRO RS-325A Digital Hygrometer. According to the experimental setup, the moment was evaluated assuming that M = 1/2 F·L.

Photography: Photographs were taken using a digital camera (D7100, Nikon, Japan).

Data analysis: The normality of data distribution was tested with the Shapiro–Wilk test; normally-distributed data were analyzed with ANOVA followed by LSD post hoc with Bonferroni correction and expressed as average ± standard error. Non-normally distributed data were analyzed with the Kruskal–Wallis test followed by pairwise Wilcox post hoc test with Holm correction and expressed as median ± 95% confidence interval. Each experiment has been performed in trip-licate (n = 3), if not differently indicated. The data were analyzed and plotted in Origin (Version 2019b, 32bit).

4.4.2 Evaluation of the Photothermal Conversion Efficiency of PPL blend

We first verified the photothermal properties of PPL blend, comparing the photo-thermal conversion efficiency of two different samples dispersing in the PCL polymer matrix respectively 7% and 17% w/w of alkaline lignin.

We tested the robustness of the effect changing irradiance with 12.5 minutes illumination cycle with 50% of duty cycle. Figure 4.33A shows an increase of temperature due to photothermal effect, when the specimens were subjected to 100 mW/cm of simulated solar irradiance. Figure 4.33A shows that PCL did not present any photothermal properties, while PPL samples with 7% and 17%

w/w of lignin reach in both cases a temperature peak of T_M = 42.5±0.7 °C in τ = 87.6±2.5 s. Since the samples with different amount of lignin did not show a statistically significant variation (paired t-test $p^* > 0.05$), we selected the PPL solution with lower dispersion grade, because an increase of lignin dispersant in PCL polymeric matrix will make the blend more brittle and it will reduce the processability and the printability [73].

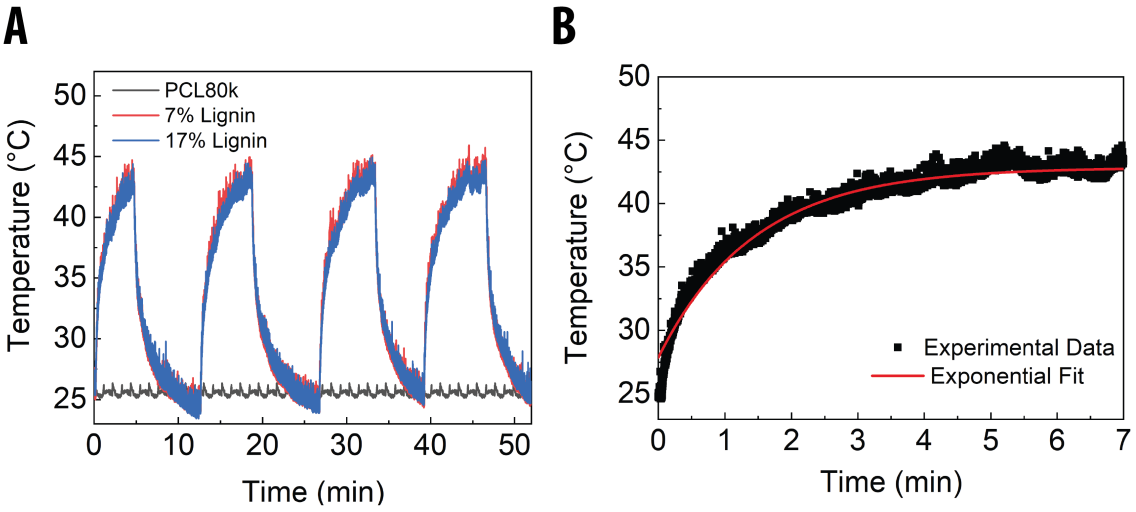

Figure 4.33: Photothermal properties of PPL blend at different concentrations of lignin. A) Time behavior of photothermal effect (12.5 minutes illumination cycle with 50% of duty cycle) under 100 mW/cm^2 of simulated solar irradiance input. B) Exponential fit of the tempera-ture variation (R^2 = 0.98) used for the evaluation of the photothermal conversion efficiency in 7% w/w lignin sample

Consider the thermal kinetic of a solid body that exchanges heat with the environmental air in natural convection regime, it was possible to evaluate the photothermal conversion efficiency (η) [39] from the exponential fit of the temperature dynamics (Figure 4.33)B. To evaluate η, we assumed that the impinging light is completely absorbed by the PPL (α = + inf) and we consider in first approximation that the density and the specific heat capacity are mainly governed by PCL properties (ρ = 1120 kg m^{-3}, c_p = 2.2 J g^{-1} K^{-1} [74]). Hence, knowing that the sample thickness is h = 0.30±0.01 mm, T, T_0= 25 °C, ΔT = 17.5 °C, τ = 87.6 s, the experimental PCE is equal to η = 13.5%.

4.4.3 Fabrication of the photothermal actuator

We proceed with the manufacturing of the bending actuator, FDM printing on a plasma activated cellulose acetate substrate the PPL blend (Figure 4.34A). When the actuator is irradiated, the photothermal element will determine a local increase of temperature in the actuator. Subsequently, the PPL layer will anisotropic expand along the printing direction since it is mainly composed by a high thermal expansion coefficient PCL polymer (16 × 10-5 $°C^{-1}$ [74]). When the sample is no longer irradiated, the reciprocal effect occurs on the PPL layer and the structure will recover its initial shape (Figure 4.34B).

Figure 4.34D shows images of FDM printed PPL sample with 7% alkaline lignin. Due to the complete homogenization of lignin in the acetic acid solution, no aggregation was visible in the PPL. We further verified the 3D printing capabilities of the photothermal blend printing a squared structure (1cm × 1cm × 3mm) with honeycomb features (hexagonal side 2.5mm). Printing planes shows perfect adhesion, highlighting the possibility to fabricate complex 3D structures with biodegradable properties and photothermal features. Figure

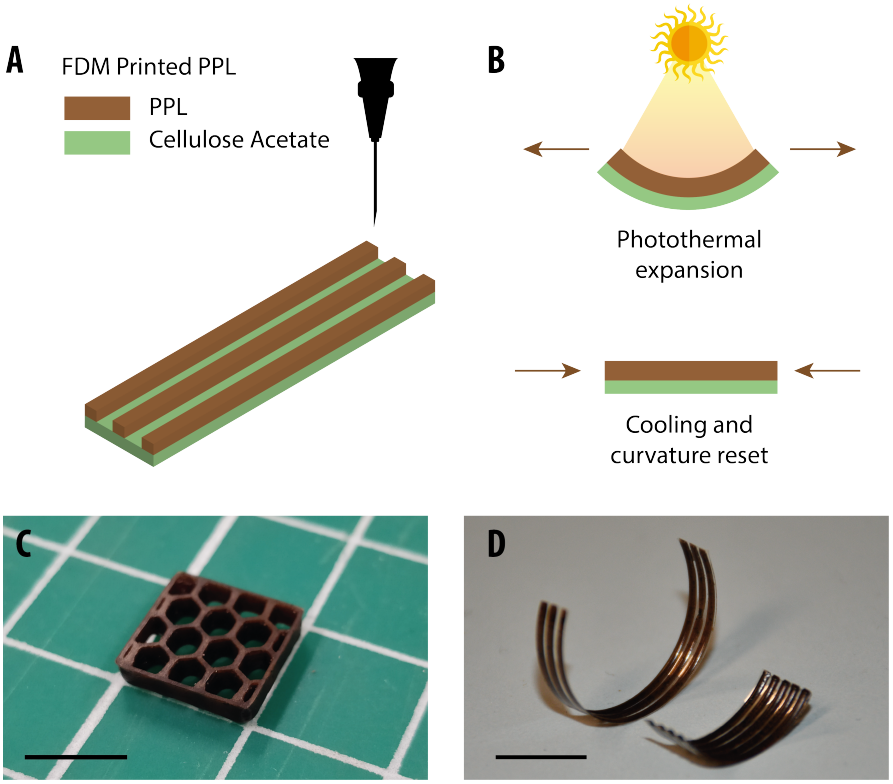

Figure 4.34: Sketch and working principle of the photothermal bending actuator. A) Representation of the fabrication process to realize the PPL-CA actuator. In particular, the PPL blend is ex-truded on a CA substrate with aligned tracks. B) Working principle of the actuator during solar illumination. When the sample is irradiated, there will be an increase of temperature in the whole actuator. Then, the PPL region will anisotropic expand due to the thermal expan-sion properties of PCL. C) Working principle of the actuator without illumination. Due to the decrease of temperature, the PPL layer shows anisotropic contraction, recovering its initial curvature. D) 3D printed honeycomb sample. Scalebar is 1 cm. E) Two different samples of soft actuators. Scalebar is 2 cm.

4.34E shows two different samples of bending soft actuators fabricated via FDM printing, where the PPL fiber-like structures present a trapezoidal shape, with a maximum thickness of $h_F = 0.37 \pm 0.07$ mm and a minimum distance between strands of $d_F = 1.2 \pm 0.2$mm.

4.4.4 Kinematics and static of the photothermal actuator

We investigate the effective bending deformation of the structure due to photothermal expansion of the PPL. In Figure 4.35 is reported the curvature of the actuator exposed to 300 mW/cm^2 of simulated solar irradiance. The initial curvature in the idle condition was equal to $\kappa_0 = 83.3 \pm 2.3$ m^{-1} (Figure 4.35A). After the illumination, the actuator reaches the thermal equilibrium in 30 ±2.5 s with a curvature $\kappa_1 = 59.0 \pm 3.4$ m^{-1} (Figure 4.35B). Coming back to the idle state, the curvature reaches the initial value $\kappa_2 = 83.3 \pm 1.6$ m^{-1} in 30.0±2.5 s (tested on n = 5 different samples). Therefore, the actuator shows a reversible bending behavior mediated by the photothermal effect, showing 25.34% in change of curvature.

Considering that cellulose acetate is a hygroscopic material [75], we verified the effective hygroscopic behavior of the actuator measuring the variation of curvature when it is subjected to variation of relative humidity from 30% to 90%. The actuator showed 1% of curvature variation, value that is one order of magnitude lower with respect to the curvature variation induced by the photothermal effect. Hence, we have observed that, in a first approximation, the actuator is predominantly powered by the thermal expansion mechanism.

To understand the effective performance of CA-PPL, we performed the static evaluation of the beam moment. Figure 4.36 shows the time behavior of the bending moment when the actuator is subjected to 300 mW/cm^2. The moment

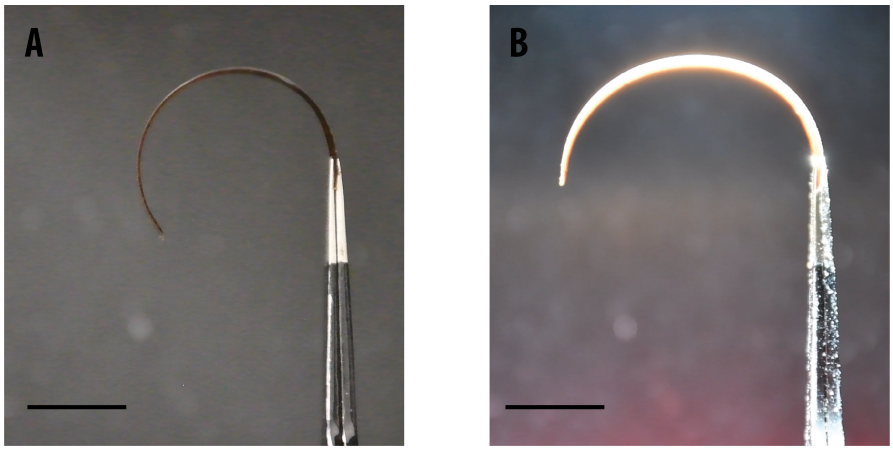

Figure 4.35: Kinematics of photothermal actuator. A) The actuator in its resting position. The initial curvature is related to residual stressed due to fabrication process. Scalebar is 1cm. B) The actuator subjected to 300 mW/cm^2 of simulated solar irradiance. Scalebar is 1cm.

reaches a peak of M = 80.2±5.3 μN·m (tested on 5 different trials). As in the curvature case, the moment reaches its saturation value in 30.0 ± 2.5s. However, the main limitation of the system is evident after 5 cycles of 1 min illumination under an external load (constrained reaction of the load cell), since the PPL layer starts to redistribute the internal stress through a deformation of the entire body, due to the low melting point of the PCL component (T_M=60°C) in the PPL blend.

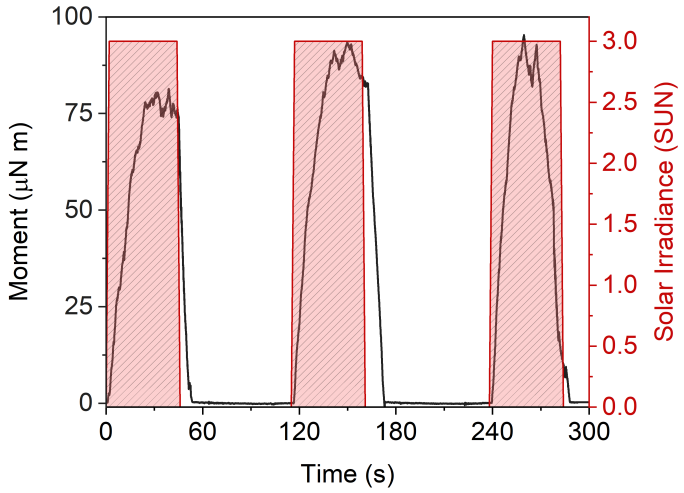

Figure 4.36: Moment of the photothermal actuator as function of time exposed to 300 mW/cm^2 of simulated solar irradiance.

Conclusion and Future perspectives

5

This thesis has successfully addressed the need for a comprehensive framework for the design and fabrication of seed-inspired soft robots, with a focus on hygroscopic and thermal embodied energy, using environmental friendly materials. The bioinspired characterization protocol developed herein serves as a critical tool for extrapolating design rules from biological systems to guide the creation of efficient and adaptable soft robots. This research is an integral part of the European Project I-Seed https://cordis.europa.eu/project/id/101017940, which lays the foundation for the the use of biological inspiration to introduce concepts for new technologies, and an environmentally benign approach for their design and effective application in sustainable enviromental monitoring.

At first, we investigated the principles behind the hygroscopic movement of Erodium and Pelargonium seeds. From the internal tissue organization, we were able to understand the deformation of seed's awn, as superposition of bending and torsion. Considering the key features extrapolated from the seed investigation, we present a suitable model to predict and design the behaviour of helical cylindrical hygroscopic actuator, structured as bilayer. The model combine laminate composite plates and spring theory to predict with statistical significance the dyanmic performances, described as extensional force and torque.

Considering the additive manufacturing technique, the integration of Fused Deposition Modeling and electrospinning has demonstrated its efficacy in achieving complex geometries and material properties necessary for reaching adaptability, functionality and fast prototyping. This unique features permitted to fabricate a seed-like soft robot with superior performances, able to explore autonomously a sample soil. We also demonstrated that the same device can be successfully used as visual humidity sensor. Furthermore, we propose a technique to realize photothermal and hygroscopic actuators, which can be also used as surface functionalization of soft materials. Thanks to Direct Ink Writing technique, we were able to fast prototyping complex patterns of actuation, with isotropic and anisotropic features. Finally, we propose also a biodegradable solution for photothermal actuation, working with thermal expansion of polymers.

The commitment to sustainability through the adoption of low exergy systems, leveraging environmental sources of embodied energy (relative humidity, temperature and solar irradiance), exemplifies a conscientious approach to engineering that aligns with the pressing global imperative for eco-conscious technologies.

The identified future perspectives hold substantial promise for advancing the field of soft robotics. The exploration of energy density enhancement through the synergistic interaction of thermal expansion and hygroscopic contraction presents an exciting avenue for further research. Moreover, the pursuit of completely biodegradable soft robots aligns with the imperative to minimize environmental impact and reduce waste in engineering practices.

The proposed study of multi-layer actuators using Finite Element Modeling, considering various environmental stimuli as sources of actuation, represents a

advanced approach to achieving robust adaptability in soft robots. The integration of additive and subtractive manufacturing techniques for the realization of origami/kirigami structures offers potential breakthroughs in achieving intricate and customizable soft robot morphologies.

Furthermore, the robot should be used as autonomous platform for environmental monitoring, embedding contaminant sensor inside the bulk materials, which changes their physical parameters according to a specific amount of contaminant. The sensing mechanism should involve a photoluminescent transduction, where the contaminant interact with a fluorescent biodegradable dye that will change its optical features according to the standard of reference (intensity, wavelength, phase, polarization). The fluorescence should be induced remotely by an UAV loaded with f-Lidar and the local re-emission is interpreted by IR or Vis camera. Finally, all the information collected are pre-processed on board and then they are sent to control unit for real time evaluation of contaminant distribution, both with high spatial and temporal resolution. Such green soft robots, endowed with sensing abilities, are envisioned as simple and low-cost tools to be used for collecting environmental data in-situ via remote sensing, across large remote areas where no monitoring data are available, and for extending current environmental sensor frameworks and data analysis systems.

There are a set of advantages in doing environmental monitoring using this paradigms. On the one hand, the seed-like robot represents an integrated version of sampling and sensing, without needing a human operator in the dissemination process (sowing and harvesting) or a further data elaboration in ex-situ laboratory. Then, drilling and dispersion mechanisms should not require any external energy supply, since the movement exploit environmental sources such as wind and temperature/humidity variation. Next, remote sensing mechanism and biodegradability (destructive sample) will make measurement disposable, accessible also in harsh regions, affordable and reliable. Finally, considering the dispersion mechanism, the sensing network will allow to obtain high spatial and temporal resolution. On the other hand, the system presents some challenges. First of all, the accuracy and the relative quality control must require an in-depth analysis, comparing the results with reference one obtained with standard technologies. This implies that the overall cost associated to the topsoil and air evaluation will increase to obtain a solid statistical basis for the next monitoring. Furthermore, we have to consider the sensitivity of the system through the transduction chain mechanisms: the contaminant will chemically bond to the fluorescent dye, that will change its optical fluorescence properties and next the light emission will be evaluated with an array of cameras at different wavelengths (from visible to IR) with a minimum pixel detection.

Moreover, the robot should be used as self-dispersal tool for top-soil monitoring, as well as reforestation tool and, combining together all the previous features, a an innovative phytoremediation tool, with release on command if a certain alert threshold is exceeded. In addition, should be interesting to further extend the visual sensor behaviour, measuring temperature, irradiance, and humidity. This platform represents a significant advancement in the development of intelligent and self-sustained soft robotic systems for environmental monitoring.

Moving forward, there are several compelling avenues for future research. Exploring the chemistry of materials to enhance diffusivity, mechanical stability, and relative hygroscopic expansion stands as a critical area of study. Understanding the chemical properties that govern these characteristics will undoubtedly lead to the development of materials with enhanced performance,

unlocking new possibilities for soft robot design and functionality. For instance, the definition a biodegradable on-demand class of materials and mechanical structures could be fundamental for the development of autonomous soft robots which will operate in sensitive ecosystems.

In addition, delving deeper into structural mechanics prototyping beyond the multi-layer approach holds great potential. This entails investigating novel structural configurations and materials that can further optimize the performance of soft robots. By pushing the boundaries of structural design, we can achieve even greater levels of adaptability and efficiency in soft robotic systems.

Moreover, it is imperative to emphasize the interdisciplinary nature of this research endeavor. Collaborations with experts in fields such as materials science, chemistry, mechanical engineering, and environmental science will be instrumental in advancing the frontiers of soft robotics and sustainability. This interdisciplinary approach will foster the exchange of knowledge and expertise, leading to innovative solutions that transcend the boundaries of individual disciplines.

In conclusion, the findings presented in this thesis lay a strong foundation for future research endeavors in the domain of soft robotics and sustainable engineering. The combination of innovative design methodologies, advanced manufacturing techniques, and a steadfast commitment to environmental stewardship positions this work at the forefront of cutting-edge research in the field. The proposed future perspectives offer a roadmap for further exploration and expansion, with the potential to revolutionize the way we conceive and implement soft robotic systems in the context of a sustainable future.

Bibliography

Here are the references in citation order.

[1] Jizhong Zhou, Shijun Ma, and George W. Hinman. 'Ecological exergy analysis: a new method for ecological energetics research'. In: *Ecological Modelling* 84.1 (1996), pp. 291–303. DOI: https://doi.org/10.1016/0304-3800(94)00135-9 (cited on page 1).

[2] Rachael Beddoe et al. 'Overcoming systemic roadblocks to sustainability: The evolutionary redesign of worldviews, institutions, and technologies'. In: *Proceedings of the National Academy of Sciences* 106.8 (2009), pp. 2483–2489. DOI: 10.1073/pnas.0812570106 (cited on page 2).

[3] D. Griggs, M. Stafford-Smith, and O. et al. Gaffney. 'Sustainable development goals for people and planet'. In: *Nature* 495.8 (2013), pp. 305–307. DOI: 10.1038/495305a (cited on pages 3, 4).

[4] W. Adams. 'The future of sustainability : re-thinking environment and development in the twenty-first century'. In: *nternational Union for Conservation of Nature* (2006) (cited on page 4).

[5] L. Magee, A. Scerri, and P. James. 'Measuring Social Sustainability: A Community-Centred Approach'. In: *Applied Research Quality Life* 7 (2012), pp. 239–261. DOI: 10.1007/s11482-012-9166-x (cited on page 4).

[6] Sustainable Development Goals : 'https://www.undp.org/sustainable-development-goals'. In: () (cited on page 4).

[7] S.S. Sethi et al. 'Biodegradable sensors are ready to transform autonomous ecological monitoring.' In: *Nat. Ecol. Evol.* 6 (2022), pp. 1245–1247. DOI: https://doi.org/10.1038/s41559-022-01824-w (cited on page 5).

[8] Fabian Wiesemüller et al. 'Self-Sensing Cellulose Structures With Design-Controlled Stiffness'. In: *IEEE Robotics and Automation Letters* 6.2 (2021), pp. 4017–4024. DOI: 10.1109/LRA.2021.3067243 (cited on page 5).

[9] Florian Hartmann, Melanie Baumgartner, and Martin Kaltenbrunner. 'Becoming Sustainable, The New Frontier in Soft Robotics'. In: *Advanced Materials* 33.19 (2021), p. 2004413. DOI: https://doi.org/10.1002/adma.202004413 (cited on page 5).

[10] C.A. Aubin et al. 'Towards enduring autonomous robots via embodied energy'. In: *Nature* 602 (2022), pp. 393–402. DOI: 10.1038/s41586-021-04138-2 (cited on page 6).

[11] Barbara Mazzolai and Cecilia Laschi. 'A vision for future bioinspired and biohybrid robots'. In: *Science Robotics* 5.38 (2020), eaba6893. DOI: 10.1126/scirobotics.aba6893 (cited on page 6).

[12] H F Howe and J Smallwood. 'Ecology of Seed Dispersal'. In: *Annual Review of Ecology and Systematics* 13.1 (1982), pp. 201–228. DOI: 10.1146/annurev.es.13.110182.001221 (cited on page 6).

[13] P. Fratzl and F. Barth. 'Biomaterial systems for mechanosensing and actuation'. In: *Nature* 462 (2009), pp. 442–448. DOI: 10.1038/nature08603 (cited on page 7).

[14] Yael Abraham and Rivka Elbaum. 'Hygroscopic movements in Geraniaceae: the structural variations that are responsible for coiling or bending'. In: *New Phytologist* 199.2 (2013), pp. 584–594. DOI: https://doi.org/10.1111/nph.12254 (cited on pages 7, 17, 18, 21, 43).

[15] Rivka Elbaum et al. 'The Role of Wheat Awns in the Seed Dispersal Unit'. In: *Science* 316.5826 (2007), pp. 884–886. DOI: 10.1126/science.1140097 (cited on pages 7, 20, 21).

[16] Dennis Evangelista, Scott Hotton, and Jacques Dumais. 'The mechanics of explosive dispersal and self-burial in the seeds of the filaree, Erodium cicutarium (Geraniaceae)'. In: *Journal of Experimental Biology* 214.4 (2013), pp. 521–529. DOI: 10.1242/jeb.050567 (cited on pages 7, 17–19, 21).

[17] Lining Yao and Hiroshi Ishii. 'Hygromorphic living materials for shape changing'. In: *Robotic Systems and Autonomous Platforms*. Ed. by Shawn M. Walsh and Michael S. Strano. Woodhead Publishing in Materials. Woodhead Publishing, 2019, pp. 41–57. DOI: https://doi.org/10.1016/B978-0-08-102260-3.00003-2 (cited on pages 7, 10).

[18] Carmen J. Eger et al. 'The Structural and Mechanical Basis for Passive-Hydraulic Pine Cone Actuation'. In: *Advanced Science* 9.20 (2022), p. 2200458. DOI: https://doi.org/10.1002/advs.202200458 (cited on page 7).

[19] C. Dawson, J. Vincent, and AM Rocca. 'How pine cones open'. In: *Nature* 390 (1997), p. 668. DOI: 10.1038/37745 (cited on pages 8, 21, 42).

[20] Graham Edgar and W. O. Swan. 'The factors dermining the hygroscopic properties of soluble substanceS'. In: *Journal of the American Chemical Society* 44.3 (1922), pp. 570–577. DOI: 10.1021/ja01424a014 (cited on page 8).

[21] K. Boki and S. Ohno. 'Equilibrium Isotherm Equations to Represent Moisture Sorption on Starch'. In: *Journal of Food Science* 56.4 (1991), pp. 1106–1107. DOI: https://doi.org/10.1111/j.1365-2621.1991.tb14654.x (cited on page 8).

[22] Simon L. Clegg et al. 'Modelling the hygroscopic growth factors of aerosol material containing a large water-soluble organic fraction, collected at the Storm Peak Laboratory'. In: *Atmospheric Environment* 214 (2019), p. 116760. DOI: https://doi.org/10.1016/j.atmosenv.2019.05.068 (cited on page 9).

[23] Fangfang Deng et al. 'Hygroscopic Porous Polymer for Sorption-Based Atmospheric Water Harvesting'. In: *Advanced Science* 9.33 (2022), p. 2204724. DOI: https://doi.org/10.1002/advs.202204724 (cited on page 9).

[24] Ugur Ulusoy. 'A Review of Particle Shape Effects on Material Properties for Various Engineering Applications: From Macro to Nanoscale'. In: *Minerals* 13.1 (2023). DOI: 10.3390/min13010091 (cited on page 9).

[25] Margarethe Hauck et al. 'Overcoming Water Diffusion Limitations in Hydrogels via Microtubular Graphene Networks for Soft Actuators'. In: *Advanced Materials* 35.41 (2023), p. 2302816. DOI: https://doi.org/10.1002/adma.202302816 (cited on page 9).

[26] Ingo Burgert and Peter Fratzl. 'Actuation systems in plants as prototypes for bioinspired devices'. In: *Philosophical Transactions of the Royal Society A: Mathematical, Physical and Engineering Sciences* 367.1893 (2009), pp. 1541–1557. DOI: 10.1098/rsta.2009.0003 (cited on page 9).

[27] Jan M. Skotheim and L. Mahadevan. 'Physical Limits and Design Principles for Plant and Fungal Movements'. In: *Science* 308.5726 (2005), pp. 1308–1310. DOI: 10.1126/science.1107976 (cited on page 9).

[28] Silvia Taccola et al. 'Toward a New Generation of Electrically Controllable Hygromorphic Soft Actuators'. In: *Advanced Materials* 27.10 (2015), pp. 1668–1675. DOI: https://doi.org/10.1002/adma.201404772 (cited on pages 10–13, 39, 42, 66).

[29] Beomjune Shin et al. 'Hygrobot: A self-locomotive ratcheted actuator powered by environmental humidity'. In: *Science Robotics* 3.14 (2018), eaar2629. DOI: 10.1126/scirobotics.aar2629 (cited on pages 10–13, 18, 32, 39, 43).

[30] Dario Lunni et al. 'Plant-Inspired Soft Bistable Structures Based on Hygroscopic Electrospun Nanofibers'. In: *Advanced Materials Interfaces* 7.4 (2020). DOI: https://doi.org/10.1002/admi.201901310 (cited on pages 11, 12, 39, 45, 55, 66).

[31] Keumbee Kim et al. '4D Printing of Hygroscopic Liquid Crystal Elastomer Actuators'. In: *Small* 17.23 (2021), p. 2100910. DOI: https://doi.org/10.1002/smll.202100910 (cited on pages 11–13).

[32] Pingan Zhu et al. 'Bioinspired Soft Microactuators'. In: *Advanced Materials* 33.21 (2021), p. 2008558. DOI: https://doi.org/10.1002/adma.202008558 (cited on pages 11, 12).

[33] F. Zhang et al. 'Unperceivable motion mimicking hygroscopic geometric reshaping of pine cones.' In: *Nature Materials* 21 (2022), pp. 1357–1365. DOI: 10.1038/s41563-022-01391-2 (cited on pages 11–13).

[34] Jie Cao et al. 'Ultrarobust Ti3C2Tx MXene-Based Soft Actuators via Bamboo-Inspired Mesoscale Assembly of Hybrid Nanostructures'. In: *ACS Nano* 14.6 (2020), pp. 7055–7065. DOI: 10.1021/acsnano.0c01779 (cited on pages 11, 12, 14).

[35] Yinan Li et al. 'High-Sensitivity Multiresponses Cellulose-Based Actuators with Configurable Amplitude'. In: *ACS Sustainable Chemistry & Engineering* 10.19 (2022), pp. 6414–6425. DOI: 10.1021/acssuschemeng.2c01152 (cited on pages 11, 12, 14).

[36] Tingting Zhao et al. 'A Multi-Responsive MXene-Based Actuator with Integrated Sensing Function'. In: *Advanced Materials Interfaces* 9.10 (2022), p. 2101948. DOI: https://doi.org/10.1002/admi.202101948 (cited on pages 11, 12, 14).

[37] Wendong Liu et al. 'Enable Multi-Stimuli-Responsive Biomimetic Actuation with Asymmetric Design of Graphene-Conjugated Conductive Polymer Gradient Film'. In: *ACS Nano* 17.16 (2023), pp. 16123–16134. DOI: 10.1021/acsnano.3c05078 (cited on pages 11, 12, 14).

[38] Luca Cecchini et al. '4D Printing of Humidity-Driven Seed Inspired Soft Robots'. In: *Advanced Science* 10.9 (2023). DOI: https://doi.org/10.1002/advs.202205146 (cited on pages 11, 12, 18–20, 52, 54, 55, 57).

[39] Stefano Mariani et al. 'A Bioinspired Plasmonic Nanocomposite Actuator Sunlight-Driven by a Photothermal-Hygroscopic Effect for Sustainable Soft Robotics'. In: *Advanced Materials Technologies* 8.14 (2023) (cited on pages 11, 12, 72).

[40] Jonghyun Ha et al. 'Hygroresponsive coiling of seed awns and soft actuators'. In: *Extreme Mechanics Letters* 38 (2020), p. 100746. DOI: https://doi.org/10.1016/j.eml.2020.100746 (cited on pages 15, 20, 21, 28, 32, 43, 45, 47).

[41] Shahaf Armon et al. 'Geometry and Mechanics in the Opening of Chiral Seed Pods'. In: *Science* 333.6050 (2011), pp. 1726–1730. DOI: 10.1126/science.1203874 (cited on pages 15, 28, 29).

[42] Omar Fiz et al. 'Phylogenetic Relationships and Evolution in Erodium (Geraniaceae) Based on trnL-trnF Sequences'. In: *Systematic Botany* 31.4 (2006), pp. 739–763 (cited on page 17).

[43] P.F. Yeo. 'Fruit-discharge-type in Geranium (Geraniaceae): its use in classification and its evolutionary implications'. In: *Botanical Journal of the Linnean Society* 89.1 (1984), pp. 1–36. DOI: https://doi.org/10.1111/j.1095-8339.1984.tb00998.x (cited on page 17).

[44] T. Marcussen and AS. Meseguer. 'Species-level phylogeny, fruit evolution and diversification history of Geranium (Geraniaceae)'. In: *Molecular Phylogenetics and Evolution* 110 (2017), pp. 134–149. DOI: 10.1016/j.ympev.2017.03.012 (cited on page 17).

[45] Wonjong Jung, Wonjung Kim, and Ho-Young Kim. 'Self-burial Mechanics of Hygroscopically Responsive Awns'. In: *Integrative and Comparative Biology* 54.6 (2014), pp. 1034–1042. DOI: 10.1093/icb/icu026 (cited on pages 17, 18, 21, 43).

[46] Y. Abraham et al. 'Mapping of Cell wall Aromatic Moieties and Their Effect on Hygroscopic Movement in the Awns of Stork's Bill'. In: *Cellulose* 25.7 (2018), pp. 3827–3841. DOI: 10.1007/s10570-018-1852-x (cited on page 18).

[47] Nancy E. Stamp. 'Self-Burial Behaviour of Erodium Cicutarium Seeds'. In: *Journal of Ecology* 72.2 (1984), pp. 611–620. (Visited on 08/25/2023) (cited on pages 19–21).

[48] Benjamin Shapiro and Elisabeth Smela. 'Bending Actuators with Maximum Curvature and Force and Zero Interfacial Stress'. In: *Journal of Intelligent Material Systems and Structures* 18.2 (2007), pp. 181–186. DOI: 10.1177/1045389X06063801 (cited on pages 20, 65, 66).

[49] Yael Abraham et al. 'Tilted cellulose arrangement as a novel mechanism for hygroscopic coiling in the stork's bill awn'. In: *Journal of The Royal Society Interface* 9.69 (2012), pp. 640–647. DOI: 10.1098/rsif.2011.0395 (cited on pages 20, 21).

[50] Carmela de Marco, Salvador Pané, and Bradley J. Nelson. '4D printing and robotics'. In: *Science Robotics* 3.18 (2018). DOI: 10.1126/scirobotics.aau0449 (cited on pages 39, 44).

[51] Xiao Kuang et al. 'Advances in 4D Printing: Materials and Applications'. In: *Advanced Functional Materials* 29.2 (2019). DOI: https://doi.org/10.1002/adfm.201805290 (cited on pages 39, 44).

[52] Al Hosni AS, Pittman JK, and Robson GD. 'Microbial degradation of four biodegradable polymers in soil and compost demonstrating polycaprolactone as an ideal compostable plastic.' In: *Waste Management* 97 (2019), pp. 105–114. DOI: 10.1016/j.wasman.2019.07.042 (cited on pages 39, 44, 45).

[53] Dan Kai, Sing Shy Liow, and Xian Jun Loh. 'Biodegradable polymers for electrospinning: Towards biomedical applications'. In: *Materials Science and Engineering: C* 45 (2014), pp. 659–670. DOI: https://doi.org/10.1016/j.msec.2014.04.051 (cited on pages 39, 44).

[54] F.V. Ferreira et al. 'How do cellulose nanocrystals affect the overall properties of biodegradable polymer nanocomposites: A comprehensive review'. In: *European Polymer Journal* 108 (2018), pp. 274–285. DOI: https://doi.org/10.1016/j.eurpolymj.2018.08.045 (cited on page 39).

[55] T. Hamann, E. Smets, and F. Lens. 'A comparison of paraffin and resin-based techniques used in bark anatomy'. In: *Taxon* 60 (2011), pp. 841–851. DOI: 10.1002/tax.603016 (cited on page 40).

[56] E.E. Morrill et al. 'A validated software application to measure fiber organization in soft tissue.' In: *Biomech Model Mechanobiol* 15 (2016), pp. 1467–1478. DOI: 10.1007/s10237-016-0776-3 (cited on page 41).

[57] W.C. Oliver and G.M. Pharr. 'Measurement of hardness and elastic modulus by instrumented indentation: Advances in understanding and refinements to methodology'. In: *Journal of Materials Research* 19.1 (2004), pp. 3–20. DOI: 10.1557/jmr.2004.19.1.3 (cited on page 41).

[58] E.G. Herbert, W.C. W C Oliver, and G.M. G M Pharr. 'Nanoindentation and the dynamic characterization of viscoelastic solids'. In: *Journal of Physics D: Applied Physics* 41.1 (2008). DOI: 10.1088/0022-3727/41/7/074021 (cited on page 41).

[59] F.V. Ferreira et al. 'Functionalized cellulose nanocrystals as reinforcement in biodegradable polymer nanocomposites'. In: *Polymer Composites* 39.S1 (2018), E9–E29. DOI: https://doi.org/10.1002/pc.24583 (cited on page 44).

[60] M Momtaz and J. Chen. 'High-Performance Colorimetric Humidity Sensors Based on Konjac Glucomannan.' In: *ACS Appl Mater Interfaces.* (2020). DOI: 10.1021/acsami.0c16495 (cited on page 56).

[61] Xing Rao et al. 'Review of Optical Humidity Sensors'. In: *Sensors* 21.23 (2021). DOI: 10.3390/s21238049 (cited on page 56).

[62] D. Kou et al. 'High-Performance and Multifunctional Colorimetric Humidity Sensors Based on Mesoporous Photonic Crystals and Nanogels.' In: *ACS Appl Mater Interfaces.* (2018). DOI: 10.1021/acsami.8b14223 (cited on page 56).

[63] Stefano Mariani et al. 'Maskless Preparation of Spatially-Resolved Plasmonic Nanoparticles on Polydimethylsiloxane via In Situ Fluoride-Assisted Synthesis'. In: *Advanced Functional Materials* 31.26 (2021). DOI: 10.1002/adfm.202100774 (cited on pages 57, 61, 62).

[64] Stefano Mariani et al. '4D Printing of Plasmon-Encoded Tunable Polydimethylsiloxane Lenses for On-Field Microscopy of Microbes'. In: *Advanced Optical Materials* 10.3 (2022). DOI: 10.1002/adom.202101610 (cited on page 57).

[65] Ying Hu et al. 'Self-Locomotive Soft Actuator Based on Asymmetric Microstructural Ti3C2Tx MXene Film Driven by Natural Sunlight Fluctuation'. In: *ACS Nano* 15.3 (2021). DOI: 10.1021/acsnano.0c10797 (cited on page 58).

[66] Yinan Li et al. 'High-Sensitivity Multiresponses Cellulose-Based Actuators with Configurable Amplitude'. In: *ACS Sustainable Chemistry & Engineering* 10.19 (2022). DOI: 10.1021/acssuschemeng.2c01152 (cited on page 60).

[67] Padryk Merkl et al. 'Plasmonic Coupling in Silver Nanoparticle Aggregates and Their Polymer Composite Films for Near-Infrared Photothermal Biofilm Eradication'. In: *ACS Applied Nano Materials* 4.5 (2021), pp. 5330–5339. DOI: 10.1021/acsanm.1c00668 (cited on page 61).

[68] Qing Zhang et al. 'In-situ synthesis of poly(dimethylsiloxane)–gold nanoparticles composite films and its application in microfluidic systems'. In: *Lab Chip* 8 (2 2008), pp. 352–357. DOI: 10.1039/B716295M (cited on page 61).

[69] Victor T. Noronha et al. 'Silver nanoparticles in dentistry'. In: *Dental Materials* 33.10 (2017), pp. 1110–1126. DOI: https://doi.org/10.1016/j.dental.2017.07.002 (cited on page 61).

[70] J. Kim et al. 'Simple and cost-effective method of highly conductive and elastic carbon nanotube/polydimethylsiloxane composite for wearable electronics.' In: *Sci Rep* 8.1375 (2018). DOI: 10.1038/s41598-017-18209-w (cited on page 62).

[71] Y. Trantidou T.and Elani, E. Parsons, and et al. 'Hydrophilic surface modification of PDMS for droplet microfluidics using a simple, quick, and robust method via PVA deposition.' In: *Microsyst Nanoeng* 3.16091 (2017). DOI: 10.1038/micronano.2016.91 (cited on page 65).

[72] Jinxing Li et al. 'Lignin: a sustainable photothermal block for smart elastomers'. In: *Green Chem.* 24 (2 2022), pp. 823–836. DOI: 10.1039/D1GC03571A (cited on page 70).

[73] Jing Tian, Yiqin Yang, and Junlong Song. 'Grafting polycaprolactone onto alkaline lignin for improved compatibility and processability'. In: *International Journal of Biological Macromolecules* 141 (2019), pp. 919–926. DOI: https://doi.org/10.1016/j.ijbiomac.2019.09.055 (cited on page 72).

[74] A. Wurm, M. Merzlyakov, and C. Schick. 'Reversible Melting During Crystallization of Polymers Studied by Temperature Modulated Techniques (TMDSC, TMDMA).' In: *Journal of Thermal Analysis and Calorimetry* 60 (2000), pp. 807–820. DOI: 10.1023/A:1010195321797 (cited on page 72).

[75] S. Khoshtinat, V. Carvelli, and C. Marano. 'Characterization and modeling the hygroscopic behavior of cellulose acetate membranes.' In: *Cellulose* 29 (2022), pp. 2175–2186. DOI: 10.1007/s10570-022-04450-8 (cited on page 73).

Acknowledgement

I would like to express my deepest gratitude to my supervisors, Prof. Nicola M. Pugno and Dr. Barbara Mazzolai, for their unwavering support, for allowing me to work in a well-funded research environment, in direct contact with international excellence.

I would like to acknowledge the financial support provided by European Union Horizon 2020 research and innovation programme under grant agreement N'o. 101017940 (I-Seed) that made this research possible. This support has been crucial in facilitating the necessary resources and opportunities for the successful completion of this thesis.

A special mention goes to Dr. Stefano Mariani, whose dedication and collaborative spirit have significantly contributed to the success of this thesis. Dr. Mariani's expertise, passion and tireless efforts in science have left an indelible mark on the project, and I am truly thankful for the collaborative environment he fostered. We faced many personal and professional challenges, coming out richer and richer by backing each other up.

I extend my appreciation to the entire Bioinspired Soft Robotics group. The intellectual fellowship and shared passion for discovery have created a stimulating and supportive research environment, where the bioinspiration key has necessarily drawn the attention of many professionals from different fields of research, making the laboratory a delightful springboard for better understanding nature. For me, it's critical for any scientist to understand that one's educational background lays a solid foundation for embarking on a path of research, but it's curiosity and passion that moves the spirit. This is only possible by renewing the passion by continuously comparing and cooperating without constraints with professionals with heterogeneous knowledge.

My sincere thanks also go to my family for their unwavering encouragement and understanding during the highs and lows of this academic journey. Their belief in me has been a constant source of motivation. Moreover, I would like to acknowledge my friend Daniele Silvestri from ISIA Roma Design for his curiosity, knowledge sharing and his support in producing and publishing visual artworks.

I express all gratitude to all those musicians who accompany me and continue to accompany me in life.

In addition, heartfelt gratitude is extended to those individuals who, in the future, find inspiration within the pages of this thesis, kindling an unequivocal passion and interest in the realms of science and phenomenology. May this work serve as a beacon, never dampening the flame of their inner curiosity. I hope it sparks a journey to unravel the intricate simplicity inherent in nature. A special acknowledgment is reserved for the global community of ecologists. May this thesis contribute to the fortification of sustainable principles through ecological concepts, fostering a resilient and harmonious coexistence between humanity and our precious spaceship, the planet Earth.